

**A Search for the Rare Decay  $K^+ \rightarrow \pi^+ \nu \bar{\nu}$**

DANIEL S. AKERIB

A dissertation  
presented to the Faculty  
of Princeton University  
in candidacy for the degree of  
Doctor of Philosophy

Recommended for acceptance  
by the Department of Physics

January 1991

## Abstract

This thesis describes an experimental search for the weak decay  $K^+ \rightarrow \pi^+ \nu \bar{\nu}$  performed at Brookhaven National Laboratory during the Winter of 1989 using the E787 Spectrometer designed expressly for this purpose.

The first-order contribution to this decay cancels exactly via the Glashow-Iliopoulos-Maiani (G.I.M.) Mechanism. However, the second-order process is expected to give a branching ratio between  $.6 \rightarrow 6 \times 10^{-10}$  in the Standard Model. The predicted rate for this process is theoretically well determined; the uncertainty is due to the experimental input parameters of the Model.

We find no candidate events in a sample of  $1.12 \times 10^{11}$  kaon decays and we set an upper limit on the branching ratio of  $4.4 \times 10^{-9}$  at the 90% confidence level. Using the same data we also set an upper limit on the process  $K^+ \rightarrow \pi^+ f$  of  $9.3 \times 10^{-10}$  at the 90% confidence level, where  $f$  is any neutral massless weakly-interacting particle.

## Acknowledgements

This thesis would not have been possible without the efforts of a great many people, whom I would like to thank:

My adviser, Stew Smith, has given me a tremendous of encouragement and guidance over the last six years; he even stood by me after I beat his BNL-Princeton driving-time record of an hour and fifty-one minutes. A great advantage of being a student on a high-energy physics experiment is that there are plenty of guys around to show you what's what; most of what I learned I picked up by working alongside Professors Bill Louis, Dan Marlow, Pete Meyers and Frank Shoemaker. This list would not be complete without Mats Selen, my fellow student and good friend, who led the way and shared his fruit pies and night shifts with me. Many thanks also to the guys at the EP Lab for teaching me some of the nuts and bolts of this operation and for all the fun we had installing detectors and eating in diners; to the teams from Brookhaven and TRIUMF for their commitment to the experiment; and to the staff of the Physics Department for making this a fun place to work. And thanks to Professor Fitch for taking the time to read through all this.

I would like to thank my friends in Princeton for all the good times—Steve Hagen, Hien Nguyen, Mary Brunkow, Steve Vandermark, Denis Keane, Dimitri Kusnezov, Lorraine Nelson, Laurel Lerner, and Vadim Polyakov; and also my friends Noah Kaplan, Adam Grimshaw, and Marianne Engelman. Finally, let me say that this would all have been pretty unlikely without the love and support of my family, especially my parents Richard and Yolanda, and my sister Andrea.

## Contents

Abstract .....	ii
Acknowledgements .....	iii
Table of Contents .....	iv
Chapter 1: Introduction .....	1
1.1 Overview .....	1
1.2 Theoretical Considerations .....	3
1.2.1 The Weak Interaction .....	3
1.2.2 On the Calculation of the Branching Ratio for $K^+ \rightarrow \pi^+ \nu \bar{\nu}$ .....	6
1.2.3 Beyond the Standard Model .....	10
Chapter 2: The Detector .....	12
2.1 Introduction .....	12
2.2 The Sub-systems .....	19
2.2.1 The Beam Line .....	19
2.2.2 The Beam Counters .....	20
2.2.3 The Target .....	23
2.2.4 The Drift Chamber .....	26
2.2.5 The Range Stack .....	27
2.2.6 The Photon Vetoes .....	29
Chapter 3: The Online Event Selection .....	34
3.1 Introduction .....	34
3.2 General Aspects of the Trigger .....	34

---

3.3 The Level 0 Trigger .....	37
3.3.1 Stopped Kaons .....	38
3.3.2 Kinematics: Fiducial Volume and Stopping Layer .....	39
3.3.3 The Barrel and Endcap Photon Vetoes .....	41
3.4 The Level 1 Trigger .....	41
3.4.1 The Hextant Photon Veto .....	41
3.4.2 The Refined Range Trigger .....	42
3.5 The Data Acquisition System .....	43
3.6 The Level 1.5 Energy Trigger .....	45
3.7 The Level 2 $\pi \rightarrow \mu$ Tagger .....	46
Chapter 4: The Offline Analysis .....	48
4.1 Introduction .....	48
4.2 The Analysis Passes .....	49
4.3 Description of the Cuts .....	52
4.3.1 Track Reconstruction .....	55
4.3.1.1 The Target Segment .....	55
4.3.1.2 The Drift Chamber Segment .....	57
4.3.1.3 The Range Stack Segment .....	57
4.3.1.4 Reconstruction Cuts .....	59
4.3.2 Fiducial Volume Cuts .....	60
4.3.3 The Delayed Coincidence Cut .....	61
4.3.4 The Transient Digitizer Cuts .....	61
4.3.4.1 The $\pi^+ \rightarrow \mu^+$ Tagging .....	62
4.3.4.2 The $\mu^+ \rightarrow e^+$ Tagger .....	68
4.3.5 Photon Veto Cuts .....	72
4.3.6 Kinematics .....	75
4.3.6.1 Range-Momentum .....	77
4.3.6.2 Energy, Momentum, Range and the "Box" Cut .....	79
4.3.7 Beam Cuts .....	82
4.4 Summary of the Cuts .....	84
Chapter 5: The Sensitivity .....	87

---

5.1 Introduction .....	87
5.2 The Factors .....	91
5.3 $K_{\mu 2}$ Measurements .....	94
5.3.1 Offline Reconstruction .....	94
5.3.2 Accidentals, Beam Cuts and Timing .....	96
5.4 $\pi$ -scat Measurements .....	98
5.4.1 Kinematic Cuts .....	99
5.4.2 Transient Digitizer (TD) Cuts .....	100
5.4.2.1 The Area Method .....	100
5.4.2.2 TD Cuts: the Counting Method .....	104
5.5 $K_{\pi 2}$ Measurements .....	105
5.5.1 The Level 1.5 Energy Trigger .....	106
5.5.2 The Hardware Stopping Counter .....	109
5.6 Monte Carlo Measurements .....	110
5.6.1 The Workings of UMC .....	111
5.6.2 UMC Acceptance Factors .....	113
5.7 Normalization .....	115
5.7.1 The Flux .....	115
5.7.2 The $K_{\mu 2}$ Branching Ratio .....	116
5.7.3 The $K_{\pi 2}$ Branching Ratio .....	118
Chapter 6: Conclusion .....	122
6.1 Limits on $K^+ \rightarrow \pi^+ \nu \bar{\nu}$ and $K^+ \rightarrow \pi^+ f$ .....	122
6.2 Future Prospects .....	124
References .....	126

## 1. Introduction

### 1.1 OVERVIEW

The Standard Model of strong and electroweak interactions is an extremely successful description of the physics of elementary particles. Since its crystallization some two decades ago, experimental physicists have been hard pressed to produce any evidence that runs contrary to it, much less to suggest a specific direction to guide the many speculations that go beyond it. The high energy physics community as a whole seeks yet a more fundamental theory because for all of its elegance and predictive power, the Standard Model still has a degree of arbitrariness. Left unanswered are questions about the number of generations (to wit, why there is more than one!), the origin of CP violation, and the mass spectrum and “mixing” of the numerous particles otherwise described so well.

The two main roads available to the experimenter are to explore with greater precision Standard Model parameters in the hope of finding an inconsistency, and to search for new phenomena that are clearly distinct from Standard Model predictions. To these ends, Experiment 787 searches for the weak processes  $K^+ \rightarrow \pi^+ \nu \bar{\nu}$ , allowed by the Standard Model at *second* order, and  $K^+ \rightarrow \pi^+ f$ , a hypothetical decay where  $f$  is a neutral weakly-interacting massless particle.

The first process is forbidden to first-order because the so-called Glashow-Iliopoulos-Maiani (G.I.M.) Mechanism causes weak neutral currents that change quark flavor to cancel exactly [1]; however, we shall see that in second-order processes the cancellation is spoiled by mass differences in the internal quark lines. The branching ratio in the six-quark Standard Model was first calculated in detail by Inami and Lim [2]; they showed that the rate is dominated by a heavy *top* quark and the decay might thus be accessible to experimental measurement. The second process describes physics that goes beyond the predictions of the Standard Model;

possibilities for  $f$  are the “familon” hypothesized by Wilczek [3], or other massless Goldstone bosons that could explain unaccounted-for broken symmetries.

The Standard Model allows a very precise calculation for the branching fraction into the final state  $\pi^+\nu\bar{\nu}$ ; as we will discuss below, hadronic uncertainties are made to cancel and long-distance electromagnetic effects are negligible. Nevertheless, the actual prediction of  $.6-6\times 10^{-10}$  [4] is uncertain due to our lack of knowledge of the experimental input parameters; a measurement of the rate could thus help to constrain them.

Alternatively, a number of effects could alter the rate from the above prediction, indicating “new” physics. A fourth quark generation\* [5] or super-symmetric extensions of the Standard Model [6-8] could enhance the rate by adding more possibilities for the virtual particles in the loop diagrams (see Figure 1). Light neutral super-symmetric particles could also enhance the rate by adding more decay channels, as could Majorana (massive) neutrinos. The Majorana model would also change the momentum spectrum of the  $\pi^+$  from the Standard Model expectation [9], although an experiment sensitive enough to measure the kinematic line-shape is unlikely in the foreseeable future.

In all of this, we search for a signal of the form  $K^+ \rightarrow \pi^+ + \textit{nothing}$ , where *nothing* means that the particle or system of particles recoiling off of the  $\pi^+$  goes undetected. The signal is thus characterized by a single charged-pion and nothing else; the momentum spectrum distinguishes the two-body from the three-body final state. Chapters 2-5 contain a detailed description of the detector, event trigger, and subsequent data analysis; here we note more generally that although kaons have been studied for the last thirty years, it is only the latest generation of experiments that have acquired the requisite sensitivity to detect a signal. Advances in accelerator design have produced beams of ever increasing intensity and purity, while advances in electronics have led to fast intelligent triggers and high-speed data acquisition systems that can take advantage of the available kaons.

The ultimate goal of E787 at Brookhaven National Laboratory’s Alternating Gradient Synchrotron is to look for  $K^+ \rightarrow \pi^+\nu\bar{\nu}$  with sensitivity to a branching ratio of  $2 \times 10^{-10}$ . Data taken over a two week period at the end of an engineering run in 1988 yielded an upper limit of  $3.4 \times 10^{-8}$  [10], a factor of 4 improvement over the previous search [11]. The subject of this thesis is data taken during the Winter of 1989, which was the first full run of the experiment. Although these data did not yield any candidate events, they allow us to further extend the upper limit for  $K^+ \rightarrow \pi^+\nu\bar{\nu}$  to  $4.4 \times 10^{-9}$  or another factor of 8. The same data give an upper limit

---

\* Given recent LEP results this would presumably be accompanied by a lepton doublet having a massive neutrino.

for  $K^+ \rightarrow \pi^+ f$  of  $9.3 \times 10^{-10}$ , a factor of 41 over the previous search and a factor of 7 over our 1988 result (same references as before). With the current schedule, the design goal should be reached with data taken in 1992.

## 1.2 THEORETICAL CONSIDERATIONS

### 1.2.1 The Weak Interaction

We review here some of the historical development of weak interactions, concluding with the form of the charged and neutral currents that describe the interactions among and between the quarks and leptons. It is the nature of these currents that is of particular importance to the phenomenology of  $K^+ \rightarrow \pi^+ \nu \bar{\nu}$ . The first theory of the weak force was due to Fermi, who described  $\beta$ -decay as a four-point Lorentz-covariant vector interaction of two Dirac currents. These are weak decays that take place in nucleons via a charge-changing current-current interaction; in modern terms we understand them to be  $d \rightarrow u$  transitions among the nuclei's constituent quarks.

As the quark model was expanded to accommodate *strangeness*, particularly the weak decays of charged and neutral kaons, and muons were understood to decay weakly, a unified theory of weak interactions was sought to account for increasingly diverse phenomena whose common denominator was relatively long-lived states. A turning point was the so-called  $\tau$ - $\theta$  puzzle in which two presumably different particles had equal mass but *opposite parity*. The mystery was resolved when Lee and Yang, after a careful survey of weak interaction data, realized that parity conservation had never actually been demonstrated; they claimed that the  $\tau$  and the  $\theta$  were one and the same particle (the  $K^+$ ) and that weak interactions violated parity symmetry [12]. This made it clear that Fermi theory was incomplete. The violation of this symmetry was soon thereafter accommodated by the  $V - A$  theory of Feynman and Gell-Mann [13], again a Lorentz covariant theory of charged-current interactions but with the added property that states thus defined are not eigenstates of the parity operator. This is embodied by the Lagrangian

$$L_{V-A} = -\frac{G_F}{\sqrt{2}}(J^\mu J_\mu^\dagger + J^{\mu\dagger} J_\mu),$$

where  $J$  and  $J^\dagger$  describe *charge-raising* and *-lowering* currents for both quarks and

leptons. The currents contain terms like

$$\bar{\psi}\gamma^\mu(1 - \gamma^5)\psi,$$

where  $\psi$  and  $\bar{\psi}$  are particle and anti-particle Dirac spinors, and the  $V - A$  character of the theory comes from the difference of terms: the vector part  $\gamma^\mu$  is even under parity and the axial-vector part  $\gamma^\mu\gamma^5$  is odd, hence the difference is not a parity eigenstate. Since the  $V - A$  mixture projects only left-handed helicity states, this means that the charged-current interaction violates parity maximally.

In its original formulation the above theory tried to describe  $\beta$ -decay in nuclei ( $d \rightarrow u$  transitions), kaon decay ( $s \rightarrow u$ ), and muon decay ( $\mu \rightarrow e$ ), however, a problem arose in that different coupling constants were needed for each. Cabibbo noticed that a universal constant would accurately describe transition rates in all three classes if he treated the  $d$  quark as a "rotated" superposition of  $d$  and  $s$  [14]:

$$\begin{pmatrix} u \\ d \end{pmatrix} \rightarrow \begin{pmatrix} u \\ d_c \end{pmatrix} = \begin{pmatrix} u \\ d \cos \theta_c + s \sin \theta_c \end{pmatrix}.$$

It should be noted that this is a purely empirical construction; there exists no fundamental reason that weak-interaction eigenstates should behave in this way. Nonetheless, a value of approximately  $\theta_c = 13^\circ$  supplied the proper correction, one that allowed for a single universal weak coupling for charged-current interactions.

Given the presence of charged-current interactions, it was natural to expect neutral currents as well, yet none were observed. They were searched for in charged and neutral kaon decays, where the otherwise much more dominant electromagnetic and strong interactions were known to be absent. Processes like  $K_L \rightarrow \mu^+\mu^-$  and  $K^+ \rightarrow \pi^+\nu\bar{\nu}$  (involving  $s \rightarrow d$  transitions) appeared to be highly suppressed relative to their charged-current ( $s \rightarrow u$ ) counterparts even though a naive construction of the neutral current indicates a non-zero amplitude:

$$\begin{aligned} J_{\text{NC}} &= \bar{u}u + \bar{d}_c d_c \\ &= \bar{u}u + \bar{d}d \cos^2 \theta_c + \bar{s}s \sin^2 \theta_c + (\bar{d}s + \bar{s}d) \cos \theta_c \sin \theta_c. \end{aligned}$$

The absence of these processes were explained when Glashow, Iliopoulos and Maiani introduced the *charmed* quark and showed that although neutral currents might still exist, they could not lead to changes in quark flavor [1]. By extending the Cabibbo Model to four quarks arranged in two doublets

$$\begin{pmatrix} u \\ d_c \end{pmatrix} \begin{pmatrix} c \\ s_c \end{pmatrix},$$

where  $s_c = d \sin \theta_c - s \cos \theta_c$  consists of the  $d$ - $s$  combination orthogonal to  $d_c$ , the part of the neutral current responsible for flavor changes cancels completely. This

is most easily seen by writing the  $-1/3$ -charged quarks as a column vector to show the relationship between the *weak* and *mass* eigenstates:

$$\begin{pmatrix} d_c \\ s_c \end{pmatrix} = \begin{pmatrix} \cos \theta_c & \sin \theta_c \\ -\sin \theta_c & \cos \theta_c \end{pmatrix} \begin{pmatrix} d \\ s \end{pmatrix}.$$

Now we form the hadronic part of the neutral current:

$$\begin{aligned} J_{\text{NC}} &= (\bar{u} \quad \bar{c}) \begin{pmatrix} u \\ c \end{pmatrix} + (\bar{d}_c \quad \bar{s}_c) \begin{pmatrix} d_c \\ s_c \end{pmatrix} \\ &= \bar{u}u + \bar{c}c + (\bar{d} \quad \bar{s}) M_c^\dagger M_c \begin{pmatrix} d \\ s \end{pmatrix} \\ &= \bar{u}u + \bar{c}c + \bar{d}d + \bar{s}s \end{aligned}$$

where  $M_c$  is the above rotation matrix and we observe that owing to the unitarity of the matrix, off-diagonal elements like  $\bar{d}s$  cancel, leaving no amplitude for flavor changes in the neutral current. The cancellation is known as the G.I.M. Mechanism. (The  $\gamma$ -matrices are omitted for simplicity).

The expansion to an arbitrary number of generations does not disturb the cancellation since the mixing matrix is by definition unitary. To summarize, we write the hadronic charged and neutral currents for the present-day six-quark theory as:

$$J^\mu = (\bar{u} \quad \bar{c} \quad \bar{t}) \gamma^\mu (1 - \gamma^5) \begin{pmatrix} d_c \\ s_c \\ b_c \end{pmatrix}$$

and

$$J_{\text{NC}}^\mu = (\bar{u} \quad \bar{c} \quad \bar{t}) \gamma^\mu (c_A - c_V \gamma^5) \begin{pmatrix} u \\ c \\ t \end{pmatrix} + (\bar{d}_c \quad \bar{s}_c \quad \bar{b}_c) \gamma^\mu (c_A - c_V \gamma^5) \begin{pmatrix} d_c \\ s_c \\ b_c \end{pmatrix}$$

where the factors  $c_A$  and  $c_V$  come from the full unified electroweak theory [15] and indicate that the neutral current (unlike the charged) is not generally pure  $V - A$ . The currents each correspond to the emission of the massive vector bosons,  $W^\pm$  in the case of  $J^\mu$  and  $Z^0$  in the case of  $J_{\text{NC}}^\mu$ . The quark rotation in the six-quark model is due to Kobayashi and Maskawa who expanded the Cabibbo Model as follows [16]:

$$\begin{pmatrix} d_c \\ s_c \\ b_c \end{pmatrix} = \begin{pmatrix} V_{ud} & V_{us} & V_{ub} \\ V_{cd} & V_{cs} & V_{cb} \\ V_{td} & V_{ts} & V_{tb} \end{pmatrix} \begin{pmatrix} d \\ s \\ b \end{pmatrix},$$

where the  $3 \times 3$  (CKM) matrix is unitary and complex, and has non-zero off-diagonal

elements which mix the quark states. Their motivation was a model for CP violation but they operated under the constraint that the G.I.M. Mechanism should still work.

### 1.2.2 On the Calculation of the Branching Ratio for $K^+ \rightarrow \pi^+ \nu \bar{\nu}$

Now that we have the expressions for the weak currents we can draw the Feynman graphs for semi-leptonic  $K^+$  decays. For sake of comparison we include the related charged-current semi-leptonic mode along with first- and second-order diagrams for  $K^+ \rightarrow \pi^+ \nu \bar{\nu}$ . As alluded to earlier, the first-order process for  $K^+ \rightarrow \pi^+ \nu \bar{\nu}$  cancels exactly; however, we shall see that interference among the second-order terms spoils the cancellation to give a non-zero rate. The calculation of the branching ratio is discussed following a survey of the diagrams.

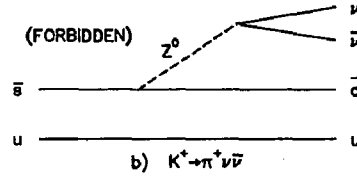
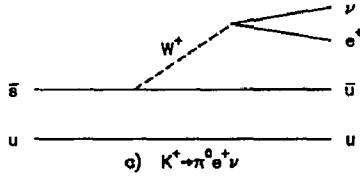
The first-order diagrams (Figure 1a-b) show, at right, the allowed decay  $K^+ \rightarrow \pi^0 e^+ \nu$ , which proceeds via a charged  $W^+$  current and has a branching ratio of 5%, and at left, what  $K^+ \rightarrow \pi^+ \nu \bar{\nu}$  would look like at first order if it could proceed via  $Z^0$  emission; of course as we saw above, the strangeness-changing amplitude for the neutral current is zero. Indeed, the relative rates of charged and neutral decays nearly signalled an early death for any theory based on neutral currents; for example, early limits showed [17]:

$$\frac{K^+ \rightarrow \pi^+ \nu \bar{\nu}}{K^+ \rightarrow \pi^0 \mu^+ \nu} < 10^{-5}.$$

In Figure 1c-d we see explicitly the importance of the  $K^+ \rightarrow \pi^+ \nu \bar{\nu}$  process to the study of weak interactions: observation of the decay would serve as the first direct test for a *purely weak* second-order process in a perturbative theory. Although  $K_L \rightarrow \mu^+ \mu^-$  has been observed, its interpretation as a purely weak second-order process is complicated by interference with electromagnetic effects. Like  $K^+ \rightarrow \pi^+ \nu \bar{\nu}$  it is based on an  $s \rightarrow d$  transition, but the induced  $Z^0$  vertex can also be replaced by a virtual photon since the final state leptons are charged.

Notice the internal quark line in the loop diagrams. The amplitude associated with each diagram depends on the quark mass through the propagator term as  $m_q^2/M^2$ , where  $M$  is the mass of the exchange particle. In calculating the transition rate, the mass differences among the quarks turn out to be crucial in getting a non-zero branching ratio, even at second order. If we assume for a moment that the quark masses are equal then the propagator for each amplitude is identical and can be factored out. Hence, the current for say the ‘‘W-box’’ diagram (Figure 1c)

FIRST ORDER:



SECOND ORDER:

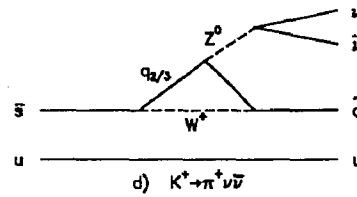
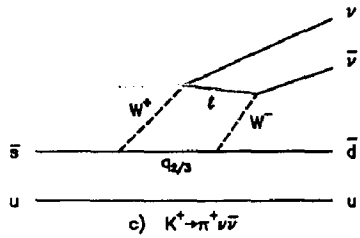


Figure 1. The (a) allowed and (b) forbidden first-order semi-leptonic  $K^+$  decays are shown at top. Below them are related second-order "loop" diagrams for  $K^+ \rightarrow \pi^+ \nu \bar{\nu}$ ; (c) can be thought of as adding a  $W$ /lepton coupling to (a), while (d) is a so-called *induced  $Z$  vertex*. Notice that both (c) and (d) include an internal  $u$ ,  $c$  or  $t$  quark labeled  $q_{2/3}$ ;  $l$  stands for any charged lepton and tags the flavor of the neutrinos as well.

has the following dependence on the CKM couplings:

$$J^\dagger J \sim V_{ud}^* V_{us} + V_{cd}^* V_{cs} + V_{td}^* V_{ts} \equiv 0,$$

and we see that the current vanishes identically. (The identity exploits the property of unitary matrices that the inner product of two column vectors is zero.) In other words, for equal quark masses the G.I.M. Mechanism is complete to all orders, hence the statement that unequal quark masses "spoil" the cancellation at second order.

The dependence on quark mass is particularly interesting at this juncture in history because the *top* quark has not yet been discovered.\* As noted earlier, Inami and Lim [2] calculated that the branching ratio depends heavily on the *top* quark term and increases with the *top* mass  $m_t$ ; in fact, the *charm* contribution to the rate only amounts to about 10% of the total. Thus, a measurement of this relatively

\* At the time of this writing the CDF Collaboration reports a lower bound on the *top* quark mass of  $m_t \geq 89.0 \text{ GeV}/c^2$  at the 95% confidence level.

low-energy process can probe physics at a higher mass scale not yet accessible at present accelerator energies. This is made more explicit by a precise calculation of the branching ratio which yields per neutrino generation [2,18,4]:

$$\frac{BR(K^+ \rightarrow \pi^+ \nu_i \bar{\nu}_i)}{BR(K^+ \rightarrow \pi^0 e^+ \nu)} = 2 \cdot \left( \frac{\alpha}{4\pi \sin^2 \theta_W} \right)^2 \cdot \frac{|\bar{D}_i|^2}{|V_{us}|^2},$$

where

$$\bar{D}_i = \sum_{j=c,t} V_{js}^* V_{jd} \bar{D}_j ((m_{qj}/m_W)^2; (m_{li}/m_W)^2)$$

is largely dominated by the *top* quark term for  $m_t \sim m_W$ . In this mass range,  $\bar{D}_i$  increases roughly linearly with  $m_t$ .

By calculating the rate relative to the measured and related process  $K^+ \rightarrow \pi^0 e^+ \nu$ , one avoids uncertainties in the hadronic wavefunctions. This is important because often long-distance effects such as these make the interpretation of weak reactions imprecise; an example is trying to use  $K^0 - \bar{K}^0$  mixing to test second-order effects. The calculation of  $K^+ \rightarrow \pi^+ \nu \bar{\nu}$  can be made in terms of  $K^+ \rightarrow \pi^0 e^+ \nu$  because of the similarities of the processes: both have a kaon in the initial state and a pion and two light leptons in the final state. The hadronic parts of the wavefunctions are related by a (strong) isospin rotation and are roughly unaffected by the short-range perturbation of the short-range weak vertex; whether the weak vertex is a single  $W$  emission or two  $W$ 's in a "box," the interaction essentially takes place at a point compared to the scale of the hadrons. A second effect that allows for a precise calculation was alluded to above in our mention of  $K_L \rightarrow \mu^+ \mu^-$ . In  $K^+ \rightarrow \pi^+ \nu \bar{\nu}$  long-distance electromagnetic terms are absent because the final state leptons are neutral, *i.e.*, neutrinos only interact weakly [19]. In other words, photons cannot contribute to the process directly, as they do in  $K_L \rightarrow \mu^+ \mu^-$ .

The most recent reference [4] includes the latest values for the CKM couplings and QCD corrections based on a *top* quark mass  $m_t$  comparable to the  $W$  mass. They find:

$$BR(K^+ \rightarrow \pi^+ \nu \bar{\nu}) = .6 \rightarrow 6 \times 10^{-10}$$

for three generations. The span is due to the freedom of the experimental input parameters, notably the CKM couplings in the third generation and  $m_t$ ; allowed branching ratio values are shown as a function of  $m_t$  in Figure 2 (also from [4]).

For a known *top* quark mass the largest uncertainty in the predicted branching ratio comes from our lack of knowledge of the CKM coupling  $V_{td}$ . The 1988 *Particle Data Group* reports a value in the range .001 to .023, which is largely determined by

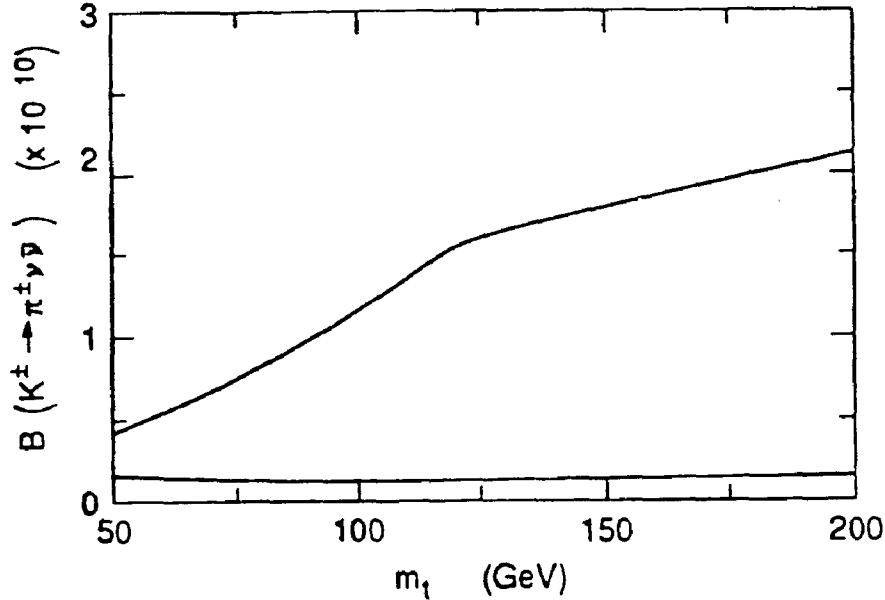


Figure 2. Maximum and minimum allowed branching ratio per neutrino flavor for  $K^+ \rightarrow \pi^+ \nu \bar{\nu}$ .

unitarity bounds on the full matrix; a direct measurement would require a sample of *top* quark decays. Therefore, a measurement of the  $K^+ \rightarrow \pi^+ \nu \bar{\nu}$  branching ratio would likely be in a position to set further bounds on  $V_{td}$ . Solving for  $V_{td}$  in the above equation in terms of the branching ratio and the other CKM couplings and taking  $m_t = 200 \text{ GeV}/c^2$  gives [20]:

$$|V_{td}|^2 = \left(1.30^{+0.47}_{-0.32}\right) \left[ \frac{BR(K^+ \rightarrow \pi^+ \nu \bar{\nu})}{2 \times 10^{-6}} - (2.41 \pm 0.74) \times 10^{-5} \right].$$

Now for example if  $BR(K^+ \rightarrow \pi^+ \nu \bar{\nu}) = 2.4 \times 10^{-10}$  then  $|V_{td}| = .0112$ . An experimental measurement uncertainty of 20% in the branching ratio translates into a 13% uncertainty in  $V_{td}$ ; however, this would be somewhat overshadowed by QCD-based theoretical uncertainties of about 20% [20]. Therefore, in the Standard Model scenario there is little reason to measure the branching ratio for  $K^+ \rightarrow \pi^+ \nu \bar{\nu}$  with an uncertainty of less than about 30%; this defines a goal for E787, which could be realized by the mid 1990's.

## 1.2.3 Beyond the Standard Model

Many model builders have speculated as to what might lie beyond the Standard Model. A number of their predictions could couple to flavor-changing neutral currents (FCNC's) and thus exhibit themselves in decays of the form  $K^+ \rightarrow \pi^+ f$ , where  $f$  is a neutral weakly-interacting massless (or nearly massless)\* particle, or  $K^+ \rightarrow X^0 X^0$ , where the  $X^0$ 's represent a pair of such particles. The possibilities breakdown into the three categories below:

- **Familons.** In an attempt to understand the structure of the quark-lepton generations, or "families," as some low-energy limit of a more fundamental symmetry, Wilczek [3] has proposed a so-called continuous flavor symmetry. The structure of the families we observe is due to the breaking of this symmetry. The theory is such that potentials in the Lagrangian which govern the symmetry lead to the presence of new massless colorless flavorless particles which he calls "familons." Since these particles are neutral and do not respect "flavor symmetry," it is natural to look for them in processes that take place via FCNC's.
- **Super-symmetry.** Although no physical evidence exists for super-symmetric extensions of the Standard Model, it appears to be quite popular among theoreticians. A number of authors [6-8] have discussed the possibility of additions to the Standard Model contribution for  $K^+ \rightarrow X^0 X^0$ , where  $X^0$  might be the usual neutrino or some other particle. Super-symmetric particles could contribute both to the internal loops in the Feynman diagrams and to the additional channels of unobserved particles in the final state. Certain channels could modify the shape of the  $\pi^+$  momentum spectrum [8].
- **Majorana neutrinos.** Bertolini and Santamaria [9] have investigated the possibility of Majorana neutrinos affecting the rate for  $K^+ \rightarrow X^0 X^0$ , should they exist. They find that the branching ratio could be enhanced by as much as the equivalent of effectively 1/2 a Standard Model lepton generation. They also show that the  $\pi^+$  spectrum could be significantly modified; we note however that from the experimentalists viewpoint the resolving of such subtleties is certainly a long way off.

It should be noted that no evidence for the last two items appeared at the recent first-round results from LEP experiments. Nonetheless, the possibility of

---

\* For  $m_f \leq 80 \text{ MeV}/c^2$  our acceptance is fairly uniform; however, for heavier particles the recoiling  $\pi^+$  cannot be clearly discerned from that of  $K_{\pi 2}$  decays, causing our acceptance to fall off sharply. (This is inherent in the experimental strategy and is discussed in Section 2.1.)

---

finding them in the distinct laboratory of the kaon is sufficiently motivated. Before turning to the actual experimental search, we note that a signal from this experiment alone would probably not distinguish among the variety of interpretations discussed herein but would certainly point the way to future investigations.

## 2. The Detector

### 2.1 INTRODUCTION

The E787 detector is uniquely designed to detect the rare decay mode  $K^+ \rightarrow \pi^+ \nu \bar{\nu}$  while offering a high degree of background suppression to the many standard first order decays. The strength of the detector lies in complete spatial and temporal event reconstruction, good online rejection, the ability to acquire data at high rates, good angular acceptance, and the near absence of dead material in the fiducial region. In this chapter I will motivate the detector's design criteria and describe its capabilities. In subsequent chapters I will explain how the information from the detector is exploited in the trigger and offline event selection.

Although I generally refer only to the decay mode  $K^+ \rightarrow \pi^+ \nu \bar{\nu}$ , the search for  $K^+ \rightarrow \pi^+ f$ , where  $f$  is any massless weakly-interacting neutral particle, proceeds in exact parallel since the signal for the latter would appear as a special case of the former, *i.e.*, decay pions collecting at the endpoint of the three-body spectrum. Analyses for the two modes diverge only in the measurement of the acceptance; unless stated otherwise,  $K^+ \rightarrow \pi^+ \nu \bar{\nu}$  is used generically to refer to both.

The essential criteria used to search for rare events are as follows:

- The incident beam particle is positively identified as a  $K^+$  that comes to rest before decaying.
- The subsequent decay products consist of a single charged track positively identified as a  $\pi^+$ . (Weakly-interacting neutral particles go undetected.)
- The  $\pi^+$  lies in the kinematic region  $213 < P_\pi < 237$  MeV/c.
- There are no photons in the event.

The selection criteria and the design of the detector itself are motivated to reject background, in particular, the  $K_{\mu 2}$  ( $K^+ \rightarrow \mu^+ \nu$ ) and  $K_{\pi 2}$  ( $K^+ \rightarrow \pi^+ \pi^0$ )

decay modes. With branching ratios of .63 and .21, respectively, they are the most frequent final states and by concentrating on them we suppress virtually all other kaon decay backgrounds.

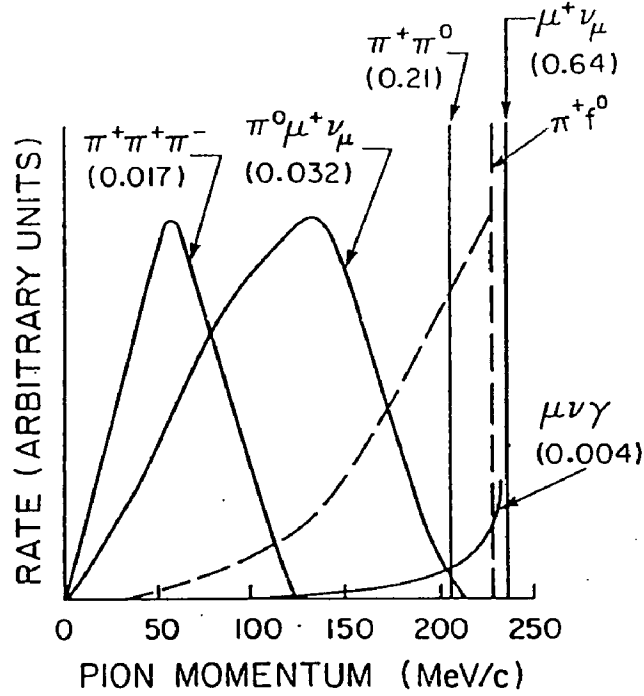


Figure 3. Momentum distributions of charged particles for background and rare processes calculated in the kaon rest frame. Numbers in parentheses indicate branching ratios for background modes. In the decay  $K^+ \rightarrow \pi^+ f$ ,  $f$  refers to any massless weakly-interacting neutral particle.

The stopped kaon requirement, which puts our kinematic measurements in the kaon rest frame, is vital because it preserves the monochromatic nature of the charged track from two-body decays. Figure 3 shows the momentum distribution of the charged particle for the rare modes and the primary backgrounds. By restricting our search to events with charged tracks lying between the  $K_{\pi 2}$  and  $K_{\mu 2}$  momentum peaks, we achieve a high degree of background rejection while still accepting about

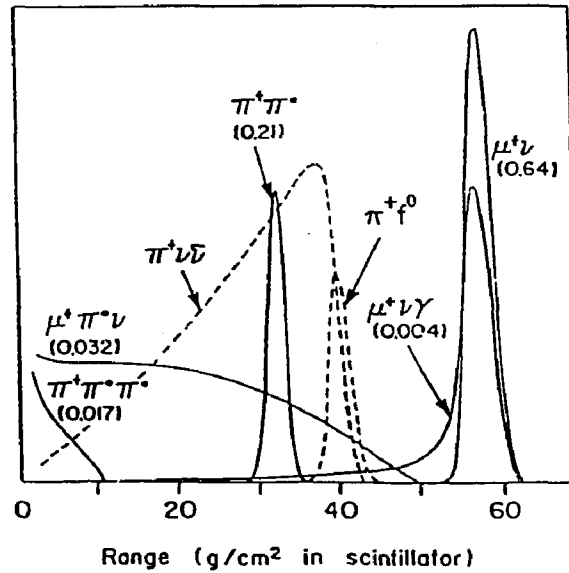


Figure 4. Range distributions of charged particles for background and rare processes, in the kaon rest frame.

20% of the  $K^+ \rightarrow \pi^+\nu\bar{\nu}$  phase space.\* Similar limits are placed on energy and range, where the kinematic separation between the peaks is even greater than for momentum. Figure 4 shows the range spectra for charged particles.

Of course, with finite separation between the  $\pi$  and  $\mu$  peaks and realistic detector resolution, other techniques that reject background are needed. Extremely good photon vetoing leads to some six orders of magnitude of  $K_{\pi 2}$  suppression, to the point that our  $\pi^0$  detection inefficiency is dominated by photonuclear interactions in which the excited nucleus decays only to undetected neutrals. We achieve an even larger degree of  $K_{\mu 2}$  suppression through particle identification techniques. But, as with kinematics, all of these methods are eventually exhausted; only through redundancy is complete background rejection ultimately achieved.

To see that all other kaon decay backgrounds are sufficiently suppressed by our strategy we consider a few examples, but otherwise restrict the discussion to the  $K_{\pi 2}$  and  $K_{\mu 2}$  modes. Semi-leptonic decays of the form  $K^+ \rightarrow \pi^0 l \nu$  are easily rejected by either photon vetoing of the  $\pi^0$  or through particle identification due to the lack

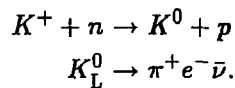
\* While it is possible to look for a signal "below the  $K_{\pi 2}$  peak," this approach is met with other difficulties and is beyond the scope of this thesis.

of a charged pion.  $3\pi$  modes are also easily rejected either through a  $\pi^0$ , the lack of a long range  $\pi^+$ , or a multiplicity of charged tracks.

Clearly, there is a fair amount of redundancy here, as each of these processes bears resemblance to the two primary modes from the viewpoint of background rejection.

A somewhat special case is the radiative decay  $K^+ \rightarrow \mu^+ \nu \gamma$ . At high muon momenta, the process is similar to  $K_{\mu 2}$  decay, where we suppress the events through particle identification and kinematics, the photon being of little consequence (indeed, the low energy photon is difficult to detect). As the initial muon momentum decreases, we still have particle identification but we begin to lose on kinematic suppression. But, this is at once linked to the rising energy of the photon which becomes easier to detect.

Additional sources of potential background arise from processes other than  $K^+$  decay. Kaon charge-exchange followed by semi-leptonic decays can lead to long range pions via the reactions



If the proton and electron are both low in energy and go undetected, and a long range pion recoils off of the neutrino, then the event could be mistaken for  $K^+ \rightarrow \pi^+ \nu \bar{\nu}$ .

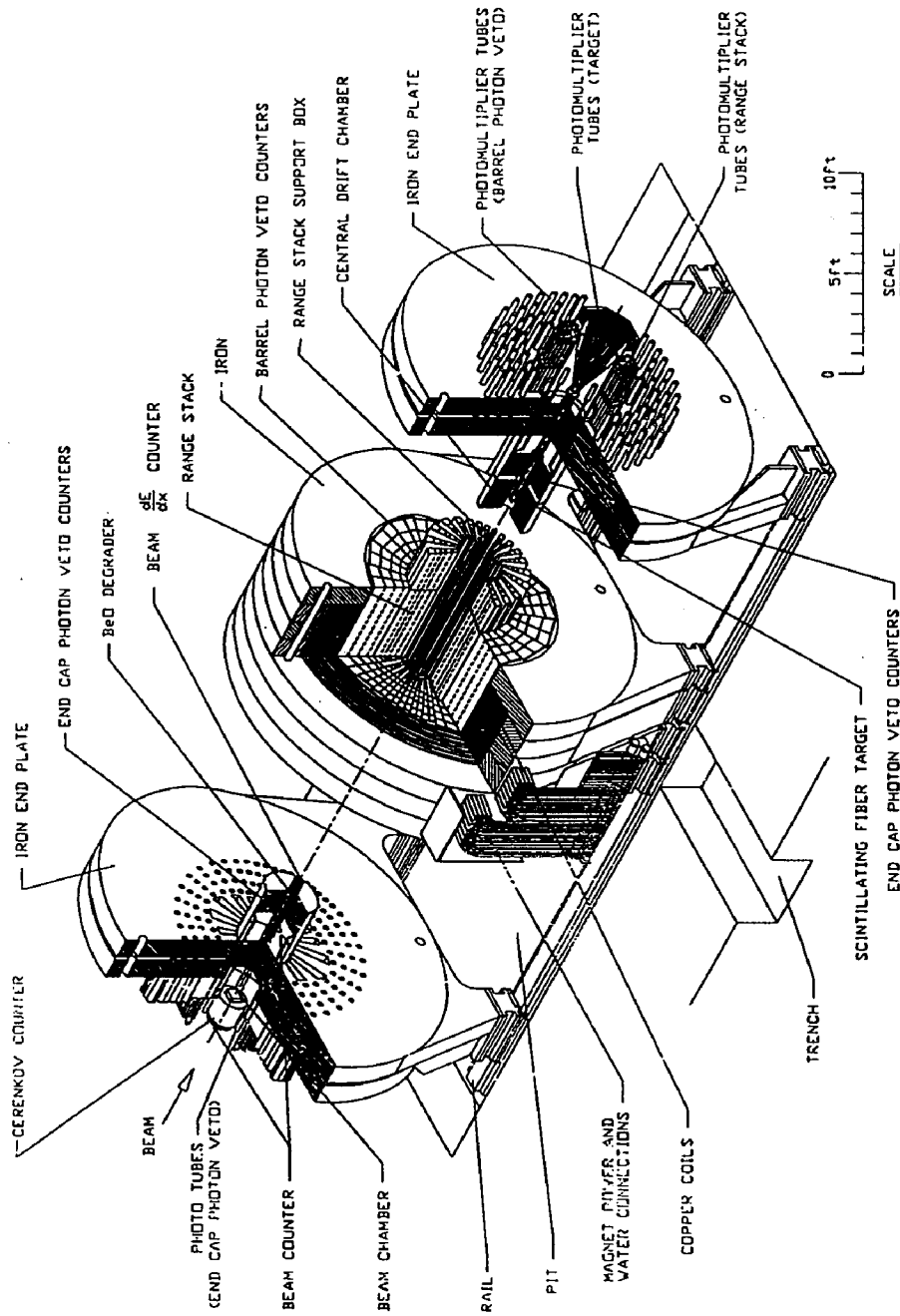
Another non- $K^+$  decay background that leads to long range pions is due to beam pions that scatter into the tracking volume. If the scattered pion enters the detector just after a kaon then it might appear to be a kaon decay product.\* Therefore, it is crucial to count and identify all incident particles.

Redundant beam instrumentation and a highly-segmented live target are used to make detailed time and position measurements of all beam and decay particles. Therefore, in either case, what is ostensibly an unaccompanied beam kaon followed by an unaccompanied decay pion can be rejected.

Before going on to describe the individual sub-systems it is useful to have an overview of detector. The philosophy of the experiment is to study a large sample of kaons in their rest frame in a spectrometer that maximizes geometrical acceptance. As with colliding beam experiments, which also work in the center-of-mass frame, practical considerations of cost and engineering lead us to a cylindrical geometry. A perspective drawing in Figure 5 illustrates this in a cut-away view of the detector.

---

\* Incidentally, a special trigger that purposely records such events provides a source of long-range pions that have proved to be invaluable in measuring detector performance.



**E-787 DETECTOR**  
BY 1968

Figure 5. A perspective drawing of the detector showing the sub-systems in a cut-away view. The magnet endplates are rolled back to the installation configuration.

Charged decay products of kaons stopped in the center of the detector are tracked over  $2\pi$  of solid angle, while photons are detected over nearly  $4\pi$ . A side-view of the detector in Figure 6 shows the location of the sub-systems drawn to scale in their final configuration.

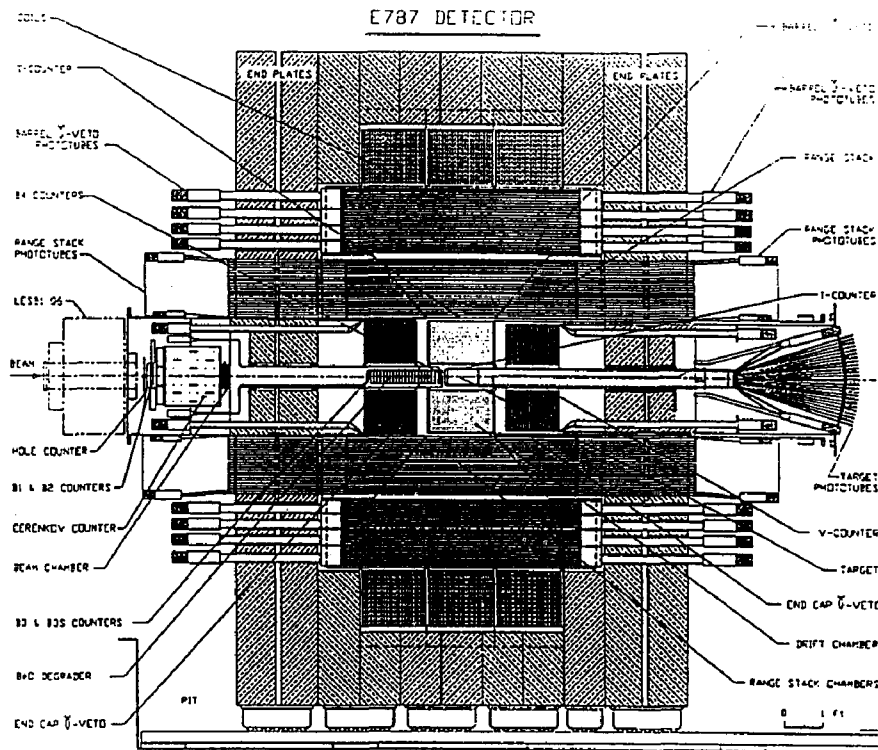


Figure 6. The final configuration of the sub-systems is drawn to scale in this side-view. The symmetry axis of the cylindrical detector is collinear with the beam.

Charged kaons from a low-energy separated beam line (LESB I) pass through a fine-grained multi-wire proportional chamber and a series of beam defining scintillation counters and hodoscopes. The  $\sim 800$  MeV/c particles are slowed by a beryllium-oxide degrader. Particle type is established by a Čerenkov counter before the degrader, and by a  $dE/dx$  measurement after. The particles come to rest in a segmented scintillating-fiber target [21] situated at the center of the cylindrical detector, the whole of which is contained in the 10 kG field of a conventional solenoidal magnet.

Decay products within a  $2\pi$  solid angle are tracked in a cylindrical drift chamber [22], before entering an azimuthally- and radially-segmented plastic-scintillator range stack, where a complete pulse shape history of all range stack phototube currents is recorded by a system of transient digitizers [23]. Range stack tracking is supplemented by two layers of multi-wire proportional chambers (RSPC's) imbedded within the stack.

Outside the range stack is a barrel-shaped lead-scintillator electromagnetic calorimeter along with two endcaps, giving nearly  $4\pi$  coverage of photon detection. Figure 7 is an end-view of the detector that shows the radial and azimuthal segmentation of the barrel veto, range stack, and endcap vetoes.

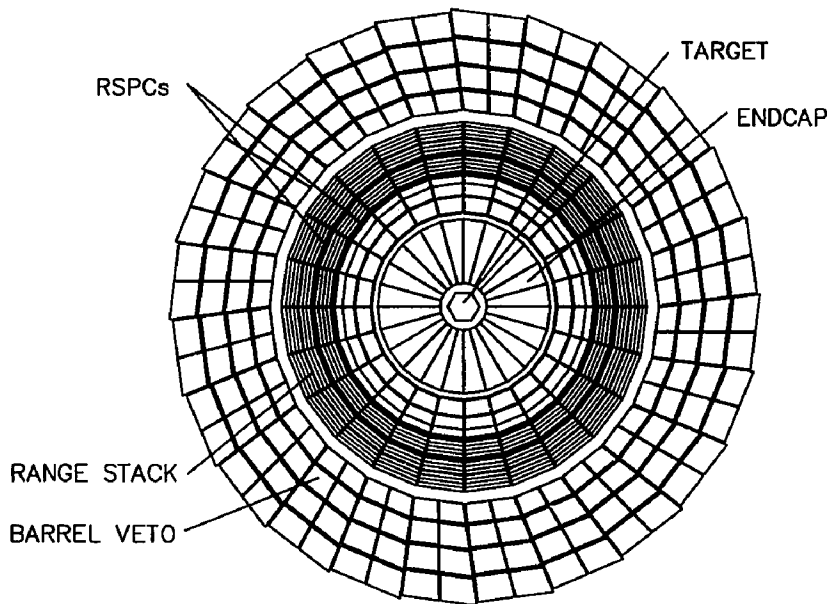


Figure 7. A detector end-view showing the radial and azimuthal segmentation. Starting at the outer radius and moving inward are the barrel veto, the range stack, the range stack proportional chambers, and the endcap vetoes. The target is shown in detail in Figure 10.

The cylindrical coordinate system is defined by the beam, which flows in the positive  $z$ -direction and is collinear with both the symmetry axis of the detector and the direction of the B-field. Thus, positive decay products emerging from the target are bent in the negative  $\varphi$ -direction, towards lower sector number. Event display pictures giving a cross sectional view are oriented with the B-field pointing

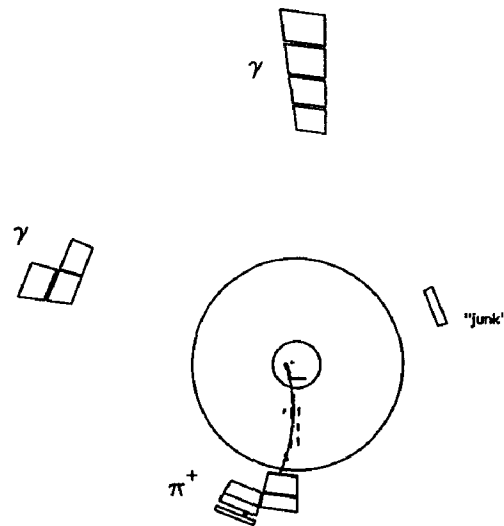


Figure 8. A  $K_{\pi 2}$  event, where the photons from the  $\pi^0$  decay are clearly visible in the barrel veto. Timing information confirms that the energy depositions in the target, range stack, and barrel occur simultaneously, and are delayed with respect to the incident kaon, and that the "junk" hit is out of time with the event. The small solid square in the range stack gap is a  $\varphi$ -hit in one of the proportional chambers.

up, out of the page. For example, Figure 8 shows a  $K_{\pi 2}$  event as it appears in the detector.

## 2.2 THE SUB-SYSTEMS

### 2.2.1 The Beam Line

A 28 GeV slowly-extracted proton beam from the Alternating Gradient Synchrotron strikes a platinum target producing a wide variety of secondary particles including protons, pions, lambdas, and of course kaons. Low energy particles given off at a production angle of  $10.5^\circ$  are captured, separated by particle type, and directed into the detector by a secondary beamline, as shown in Figure 9. The beam is extracted by the D1 magnet, a dipole septum that steers the secondary beam away from the primary beam. Quadrupole magnets Q1 and Q2 focus the extracted beam onto a second dipole which disperses the particles according to momentum.

Particle type is selected with a pair of devices called an "electrostatic separator" and a "mass slit," the heart of the secondary line. The separator, which consists of crossed E- and B-fields, transforms the 1-dimensionally momentum-dispersed beam into a 2-dimensionally dispersed beam in momentum versus velocity. This "separated" beam is focused by quadrupoles Q3 and Q4 onto the the mass slit. As its name suggests, the slit selects particles of a unique mass by passing only a narrow band in the momentum-velocity focal plane. A final pair of quadrupoles, together with a dipole, focus and direct the beam into the detector.

By careful tuning of the various parameters of the secondary line it is possible to greatly enhance the fraction of charged kaons in the beam, to the point that there is about one kaon for every two pions. Also important is the slow-extraction of the primary AGS beam which typically leads to  $2-3 \times 10^5$  kaons stopping in our target that are distributed smoothly in time over a 1.4 sec spill. This ensures that, barring accidental pile-up, we basically look at one kaon at a time.

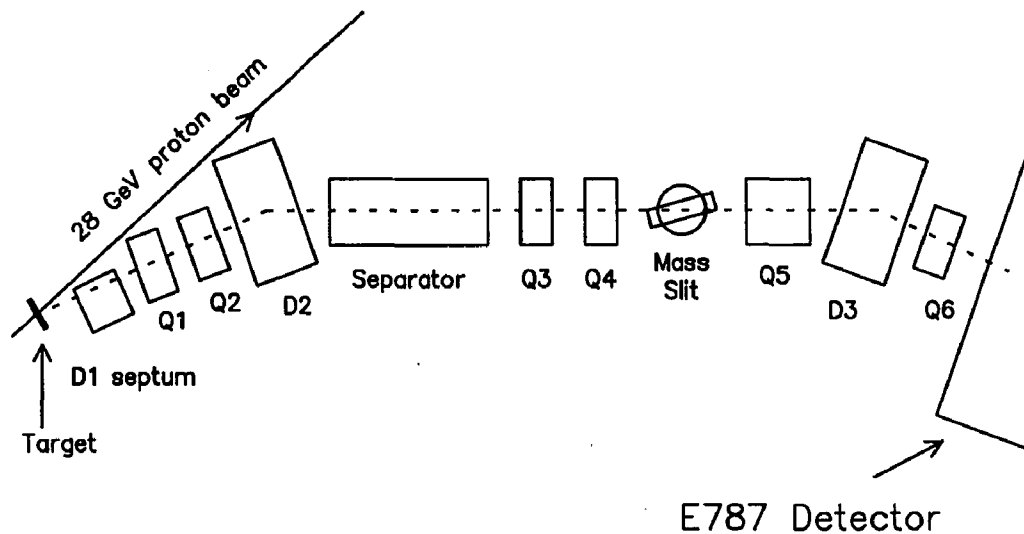


Figure 9. A schematic view of the LESB I Beamline at the Alternating Gradient Synchrotron at Brookhaven National Laboratory.

### 2.2.2 The Beam Counters

A series of beam counters, which are shown schematically in Figure 10, define the geometrical acceptance into the center of the detector and identify the incident particles.

Scintillation counters B1-B4 are read out by analog-to-digital and time-to-digital converters (ADC's and TDC's) that record their signals for offline use. In addition, discriminated versions of the signals are used "real time" in the online phase of the experiment.

Starting at the upstream end, the B1 scintillator is discriminated and scaled for use in beam tuning. It is of limited use at high rates because its single element saturates. The B2 hodoscope, with its 8 "x-fingers" and 4 "y-fingers," has greater immunity to rate saturation and has proved to be more useful for beam tuning. It can also be used offline to measure the multiplicity of beam particles entering the degrader. B3 consists of a pair of counters: a small central counter and a larger overlapping one. Also used in beam tuning, a comparison of the relative rates indicates the tightness of the beam focus near the entrance to the degrader. B4

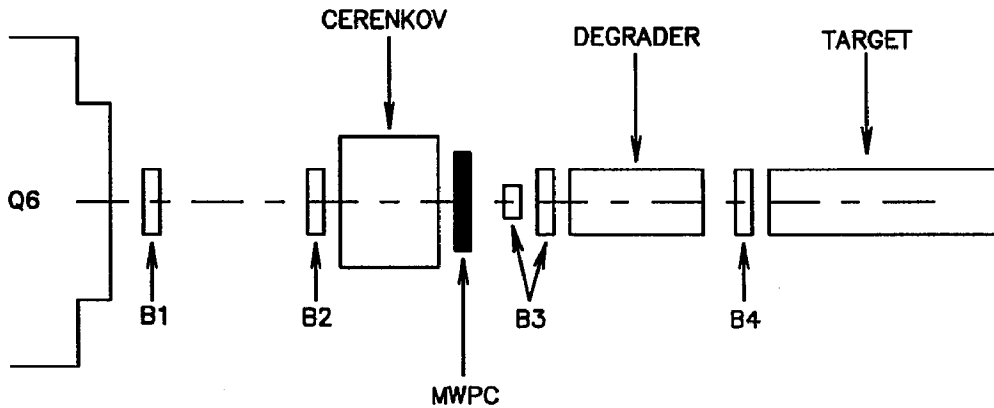


Figure 10. A schematic representation of the beam instrumentation situated between the Q6 quadrupole of LESB I and the target at the center of the detector. The dashed line indicates the beam path.

The three layers of B4, made up of a  $4 \times 4$  hodoscope (B4XY) and a single trigger counter covering the front face of the target (B4T), perform the following functions:

- B4T provides part of the beam signal for triggering.
- Beam particle multiplicities are measured both in space using the hodoscope signals, and in time by looking at a complete pulse-shape history in B4T, recorded with transient digitizers. Note that this is done *after* the degrader, therefore only the beam component reaching the target, which is considerably reduced in rate, is surveyed.

- A  $dE/dx$  measurement based on B4XY pulse height provides beam particle identification by exploiting the different ionization rates for pions and kaons which results from the slowing by the beryllium-oxide degrader.
- Photons emitted in the upstream direction leaving the front face of the target can shower in B4T, registering a hit in time with the charged track.

A double-ring Čerenkov detector, which is shown in Figure 11, is the primary method used to tag kaons and veto pions. In the selected momentum band of 750–800 MeV/c, kaons and pions have production angles for Čerenkov radiation in lucite that lie on either side of the critical angle for total internal reflection. Pion light radiated at the shallower angle is totally internally reflected, collected by a conical mirror encircling the edge of the disc, and projected onto a ring of phototubes at the appropriate radius, while kaon light is transmitted through the disc in the forward direction, refracted to a wider angle at the lucite-air interface, and focused onto a second ring of tubes by a parabolic mirror. In both cases, light collection following the mirrors is enhanced by aluminized non-imaging reflectors known as Winston cones.

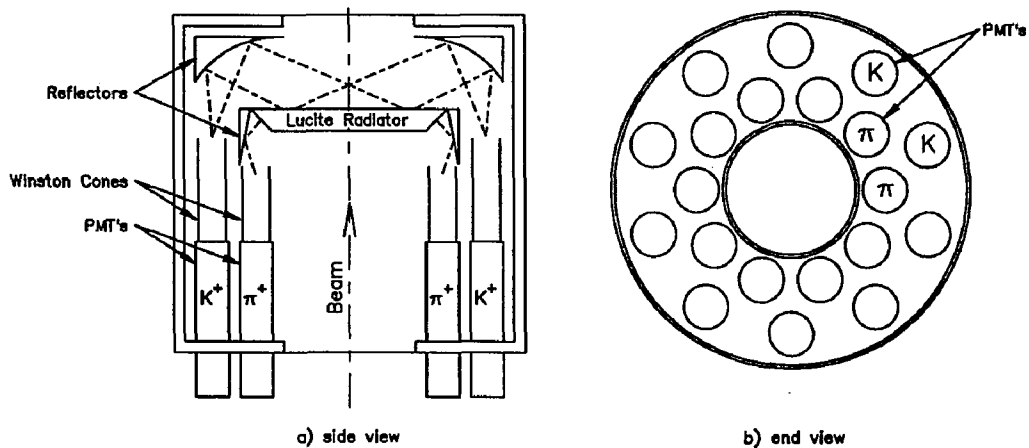


Figure 11. The Čerenkov counter: a) side and b) end views (the counter is cylindrically symmetric about the beam axis). The ray tracings on the left illustrate how pion and kaon Čerenkov light produced in the lucite radiator is separated and collected upon the inner and outer rings of phototubes on the right. There are ten tubes for each species, at radii of approximately 9 and 13 inches. The drawing is not to scale.

The readout for each ring of ten tubes is done with a multiplicity sum of discriminated signals from the individual tubes (see Section 3.3). These sums in turn are

discriminated with a threshold corresponding to a minimum of 6 struck tubes. In addition to tagging kaons, the  $\check{C}_K$  signal provides a timing reference for the event, while the  $\check{C}_\pi$  signal serves as the main defense against the “ $\pi$ -scat” background discussed in Section 2.1.

Directly downstream of the Čerenkov detector is a three-layer multi-wire proportional chamber (MWPC) that gives  $x, u$  and  $v$ -coordinates. Another check on the beam profile, the chamber can also provide redundancy on beam particle multiplicity. Although not actually used in this analysis, it could prove useful in future runs of the experiment.

### 2.2.3 The Target

After passing through B4, the kaons are brought to rest in the live fiber target made up of the 378 triangular scintillating elements, arranged in a hexagonal array as shown in Figure 12. The target elements, or simply “triangles,” are each made from a cluster of six 2-mm diameter fibers. The scintillation light is recorded with one ADC and one TDC per triangle. The fiducial region of the target is defined by two sets of scintillation counters, the I- and V-counters, as shown.

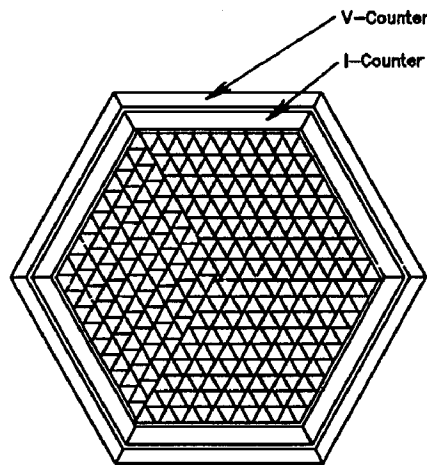


Figure 12. An end-view of the 378 triangular solids that make up the target, plus a single central fiber. The hexagonal array is surrounded by six I-counters and six V-counters that define the target volume in  $z$  (see also, Figure 15).

The combination of spatial segmentation and good timing information allow us to disentangle the decay vertex, and thus associate given triangles with the incident particle or the subsequent decay products. This is essential for making good kinematic measurements. While it is obviously necessary to have material present to stop the kaons it is also necessary to initiate kinematic measurements of the decay products as close to the vertex as possible. The segmentation also helps flag events that have a detached vertex, as is characteristic of kaon charge exchange and scattered pion events. In other words, events in which the apparent decay pion did not emerge from the charged kaon.

How we classify struck triangles as kaon or pion is illustrated in Figure 13, which shows an enlargement of the target for the  $K_{\pi 2}$  event in Figure 8. Kaon triangles are characterized by high pulse height with times near zero. The high pulse height comes about because the kaons tend to travel along the length of a fiber, and because as they stop,  $dE/dx$  becomes very large. Times are near zero by definition: a kaon that ends up in the target is first required to produce a signal in the Čerenkov counter, and it is this signal that we use to calibrate the event time. Conversely, pion triangles tend to be delayed by the kaon lifetime and they have low energy because they tend to travel transverse to the fibers.

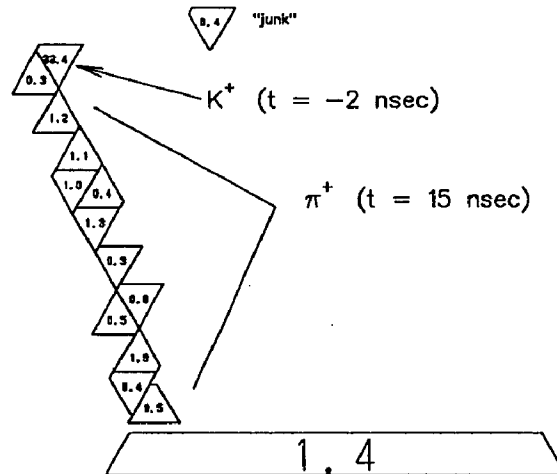


Figure 13. The time and magnitude of energy depositions in the target shows the characteristic pattern of large prompt energy for the beam particle and small delayed energy for the decay particle. The triangles are labeled in MeV of deposited energy. The "junk" hit is at  $t = 79$  nsec. For a complete display of this event, see Figure 8.

Timing resolution is improved for both the beam and decay particle by av-

eraging the triangles of each cluster or track. Kaon clusters can include several triangles, while pion tracks have as many as 10-20. The resolution is also aided by an empirical correction based on pulse height that compensates for a "time-walk" in discriminating low pulse height hits. The result, a good fit to the kaon lifetime, is shown in Figure 14.

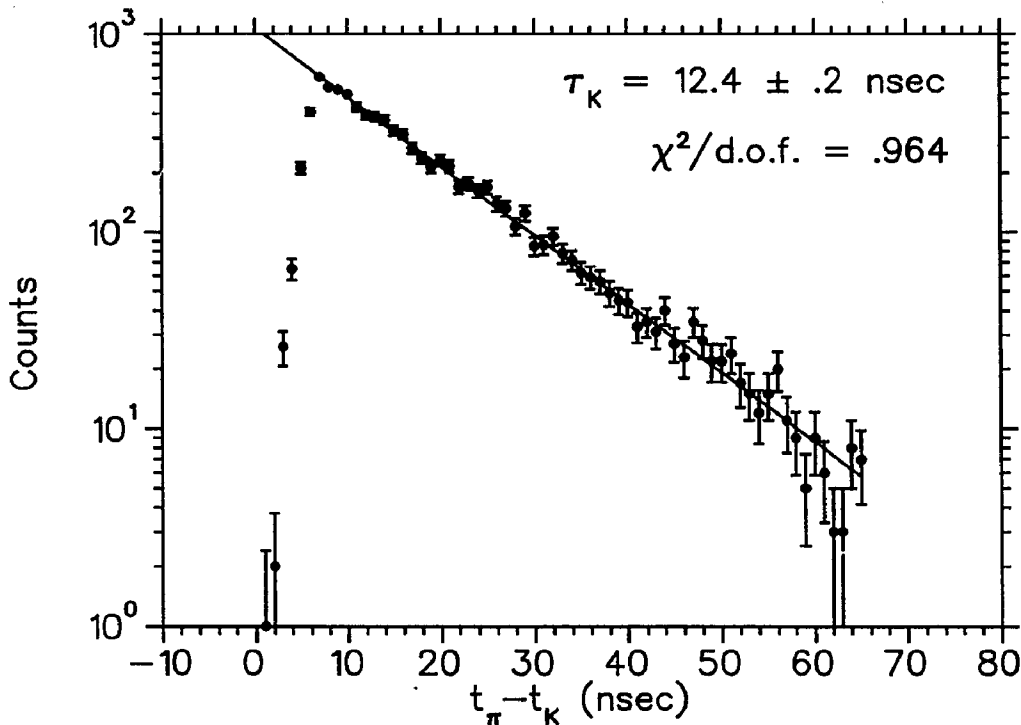


Figure 14. The kaon lifetime based on time measurements in the target. The uncertainty is the statistical error in a two-parameter fit to an exponential. The result is in good agreement with the Particle Data Group's value of  $12.37 \pm .03 \text{ nsec}$ .

Good timing information in the target lets us require a time delay between the kaon and the pion so that we can ensure that the kaon came to rest before it decayed (we call this a "delayed coincidence"). It is also important because it helps us classify the energy as kaon-like, pion-like or photon-like.

The fiducial volume of the target in the z-direction is defined by the I- and V-counters, as shown in Figure 15. This is done with external counters because the

target fibers themselves are active along their entire 3-meter length. Together with the "T-counters," the innermost layer of the range stack, we use these counters to define the maximum acceptable obliqueness, or "dip angle," for tracks originating in the target and entering the range stack.

This simple method of limiting the detector aperture at two different radii is particularly useful at the first level of the trigger. Without a limit on the dip angle, oblique tracks defeat the trigger's range measurement, which is based on the deepest layer that a track reaches, the "stopping layer." Notice that the dashed-line track clearly has a longer range than the solid-line track even though it stops in the same layer. (Without requiring both an I-counter and a T-counter,  $K_{\mu 2}$  decays, with their long range, would flood the trigger.)

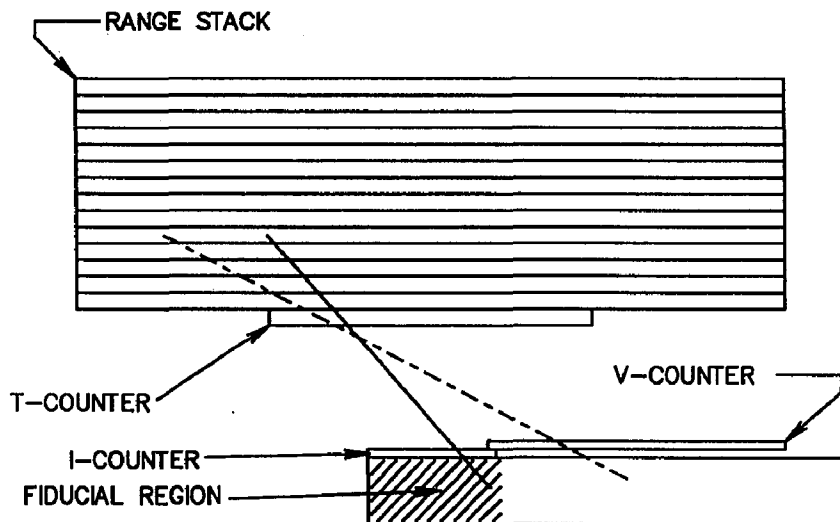


Figure 15. A side-view of the top half of the detector showing the relative positioning of the scintillation counters. Observe how the I- and V-counters define the fiducial region of the target, and the T-counter defines the entrance to the range stack. Together, they limit the acceptance angle for charged tracks, as illustrated by the solid (pass) and dashed (fail) lines. Counters are not drawn to scale.

#### 2.2.4 The Drift Chamber

The central tracking chamber is made up of five radial super-layers in a "jet-cell" geometry, as shown in Figure 16. The three odd-numbered layers, with wires

parallel to the detector axis, measure the transverse momentum of the track, while the two even-numbered layers, with wires pitched at stereo angles of  $3.1^\circ$  and  $4.0^\circ$ , measure the dip angle to correct for the longitudinal component. A correction for the degradation suffered in the target, based on target range, gives the total momentum.

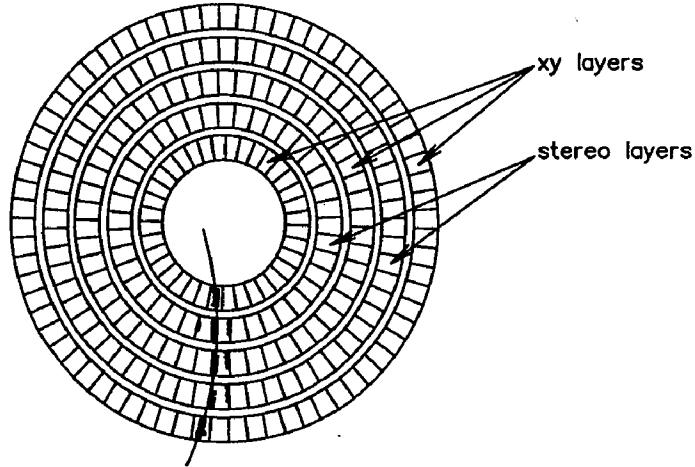


Figure 16. The drift chamber cells are patterned after five super-layers, as indicated. Also visible are the hits and a subsequent  $xy$ -trackfit for the  $K_{\pi 2}$  event in Figure 6.

In addition to measuring the momentum, the track information supplements event reconstruction in other systems. Projecting the track backwards into the target serves as a “road map” to aid in pattern recognition and fiber classification. In the range stack, directional information provided by the track fit is used as a starting point for the range measurement. The range resolution is actually worsened by the presence of the magnetic field, but there is an overall gain because range and momentum are employed together as a means of particle identification. (They are used in combination, via the *Bethe-Bloch* equation, to test a mass hypothesis; details are given in Section 4.3.6.1.)

### 2.2.5 The Range Stack

The energy, range, and decay sequence of the particles is recorded in a plastic-scintillator range stack comprised of 24 azimuthal sectors by 21 radial layers, as can be seen in Figure 7. Scintillation light is brought out of the detector in between the iron spokes of the magnet endplate that provide flux return.

Signals from the phototubes at each end that collect the light are processed as shown in Figure 17. Analog-to-digital converters (ADC's) integrate the pulse height for the energy measurement, transient digitizers (TD's) record the actual pulse shapes (see Figure 18), and discriminators provide fast signals for the trigger. The per channel cost, as well as the tremendous volume of information that issues from the TD's, requires that we multiplex every four range stack PMT's into one TD channel. A total of two-hundred channels record the activity throughout the range stack and in a selection of other counters.

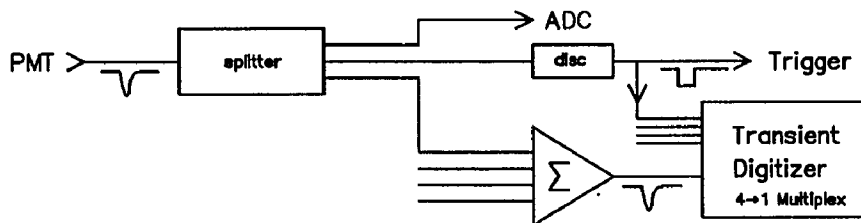


Figure 17. Range stack signals follow the path shown above. The transient digitizers record the activity for every range stack PMT sum-of-four. Corresponding discriminator signals are sampled and encoded along with the pulse shape data. These form "flag bits" that are used to de-multiplex the channels, offline.

The range stack is constructed with very little dead material in the fiducial volume so as to minimize any undetected degradation of the charged track. The  $2\pi$  angular acceptance for charged tracks is defined by the counters of the innermost layer, the "T-counters," which have a shorter active length in  $z$  than the rest of the range stack, as can be seen in Figure 15. Requiring a struck T-counter prevents us from triggering on tracks at large angles relative to the detector midplane, as they may have struck either the drift chamber endplates or the steel support structure that protrudes part way into the stack.

An enlargement of one of the 24 sectors is shown in Figure 19. Notice that the 21 layers are actually read out as 15. Optical coupling of the inner layers solves a crowding problem at smaller radii by reducing the needed number of phototubes. It also leads to a numbering scheme of T, A, B, C, 11, 12, ..., 21 for the 15 layers in each sector. Since the pions we are interested in are at the upper end of the kinematic phase space, the lack of radial segmentation in the inner layers is not a problem.

Tracking in the range stack is done using 48 multi-wire proportional chambers, the RSPC's, which are interleaved at two radii following layers C and 14. The

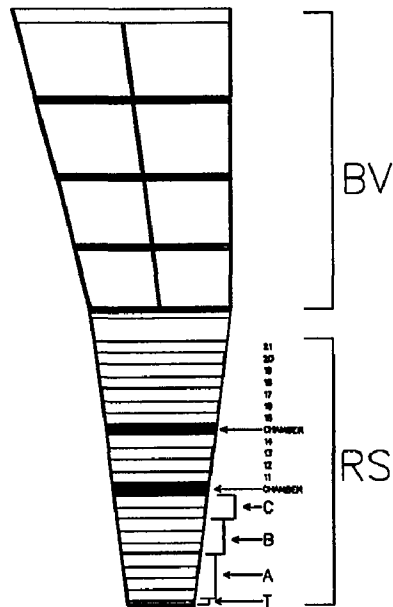


Figure 19. Cross sectional view of a one of twenty-four range stack sectors. Imbedded in the stack are two multi-wire proportional chambers that provide modest-resolution tracking in  $\varphi$  and  $z$ . Notice how layers 2–10 are grouped into the three super-layers A, B and C. Positioned directly beyond each range stack sector are two of the forty-eight sectors making up the barrel veto.

chambers are read out to give both  $\varphi$ - and  $z$ -coordinates for offline corrections to the range. The  $z$ -coordinate from the inner layer of chambers is also used to refine a range cut in the second trigger level.

To obtain sufficient muon rejection and establish with certainty that the stopping particle is indeed a pion we look for the complete  $\pi \rightarrow \mu \rightarrow e$  decay sequence using the transient digitized phototube currents, which are sampled every 2 nsec over a period of 10  $\mu\text{sec}$  [23] — this is basically like having a digital oscilloscope on each signal. The need for the high sampling frequency is dictated by the nanosecond timescale of phototube pulses and the pion lifetime, while the long time history is necessary because of the 2.2  $\mu\text{sec}$  muon lifetime. Figure 18 shows how the pulse shape data appears at one end of a range stack module in which the  $\pi^+$  from a  $K_{\pi 2}$  decay has come to rest. We refer to this module as the “stopping counter.”

In addition to the pulse shape data, the TD's provide timing information relative to a common reference signal from the B4T trigger counter. The timing information is used to tag photons that occur in time with the charged track, and to search for

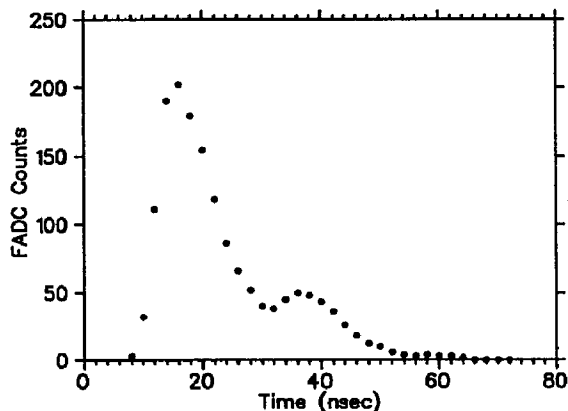


Figure 18. The transient digitizer (TD) data in the stopping counter for a  $K_{\pi 2}$  event clearly shows the two-pulse signature of a stopping particle and its subsequent decay, i.e., a  $\pi^+ \rightarrow \mu^+ \nu$  decay.

electron clusters from the muon decay.

### 2.2.6 The Photon Vetoes

Rejection of  $K_{\pi 2}$  decays is primarily achieved using a lead-scintillator “barrel” and two end-caps that together provide nearly  $4\pi$  coverage of photon detection. Barrel veto (BV) modules are composed of alternating sheets of 5mm scintillator and 1mm lead sheets with “mixer blocks” glued on at each end to facilitate light collection from the individual sheets. Figure 20 shows a schematic drawing of one end of a complete barrel veto assembly.

The counters, arranged in 48 azimuthal sectors by 4 radial layers, are supported along their entire length by a stainless steel structure built into the magnet interior. In order to prevent photons from escaping through gaps between the sectors we have employed “non-projective” geometry so that none of the gaps point back to the target. This accounts for the skewed appearance of the barrel in Figure 7.

The endcap (EC) modules are each subdivided into 24 azimuthal “petals” as shown in Figure 7. Like the barrel, they are constructed out of alternating lead and scintillator sheets. Because of limited space and the configuration of neighboring modules, the light collection system must be very compact, yet allow the light to propagate in the  $z$ -direction so that it can be extracted from the detector. We use a fluorescent “wave-shifter” bar (made of BBOT) to gather the light at the outer radial face formed by the edges of the sheets, as shown schematically in Figure 21.

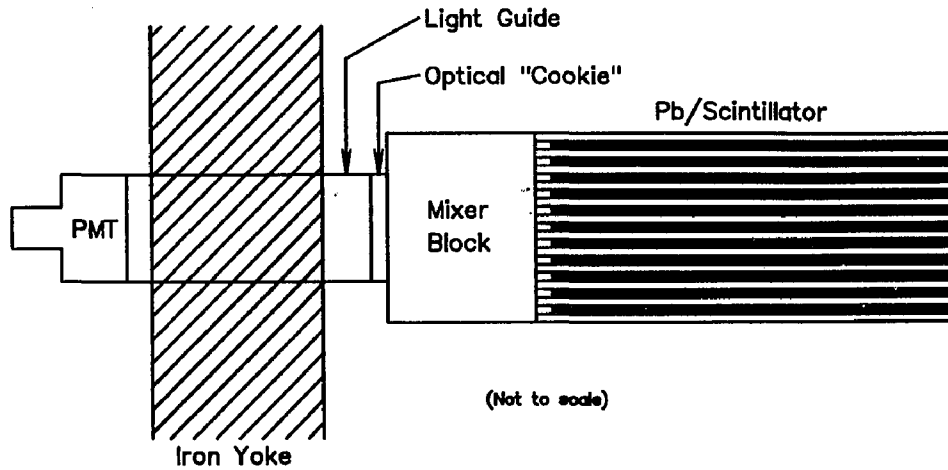


Figure 20. One end of a barrel veto module. The alternating lead-scintillator sheets are roughly orthogonal to a radius vector from the center of the spectrometer. "Mixer blocks" glued on at each end optically couple the scintillator sheets to lucite pipes that guide scintillation light through a set of holes in the magnet end-plate. The optical joint at the light guide-mixer block interface is made with a clear silicone-rubber "cookie." Both ends of the counter are instrumented with 3-inch phototubes (PMT's).

Scintillation light, which excites the wave-shifter, is thus made to "turn the corner." From there, lucite pipes bring the light out through a second set of holes in the magnet, onto 2-inch phototubes.

All barrel and endcap signals are fed into ADC's and TDC's for offline analysis. The signals are also used for online vetoing by forming total energy sums with multiple-input unity-gain summing amplifiers. These fast analog sums are then discriminated with thresholds of 5 MeV for the barrel and 10 MeV for the endcaps to distill the pulse height information down to a few digital signals for use in the trigger.\* The path of the photon veto signals is illustrated in Figure 22.

By their very nature, the online sums are a somewhat coarse measure of the true photon energy because they suffer from accidental hits. Offline, the use of precision timing lets us sum up only the energy that is close in time with the event, and thus reduce our susceptibility to accidental vetoes. Nonetheless, with the modest online thresholds indicated above enough  $K_{\pi 2}$  events are rejected by the trigger so that the data recorded to tape are dominated by  $K_{\mu 2}$  events by a factor of 10:1.

\* Conservatism demands a somewhat higher threshold for the endcap sums, which are subject to higher rates of beam-related accidental hits.

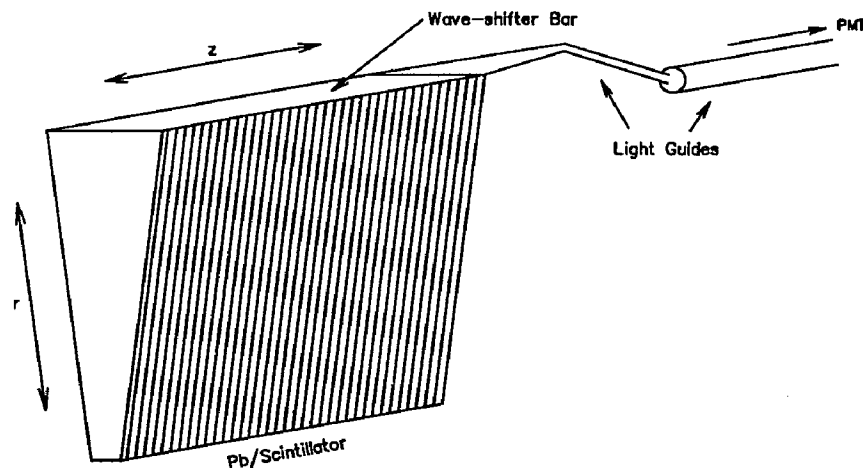


Figure 21. A perspective view of an endcap module. The compact light collection system is based on a fluorescent "wave-shifter" bar that is used to gather the light from the outer radial face and redirect it in the  $z$ -direction.

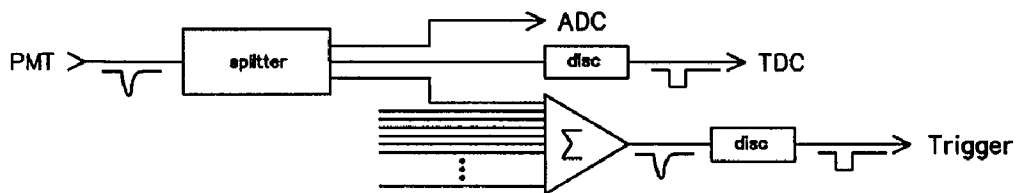


Figure 22. Photon veto signals. ADC's record the integrated pulse height in each channel for offline energy measurement; TDC's record the leading-edge time of each hit (multi-hit information is achieved by using "pipe-line" TDC's); and discriminated analog sums provide veto signals for the trigger. Separate sums are made for the barrel (384 PMT's), the upstream endcap (24), and the downstream endcap (24).

While it is impossible to completely seal a detector with many radiation lengths in all directions, we are still able to achieve extremely good  $\pi^0$  rejection because of the kinematics of  $K_{\pi^2}$  decay at rest and the geometry of our detector. The two photons from the  $\pi^0$  decay range in energy from 20 to 225 MeV, with the sum of the two constant. Even if one of the photons is low in energy and thus less likely to be detected, conservation of 4-momentum guarantees that the other is high in energy and thus all the more likely to be detected. Furthermore, given that the photons are due to a recoiling  $\pi^0$ , phase space is maximized when the more energetic photon is anti-correlated with the  $\pi^+$  and thus headed for the thickest most-favorable part

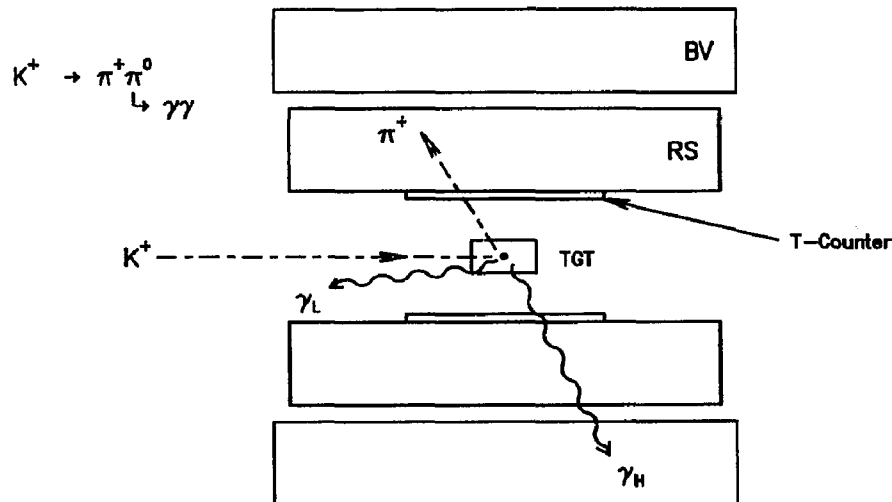


Figure 23. A schematic representation of a  $K_{\pi 2}$  event in the detector. For a  $\pi^+$  that satisfies our geometrical acceptance, the anti-correlated high energy photon ( $\gamma_H$ ) is contained by the barrel.

of the detector, as illustrated in Figure 23.

Finally, photon vetoing is supplemented by all of the other scintillation counters in the detector. It is necessary to suppress as many  $K_{\pi 2}$  decays as possible before resorting to  $\pi^+$  kinematics. Hence, the target, beam and range stack counters all enter into the offline photon veto (the range stack also contributes to the online veto).

All energy collected in time with the kaon decay but spatially separate from the charged track is used for vetoing.

### 3. The Online Event Selection

#### 3.1 INTRODUCTION

The selection of candidate events for  $K^+ \rightarrow \pi^+ \nu \bar{\nu}$  and  $K^+ \rightarrow \pi^+ f$  is based on a four-point approach, each element of which is asserted in the trigger, and more thoroughly in the offline analysis. The four elements again are:

- A kaon at rest
- Decay to a single charged pion
- No photons
- Kinematic phase space

In this chapter I describe how these fundamentals are addressed online. First, an overview of the E787 trigger is given, regarding general organization and the issues encountered in a high-rate, high-statistics environment. Following that, I treat the trigger criteria themselves, with a focus on how background events appear in the detector and how we implement various levels of online reconstruction to reject them.

#### 3.2 GENERAL ASPECTS OF THE TRIGGER

Online event selection is done in four successive levels of triggering, each level increasing in complexity and execution time, but also in sophistication and detail. A simple flow chart is given in Figure 24. The levels are numbered 0, 1, 1.5, and

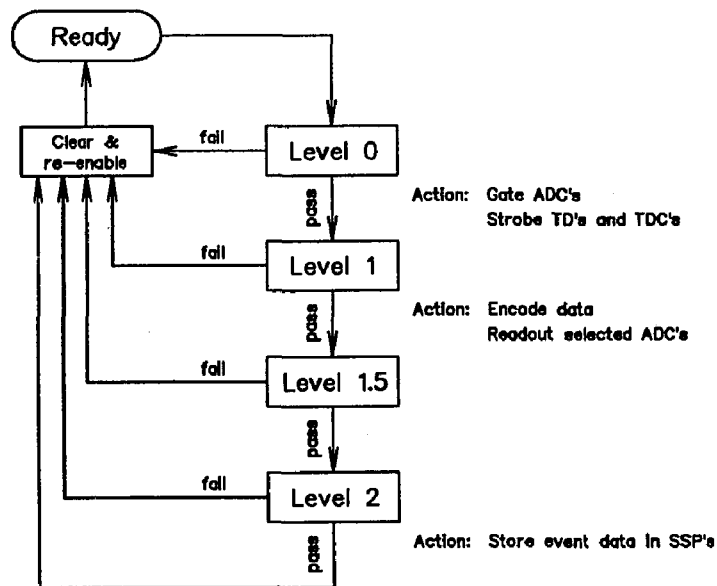


Figure 24. A flowchart for an event through the multi-level trigger. Shown at right are the data acquisition tasks at each level. During a beam "spill," which lasts about 1.6 sec, the data for events passing Level 2 are stored in local memory throughout the data acquisition system in SLAC Scanner Processor (SSP) crate-controllers. At the end of the spill a "Master" SSP reads out the data from the various crates and initiates magnetic tape writing via a host computer.

2. (We departed from integers when Level 1.5, which was originally part of level 2, was upgraded and renamed.)

Level 0 and Level 1 are based on high-bandwidth analog circuits and dedicated sequential logic. The former refers to devices like the splitter and energy-sum devices in Figure 22. The latter refers to digital circuits in which the state of the outputs are uniquely determined by the state of the inputs. There is no external clock pulse to govern the flow or transfer of information—the only delay is introduced by the propagation time of the signals themselves. The result is a very fast decision-making time. For example, at Level 0 it takes only about 200 nsec to process the signals from some 1600 phototubes in order to make decisions based on range, timing, and the presence of photons.

Level 1.5 and Level 2 are software-based triggers that use data in digital form that is generated once the event passes Levels 0 and 1. Should the event pass the higher trigger levels as well, then this same data becomes part of the offline event record. The trigger algorithms are implemented with dataways and microprocessors

that are integral to the data acquisition system. Level 1.5, for instance, uses data from the range stack and target ADC's to measure and place an upper limit on the energy of the charged track.

The trigger design makes it possible to select several classes of events simultaneously, thereby allowing us to take physics data for several different processes, as well as calibration data, all from the same exposure of kaons. Given the basic tenet of the experiment—take data at the highest reasonable rate for as much time as possible—there are several virtues to this design, especially when one considers the many parameters that determine the optimum way to run. Among these considerations are beam rate, accidental losses, reconstruction losses, rate-induced backgrounds, read out dead time, down time between runs, and setup time for special runs. Clearly, it would be difficult to make a purely analytic determination of how best to proceed, but given the issues certain strategies offer distinct advantages.

For example, calibration triggers mixed in with the main data taking streamline the overall process by reducing setup and down time. Calibration data taken in parallel is also useful because it is a natural way to average over changing conditions, both ambient and internal to the detector hardware.

Similar benefits obtain with multiple physics triggers, but with an added gain. Most of the physics triggers implemented thus far have evolved to the point where their event rates are low enough that each one by itself does not saturate the system—it does not make complete use of the available kaon flux. Combining them gives us more science by allowing each kaon the chance to fire any one of the physics triggers, with only a modest cost in additional dead time of about 1% per event written. A typical set of run-time parameters for a 1.6 sec AGS spill producing 300,000 kaons-on-target (KT's) is, on average, 25  $K^+ \rightarrow \pi^+ \nu \bar{\nu}$  triggers, 6 other physics triggers, and 2 calibration triggers, with a detector live time of 70%. The other physics triggers are drawn from the two to three available choices, the calibration, from seven to eight.

The online rejection of the  $K^+ \rightarrow \pi^+ \nu \bar{\nu}$  trigger, which is about 10,000:1, is achieved with four successive levels of selection. The remainder of this chapter is devoted to their implementation and their effect.

## 3.3 THE LEVEL 0 TRIGGER

The Level 0 trigger collects information from the various detector subsystems using fast analog circuitry and discriminated phototube signals, as outlined in Figure 25. Fast logic circuits distill the state of the detector down to some 40 digital signal lines we call "trigger bits," all of which are gathered onto a single shared dataway, or "trigger bus" [24].

In addition to fast circuitry, the trigger's performance also relies on carefully-timed narrow signals. The reference time of the event is defined by the leading edge of the signal " $T \cdot A$ ," which is defined in Figure 25. All of the other signals on the bus have their cable lengths appropriately trimmed so that their 40 nsec discriminator signals are properly defined at the time of  $T \cdot A$ .

Up to 16 different trigger states are established by independent logic circuits that simultaneously sample the state of the trigger bus. Any valid combination of trigger bits that occur at the  $T \cdot A$  time will invoke the next level of the trigger, cause various data acquisition strobes to be issued, and inhibit future  $T \cdot A$ 's.

The Level 0 trigger for  $K^+ \rightarrow \pi^+ \nu \bar{\nu}$ , which applies three of the four main strategies—all but particle ID—is defined as the state:

$$KT \cdot IC \cdot DC \cdot (T \cdot A) \cdot B_{CT} \cdot \overline{(19_{CT} + 20_{CT} + 21_{CT})} \cdot \overline{(BV + ECM + ECP)}.$$

The terms, defined below, are discussed in detail in the sections that follow:

$KT \Rightarrow$  Kaon in target ( $\check{C}_K \cdot B4 \cdot E_{\text{target}}$ ).

$IC \Rightarrow$  Struck I-counter.

$DC \Rightarrow$  Delayed coincidence between  $IC$  and  $\check{C}_K$ .

$T \cdot A \Rightarrow$  Coincidence within a range stack sector.

$X_{CT} \Rightarrow$  RS layer  $X$  in charged track region (3-sectors starting with  $T \cdot A$ ).

$BV \Rightarrow$  Barrel energy sum above 5 MeV.

$ECM \Rightarrow$  Upstream endcap sum above 10 MeV.

$ECP \Rightarrow$  Downstream endcap sum above 10 MeV.

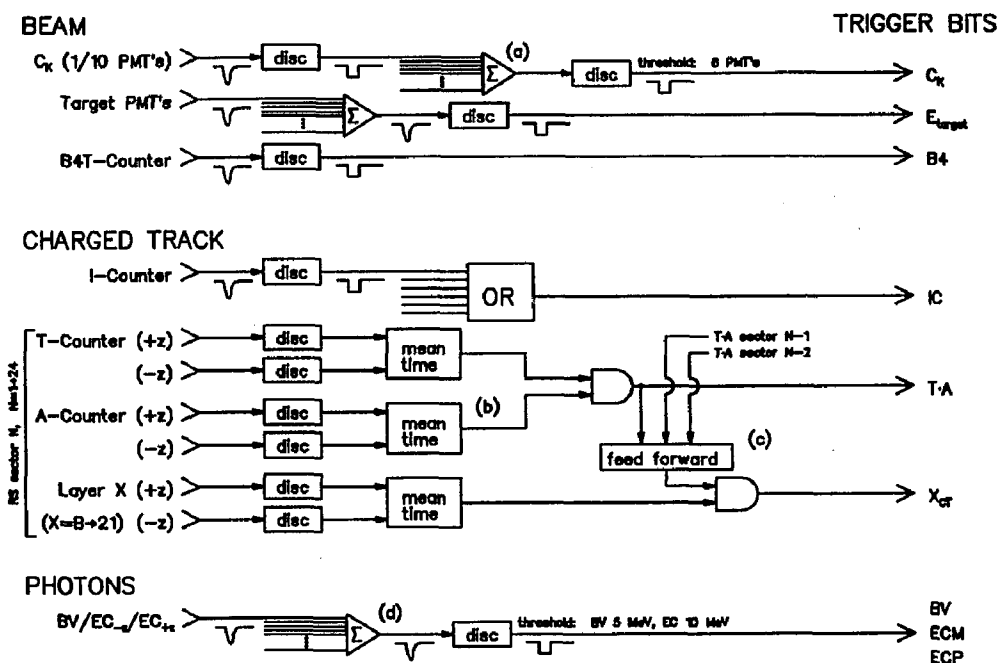


Figure 25. An overview of the signal processing that leads to the Level 0 "trigger bits." Note the following, as indicated on the diagram: (a) The Čerenkov PMT signals are first discriminated individually, then a multiplicity sum is made. A discriminator applied to the sum determines if enough tubes have fired to establish that a kaon was present. A minimum of six is required. (b) The 2 meter length of the range stack makes it necessary to take the mean time of the two ends to get good relative timing among the counters. Of particular importance is the  $T \cdot A$  signal because it sets the event time. Therefore, since the A-counters set the time of  $T \cdot A$ , they are instrumented with precision analog mean-timer circuits; mean times for the remaining layers are made digitally. (c) The "feed forward" logic deduces if a struck layer is part of a positively charged track (CT) by checking to see that its sector number is at most two less than  $T \cdot A$  (positive tracks curve towards lower sector number). (d) Separate sums are made for the barrel and the two endcaps, as discussed in Section 2.2.6.

### 3.3.1 Stopped Kaons

The only practical way to produce kaons is in flight, along with a host of other particles. The experiment rests on tagging the kaons, slowing them down, and triggering on those that stop. This accounts for the  $KT$  and  $DC$  terms in the expression above.

$KT$  is satisfied by particles that are tagged as kaons in the Čerenkov counter, pass through B4T, and reach the target. The target energy requirement, while geometric in purpose, is established by placing a low discriminator threshold on the target energy sum, sufficient only to ensure that the kaon actually entered the target. The  $\check{C}_K$  signal, in addition to particle ID, serves as a timing signal for the *beam* part of the event.

$DC$ , the delayed coincidence, refers to the relative timing of  $\check{C}_K$  and an I-counter, where the I-counter is presumably struck by kaon decay products emerging from the target. The minimum delay time of about 2 nsec, governed by the detector timing resolution, is used to suppress triggers from kaon decays in flight. Preventing such triggers is of particular importance to the online rejection of  $K_{\mu 2}$  decays, as we shall see below.

### 3.3.2 Kinematics: Fiducial Volume and Stopping Layer

$K_{\mu 2}$  decays are rejected kinematically at Level 0 by using a fast range measurement derived from the stopping layer of the track in the range stack. Ideally, in order to measure the range of particles emanating isotropically from a point, one would build a spherical detector; practical considerations, of course, dictate a cylindrical one. Therefore, to make meaningful range measurements with our detector we restrict the angular acceptance such that, roughly, tracks travel *through* the layers of the stack. We achieve this by requiring a  $T \cdot A$  signal which limits the track angle to within  $30^\circ$  of the detector midplane.

Inasmuch as the Level 0 range measurement assumes straight tracks at normal incidence to the range stack and uniform target path length, the range resolution suffers due to curvature, to tracks entering the range stack at oblique angles, and to variations in the path length in the target—all the tracks in Figure 26 have the same range, according to Level 0. Although these effects are not corrected until higher levels of analysis, the range resolution is still sufficient to reduce backgrounds significantly.

The algorithm that deduces the Level 0 range looks for charged tracks in the range stack using mean timed signals from the ends of each counter. A sector-specific  $T \cdot A$  signal enables a gate in its own sector and in the two adjacent sectors in the direction of curvature for positive tracks. Any struck layer in the three-sector region sets a corresponding bit on the trigger bus. The track shown in Figure 13, for example, enters the range stack in sector 18, crosses into sector 17, and stops in layer 11. As a result, trigger bits  $B_{CT}$ ,  $C_{CT}$ , and  $11_{CT}$  will be asserted.

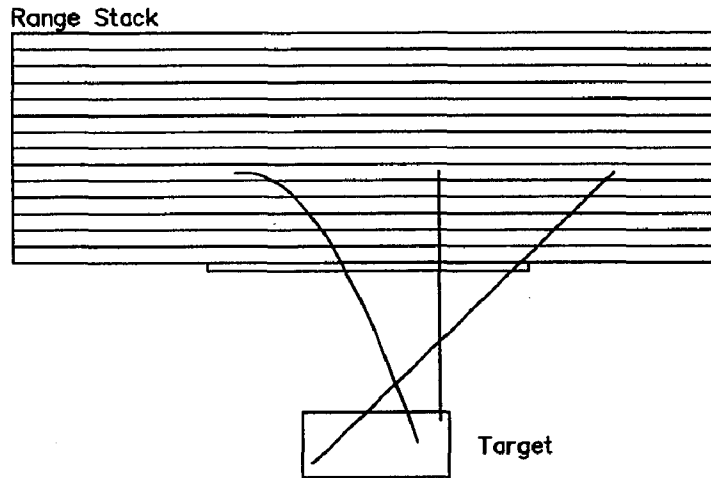


Figure 26. The Level 0 range measurement does not account for dip angle, target path length, or track curvature—all tracks shown give the same result, i.e., they have the same stopping layer. The curved track is meant to represent a helix viewed from the side, which is itself only an approximation to the trajectory of a charged particle slowing down in the presence of a magnetic field. Nonetheless, it does illustrate how a particle that is “turning over” in a counter can have a path length significantly longer than the counter’s thickness.

By interrogating the  $X_{CT}$  bits, the  $K^+ \rightarrow \pi^+ \nu \bar{\nu}$  trigger places limits on the minimum and maximum allowed range. Requiring layer *B* rejects virtually all  $K \rightarrow \pi^+ \pi^+ \pi^-$  decays, the most energetic pions from which have a range of 8.4 cm. Thus, even tracks that leave from the edge of the target and strike the range stack at normal incidence will not go beyond layer *A*—the total thickness of the *I*, *T* and *A* counters is 9.3 cm; besides, the tracks are curving in the magnetic field so not all of their path length extends in the radial direction.

At the high end we veto on layers 19–21. This suppresses  $K_{\mu 2}$  decays with a rejection factor of 10:1, with the veto placed just beyond the  $K^+ \rightarrow \pi^+ \nu \bar{\nu}$  endpoint. In the previous section we mentioned that  $K_{\mu 2}$  decays in flight tend to defeat the veto. This is because the decay muon receives a negative boost in the lab frame if it decays in the backward direction, thus allowing it to stop short of layer 19—herein lies the importance of the delayed coincidence requirement in the trigger.

It is perhaps interesting to note that this very effect is used to tune the delayed coincidence. The delay time, which is set with a length of cable, is trimmed in half-nanosecond steps until a sudden rise is observed in the trigger rate—that due to  $K_{\mu 2}$  decays in flight. Restoring the last section of cable sets the operating point.

### 3.3.3 The Barrel and Endcap Photon Vetoes

The Level 0 trigger is completed by vetoing photons in the barrel and the endcaps. The *BV* line on the trigger bus is set by applying a 5 MeV threshold to the analog sum of all channels in the barrel, as illustrated in Figure 25. The endcaps are treated similarly, but with a 10 MeV threshold applied to analog sums at each end. This sets the corresponding lines for the upstream (*ECM*) and downstream (*ECP*) ends. If any of the three bits is "true" the event is vetoed. The more conservative threshold on the endcaps serves to minimize the accidental losses caused by the beam halo, which is more pronounced there than in the barrel.

## 3.4 THE LEVEL 1 TRIGGER

The level 1 trigger consists of a photon veto that looks for showers in the range stack, as well as further kinematic suppression based on an improved range measurement. With rejection of both  $K_{\pi 2}$  and  $K_{\mu 2}$  decays, we achieve an overall reduction factor of 15:1 with a dead time contribution of about  $7\mu\text{sec}$  per event.

### 3.4.1 The Hextant Photon Veto

The range stack is approximately one radiation lengths of matter situated in front of the barrel and is therefore important to online rejection of  $K_{\pi 2}$  decays. By dividing the range stack into hextants, we can recognize photon showers as blobs of energy that are distinct from the  $\pi^+$  track. Fortunately, owing to the anti-correlation of the  $\pi^+$  and the  $\pi^0$  in  $K_{\pi 2}$  decay, the photons tend to shower far enough from the  $\pi^+$  so that a division by hextant gives sufficient separation to isolate and tag the extra energy. For example, if the high-energy photon in Figure 23 showered in the range stack, the energy would be easily tagged.

Reduction of the range stack signals to six "hextant bits" is accomplished by discriminating a fast analog sum of the total pulse height within each hextant, as shown in Figure 27. The pattern of bits is compared against what we expect for a clean single track, a single cluster that is at most two hextants wide. The trigger decision for each of the  $2^6$  possible bit patterns is programmed into a Memory Look-up Unit (MLU),\* accessed by the address word formed by the hextant bits, and passed on to the trigger control boards, where it awaits the second part of Level 1.

---

\* An MLU is a multiple-bit digital memory into which predetermined data is loaded before application time. An individual datum can then be quickly and directly accessed according to its specific address. Fast pattern recognition, as described here, is a typical application.

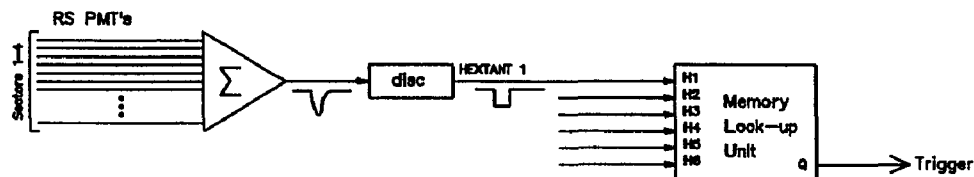


Figure 27. "Hexant bits" are formed by summing the pulse height in every four sectors and discriminating the result with a threshold of about 10 MeV. The six bits are used to access a pre-loaded trigger decision stored in a "Memory Look-up Unit," or MLU.

### 3.4.2 The Refined Range Trigger

The online range measurement is enhanced by applying some of the corrections mentioned in Section 3.3.2, thus improving the separation between  $K_{\mu 2}$  muons and the  $K^+ \rightarrow \pi^+ \nu \bar{\nu}$  endpoint and allowing more rejection. As with the hexant veto, detector information is reduced to an MLU address where the trigger decision is pre-determined for each possible address, and programmed into the corresponding memory location. We apply corrections for the path length in the target and the incidence angle in the range stack so that the tracks from Figure 26, which had the same range at Level 0, are rendered distinct at Level 1.

The 12-bit MLU address consists of three 4-bit sub-addresses, as shown in Figure 28. The first, carried over from Level 0, is a digital version of the stopping layer. Derived from the  $X_{CT}$  lines of the trigger bus, it is a binary value corresponding to the deepest struck layer in the charged track.

The second sub-address is a correction for the dip angle, determined by the absolute value of the track's  $z$ -position at the inner range chamber. The  $z$ -coordinate is determined with the chamber cathodes, which are etched into a serpentine-pattern transmission line running in the  $z$ -direction. The basis of the measurement lies in comparing the signal's arrival time at the two ends of the chamber. To extract a fast measurement for use in the trigger we transform the timing signals into a 4-bit determination of  $z$  with a time-to-amplitude converter and a "Flash" ADC. To ensure that a chamber was penetrated we require a hit in layer 11 of the range stack, just beyond the chamber.

The third sub-address accounts for the target's contribution to the path length. To extract a fast measurement we approximate the range by the number of struck elements in the target. We start with an analog version of this by making a multiplicity sum of all target discriminator pulses, which is then flash encoded such that a full-scale reading on a 4-bit Flash ADC corresponds to about 30 cells, the full width of the target.

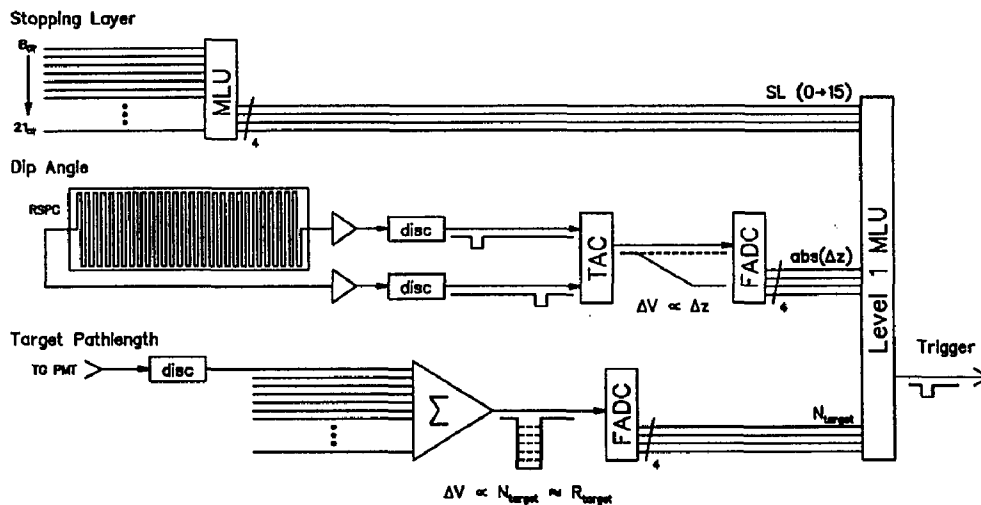


Figure 28. The Level 1 "Refined Range" trigger is based on the RS stopping layer, the track dip angle based on an RSPC  $z$ -measurement, and a target path length correction based on the number of struck target elements. Digital versions of each quantity combine to form an MLU address which accesses a pre-loaded trigger decision.

The complete address of 12-bits is used to access the trigger decision in the Level 1 MLU, which is programmed to reject long range tracks. Roughly, for a given stopping layer, an event is more likely to fail if it has a large  $|z|$  or has many struck target elements.

### 3.5 THE DATA ACQUISITION SYSTEM

Before describing the higher level triggers we digress for a brief discussion of the data acquisition system, on which they depend. The system, which is described in Figure 29, has an extremely high data transfer rate of 140 kbyte/sec.\* It also has microprocessors distributed throughout that are programmed to partially analyze the data before deciding whether or not to write it to tape. This allows us to establish further selection criteria in order to reject more events online.

The Level 1.5 trigger uses data from the analog to digital converters (ADC's) by accessing the high-speed bus (see figure) with special logic modules that sum the

\* This gives us the capability of recording about 45 events per 1.6 sec spill, each 10 kbytes in length; the data are buffered so that readout continues between spills.

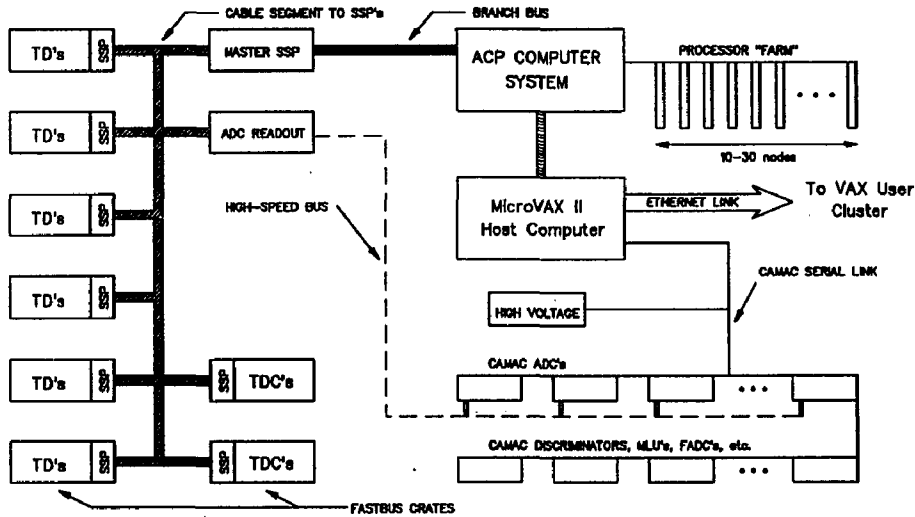


Figure 29. The E787 data acquisition system is based on the FASTBUS standard of computer-controlled crate electronics. Data are transferred over a cable segment from crate-controllers (SLAC Scanner Processors or SSP's) to a master crate, which communicates in turn with a host computer. Along the way some data reduction is performed in a processor "farm," where whole events are each analyzed in parallel by a set of independent nodes, all executing the same program. ADC's and other assorted modules in the CAMAC standard are controlled directly by the host computer; data from the ADC's, where digital readout speed is of prime importance, are transferred to FASTBUS via a customized high-speed data bus and interface.

energy in the charged track. We reject  $K_{\mu 2}$  decays by setting a maximum allowed energy just above the  $K^+ \rightarrow \pi^+ \nu \bar{\nu}$  endpoint. At Level 2, data from the transient digitizers (TD's) are analyzed by microprocessors directly within the crates in which the data were taken. The TD algorithm, which is described in Section 3.7, further suppresses  $K_{\mu 2}$  events by looking for the absence of the (pion) double-pulse signature shown in Figure 18.

## 3.6 THE LEVEL 1.5 ENERGY TRIGGER

The Level 1.5 trigger achieves a factor of 2 in  $K_{\mu 2}$  rejection by imposing an upper limit on the kinetic energy of the charged track using ADC information that ultimately becomes part of the offline event record. Energies in selected counters of the range stack and target are summed according to the scheme outlined in Figure 30.

The charged-track region in the range stack is defined as a three-sector wide swath determined by  $T \cdot A$  information from Level 0. The definition is made unique by requiring one-and-only-one  $T \cdot A$ \*. The address part of each ADC data "word" is checked to see if it is in the track region. Only then is it included in the sum. Target elements are selected by requiring that they have less than 2 MeV of energy. As illustrated by the pulse-height pattern in Figure 13, this is a simple way of choosing hits in the decay track.

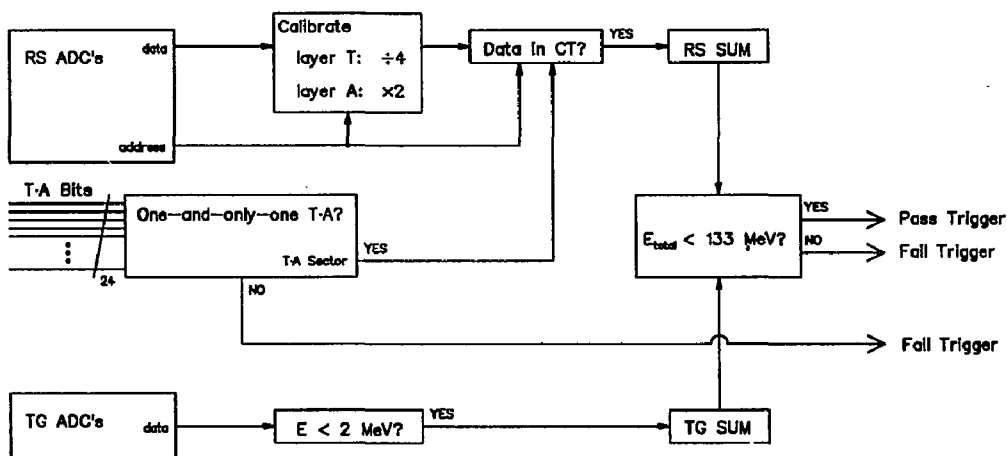


Figure 30. A block diagram illustrates the elements of the Level 1.5 energy trigger. ADC data for the range stack and target are summed in Arithmetic Logic Units, or ALU's. These are electronic devices that make fast running-sums of binary data applied to their input lines.

A system wide calibration of 32 ADC counts/MeV is assumed, based on a nominal range stack calibration of 16 counts/MeV/end (adding the two ends gives 32

\* This does not represent a significant loss for single charged-track events *without* photons.

counts/MeV). Although no counter-specific corrections are made, layer-specific corrections are needed for the  $T$  and  $A$  counters because their gains differ from the nominal setting. Smaller phototubes in layer  $T$ , which are capable of about only half the nominal *tube* gain, are compensated with  $8\times$  amplifiers for an *overall* gain of 64 counts/MeV/end. Thicker counters in layer  $A$  are run at half the nominal gain to avoid saturation effects. Prior to summing, appropriate division or multiplication is performed in digital circuitry by bit-wise shifts of the binary data.

Several items cause the online energy to be underestimated: The I-counters are not included in the sum, the target calibration is 22 counts/MeV,<sup>†</sup> and saturation in the scintillator is not corrected for. Although these add up to about a 10% shift in the energy, the variation in each quantity can be safely ignored as a higher-order effect. Also, since the maximum allowed energy is determined empirically, relative to the online measurement of the  $K_{\pi 2}$  energy, the shift is not a concern, either.

### 3.7 THE LEVEL 2 $\pi \rightarrow \mu$ TAGGER

The Level 2 trigger runs a program called TDPION, which analyzes transient digitizer data from the stopping counter to search for a  $\pi \rightarrow \mu$  decay. The program is executed with the microprocessors in the SSP crate-controllers and is based entirely on software processing of the detector information in digital form. A factor of 7 in muon rejection is realized.

The stopping counter is deduced by the state of the trigger bits from Level 0 and Level 1. The bits are recorded, or "latched," by a set of registers called "I/O boards," which are accessed by Level 2 to determine the stopping layer via  $X_{CT}$  bits, and the stopping counter via hexant bits.<sup>‡</sup>

Figure 31 illustrates typical stopping counter activity for (a) pion and (b) muon events. TDPION distinguishes the cases by looking at two quantities, the peak height and the total pulse area, both of which lend themselves to efficient computation. The area expected for a single-pulse event, which is predicted based on the peak height, is compared to the measured area. An excess in the measured area indicates the double-pulse signature of a stopping pion because a second pulse sitting

<sup>†</sup> A correction for non-scintillating material (glue) has already been made—ADC counts  $\div$  22 yield "true" MeV.

<sup>‡</sup> The 4-to-1 multiplexing of range stack signals into a TD channel is done by summing the four signals in a given layer and hexant. Therefore, inasmuch as the trigger ignores the de-multiplexing flag bits, the particular "stopping counter" within the hexant need not be specified—it is enough simply to know the hexant.

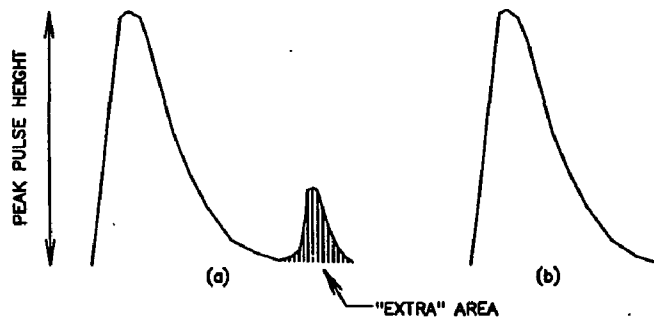


Figure 31. A sketch of stopping counter activity for (a) pion and (b) muon events. Notice how the second pulse in (a), which is due to a  $\pi \rightarrow \mu$  decay, contributes to the area but not the peak height. This is exploited by the TDPION trigger routine. Note that the typical pulse width of 20 nsec is comparable to the pion lifetime of 26 nsec. Therefore, early pion decays may not produce a distinct second pulse.

on the tail of the first affects the total area but not the peak height, as shown in (a).

Two cases that cause the algorithm to break down are overflows due to large stopping pulses, and early  $\pi \rightarrow \mu$  decays. In the former case, the true peak height is not recorded and as a result, large single pulses will appear to have extra area. Therefore, we reject overflow events outright. In the latter case, the early muon pulse tends to add to the peak height, not just the area. Since this raises the expected area, the event appears to have only one pulse. Both effects are intrinsic limitations in detecting the double-pulse signature that are not specific to the online analysis. Furthermore, the loss of efficiency due to overflows is small because this seldom happens for "normal" events.

The two ends of the stopping counter are analyzed in succession and both are required to pass. If the first end fails then the event is immediately aborted for a savings in execution time of 30%, or 160 out of a total of 540  $\mu\text{sec}$ . If both ends pass, then the end of the trigger chain has been successfully reached and the event is recorded for offline analysis.

## 4. The Offline Analysis

### 4.1 INTRODUCTION

Data taken over a period of three months in the Spring of 1989 led to approximately 1700 standard 6250-bpi half-inch data tapes containing about  $10^7$   $K^+ \rightarrow \pi^+ \nu \bar{\nu}$  triggers. Starting with the assumption that most (or perhaps all) of these are background, the task is to subject the data to a detailed offline reconstruction program that allows the application of "cuts" that distinguish signal from background events. The program was applied in several "passes" through the data, eliminating a fraction of the events at each stage. Thus, data summary tapes from each pass do not contain a compact or reduced summary of each event, but rather complete event information for a subset of the data—those events that have not *yet*\* been rejected as background.†

The program consists of an analysis "shell" developed specifically for E787 called KOFIA (Kaon OFFline Interactive Analysis). It consists of a number of standard reconstruction analyses for the various sub-systems, providing the user with quantities such as track momenta; range, energy and times of tracks in the target and range stack; energy of individual hits and their associated times throughout the detector (useful for finding electrons from  $\mu^+ \rightarrow e^+$  decays, or photons); position information based on chamber hits or extrapolations thereof; and pulse shape data from the transient digitizers (TD's). Basically a utility program, KOFIA leaves it to the user to develop and implement analysis subroutines, define and plot quantities of interest, and decide which events to cut and which to keep for further scrutiny. It also supervises use of calibration data, and accumulation of scaler data for beam flux measurements and normalization. It allows for batch and interactive processing and can be run on a number of different computer systems.

\* No  $K^+ \rightarrow \pi^+ \nu \bar{\nu}$  candidates were found in this sample.

† Results from some of the more CPU-intensive steps are saved along with the "skimmed" events.

The remainder of this chapter is divided into three parts. The first gives a general description of the analysis passes, the second provides details of cuts that were applied, and the third summarizes the cuts along with their rejection factors.

## 4.2 THE ANALYSIS PASSES

The analysis consisted of four "passes" through the data. Except for Pass 0, which sorted the various types of physics and calibration events, each pass reduced the number of events in the overall sample. (Recall that several trigger criteria were simultaneously active during data taking; all triggered events were recorded in the same physical output stream, hence the need to sort.) Table 1 summarizes what was done at each pass, along with the number of surviving events. Following the table, the passes are described in more detail.

The availability of analysis code and calibration constants, as well as the optimization of rejection versus CPU time, influenced the order in which cuts were applied. Also, depending on the previous set of cuts, the sample is dominated by a particular type of background event, making certain cuts more effective. For example, raw data is dominated by  $K_{\mu 2}$  decays so in Pass 1 we concentrate on particle identification, whereas after Pass 1 the sample is dominated by  $K_{\pi 2}$  decays so we concentrate on photons. In a number of cases loose versions of cuts were applied at earlier passes to give us leeway in the final placement of cuts in later passes after more precise calibration data had been analyzed. This allowed us to optimize the acceptance and minimize the chance of having to re-run the more labor-intensive earlier steps.

The main purpose of the Pass 0 analysis was to put the nearly 1700 raw tapes of mixed triggers into a more manageable form. This was done in two major steps. The first step, run on the IBM 3090 at BNL, served to sort the various trigger types into separate disk files. Files of a given type were then copied back on to half-inch tape. All special records, *i.e.*, non-event data, such as scaler information read out at the end of each beam spill, were kept in each of the output streams. The second step consisted of copying the sorted tapes onto 8-mm video cassettes—this was done mainly at BNL and Princeton, wherever and whenever a half-inch and an 8-mm drive were available on the same system.

By going through the run-time log books, we compiled a list of problem-free runs to be analyzed. This ultimately led a set of 65 8-mm cassette tapes. As subsequent passes were performed we were able to determine which of the runs in the original list had been lost along the way, for example, due to operator errors in running Pass 0. Approximately 60 remaining runs were recovered, leading to a

Summary of the Passes		
Pass	Analysis Performed/Cuts Applied	# Events Surviving
Pass 0	Select $K^+ \rightarrow \pi^+ \nu \bar{\nu}$ triggers. Compress TD data.	$\sim 10^7$
Pass 1	Track reconstruction in target, drift chamber, and range stack. TD and kinematic pion identification.	859134
Pass 2	Loose photon veto, beam and fiducial cuts. Delayed coincidence. TD pion identification.	13720
Pass 3	Secondary photon veto, beam and fiducial cuts. "Quality" cuts on reconstructed track. TD and kinematic pion identification. $\mu^+ \rightarrow e^+$ tagging.	2051
—	Final spectrum cut ( $E/P/R$ ).	0

Table 1. Summary of the analysis in the various data reduction passes. The final spectrum cut, which defines the allowed kinematic region for the charged track in momentum, energy and range, is used to extract branching ratio upper limits on  $K^+ \rightarrow \pi^+ \nu \bar{\nu}$  and  $K^+ \rightarrow \pi^+ f$ .

total of 69 cassettes and an overall yield of 99.5%. Pass 0 also yielded 33 cassettes of calibration triggers, and an assortment of other physics triggers. Data were taken to study the processes  $K^+ \rightarrow \pi^+ \mu^+ \mu^-$  [25] and  $K^+ \rightarrow \pi^+ \gamma \gamma$  [26], as well as a search for  $K^+ \rightarrow \pi^+ \nu \bar{\nu}$  in the kinematic region below the  $K_{\pi 2}$  peak.<sup>†</sup>

The goal of the Pass 1 analysis was a modest rejection factor of 10:1 using a simple set of well understood cuts. Basic track reconstruction was performed in the target, drift chamber and range stack, and we required that only a single track was found. Loose spatial cuts were applied to ensure that the three sub-systems were, in fact, reconstructing the same track. Again, since the raw triggers are dominated by  $K_{\mu 2}$  decays, particle identification cuts are the most effective way to reduce the number of events. Both TD and kinematic cuts were used.

Identical versions of the Pass 1 program were run at Princeton and TRIUMF, with about half of the data being processed in each country. Couriers were then sent to the border for a simultaneous exchange of the resulting output tapes. Pass 1 yielded nearly 900,000 events occupying fifteen 8-mm cassettes. (A summary of the

<sup>†</sup> The references are for results from our 1988 run; more data were taken in 1989 and 1990 for each process and are now being analyzed.

cuts for all three passes is given in Section 4.4.)

The next pass through the data, Pass 2, was run three times. The goal of the earliest version was to develop an analysis with a rejection of about 50:1 so that we could quickly get down to a small sample to see if there were any major sources of background (or signal!) in the data. None was found. The subsequent versions benefitted from a more considered development of cuts, better efficiency studies, and improved calibration.

Pass 2 emphasized three main strategies.  $K_{\pi 2}$  decays were suppressed by tagging photon energy throughout the detector with a lower veto threshold than what was used in the trigger, “ $\pi$ -scat” events (see Section 2.1) were vetoed on beam pion activity as recorded by the Čerenkov counter, and  $K_{\mu 2}$  decays were rejected by tighter TD particle identification cuts. The TD analysis includes a cut to suppress early  $\mu^+ \rightarrow e^+$  decays that mimic a pion signature.\* The final version of Pass 2 reduced the Pass 1 data set by a factor of 62:1, down to a sample of about 14,000 events.

At this point the sample was small enough to conveniently store on a hard-disk storage device where we proceeded to develop and optimize the Pass 3 cuts. Half of the cuts are simply tighter versions of those already applied, making the list of cuts deceptively long. The other half, which appear for the first time, complete our ensemble of beam and photon veto cuts. They reject events that happen to be in the “tails” of distributions already cut on, or they deal with potential background scenarios that have not yet been covered. In addition, the Pass 3 cuts further define the fiducial region of the detector to ensure that kinematic quantities are reliably measured.

Finally at Pass 3, we require a  $\mu^+ \rightarrow e^+$  decay. Paradoxically, this helps reject  $K_{\mu 2}$  events. To see this recall that we have already made very stringent demands that there be a two-pulse  $\pi^+ \rightarrow \mu^+$  signature. If the two-pulse signature is actually due to the decay of a  $K_{\mu 2}$  muon, then that same muon will not be able to later satisfy the  $\mu^+ \rightarrow e^+$  requirement. Barring accidentals, only stopped pions are capable of producing the complete three-pulse signature.

2051 events survive the Pass 3 analysis. These are dominated by  $K_{\pi 2}$  decays in which the photons have gone undetected, along with a small number of what are likely  $K_{\mu 2}$  decays that have a spurious pion signal. The number of surviving  $K_{\pi 2}$  events corresponds to a  $\pi^0$  detection inefficiency of  $10^{-6}$  and is consistent with

---

\*  $\mu^+ \rightarrow e^+$  decays in the first  $\sim 120$  nsec can appear to have a double-pulse signature in the stopping counter.

that predicted by Monte Carlo simulation.<sup>†</sup> The inefficiency is dominated by photo-nuclear reactions in which the de-excitation products are neutral and go undetected.

A final set of cuts are applied to the sample in order to define the allowed kinematic region for rare events. As noted earlier, to distinguish signal from background with certainty, we search only for events in which the kinematics of the  $\pi^+$  lie between those of the charged particles from  $K_{\pi 2}$  and  $K_{\mu 2}$  decays. Cuts are applied in momentum, energy and range. Their effect is illustrated by plots of range versus energy for the Pass 3 survivors, shown before and after the momentum cut in Figure 32a–b. As suggested by the figure, which shows the energy and range cuts, we refer collectively to all three as the “Box” cut. In selecting, *a priori*, the uppermost portion of the three-body phase space and finding no candidate events, we can extract limits on the  $K^+ \rightarrow \pi^+\nu\bar{\nu}$  and  $K^+ \rightarrow \pi^+f$  branching ratios.

The surviving events are further characterized by occupation plots of the stopping counter (Figure 33a) and run number (Figure 33b), which demonstrate that the events are not localized in space or time, as might arise, for example, from a temporary detector or calibration problem. Figure 33c is a distribution of the kaon decay time, based on timing measurements in the range stack. Rough agreement with the accepted value for the lifetime verifies that the surviving events are due to kaon decays and that the acceptance is fairly uniform.

### 4.3 DESCRIPTION OF THE CUTS

In this section we describe the offline event reconstruction and the analysis cuts that are applied to the data. As with the trigger, the cuts we apply offline are largely motivated by the nature of the potential background events. Many of them were conceptualized before we knew exactly what the data looked like (inasmuch as they embodied the basic strategy of the experiment). Others did not arise until the data were inspected in detail.

For example, it was pretty clear beforehand that we would combine energy (ADC) and time (TDC) information to veto photons in coincidence with the charged track, and that we would use range and momentum information together to distinguish particles of different mass (*i.e.*, pion versus muon). But, other cuts were developed using the data itself as a guide. This was done by “hand-scanning” events that survived cuts already applied in order to expose a new class of “bad” events—events that are clearly discernible as background once more detector information is invoked.

<sup>†</sup> The  $K_{\pi 2}$  events that we reject represent a large sample of tagged  $\pi^0$  decays. Thus, our detection inefficiency allows us to set limits on the process  $\pi^0 \rightarrow \nu\bar{\nu}$  [27].

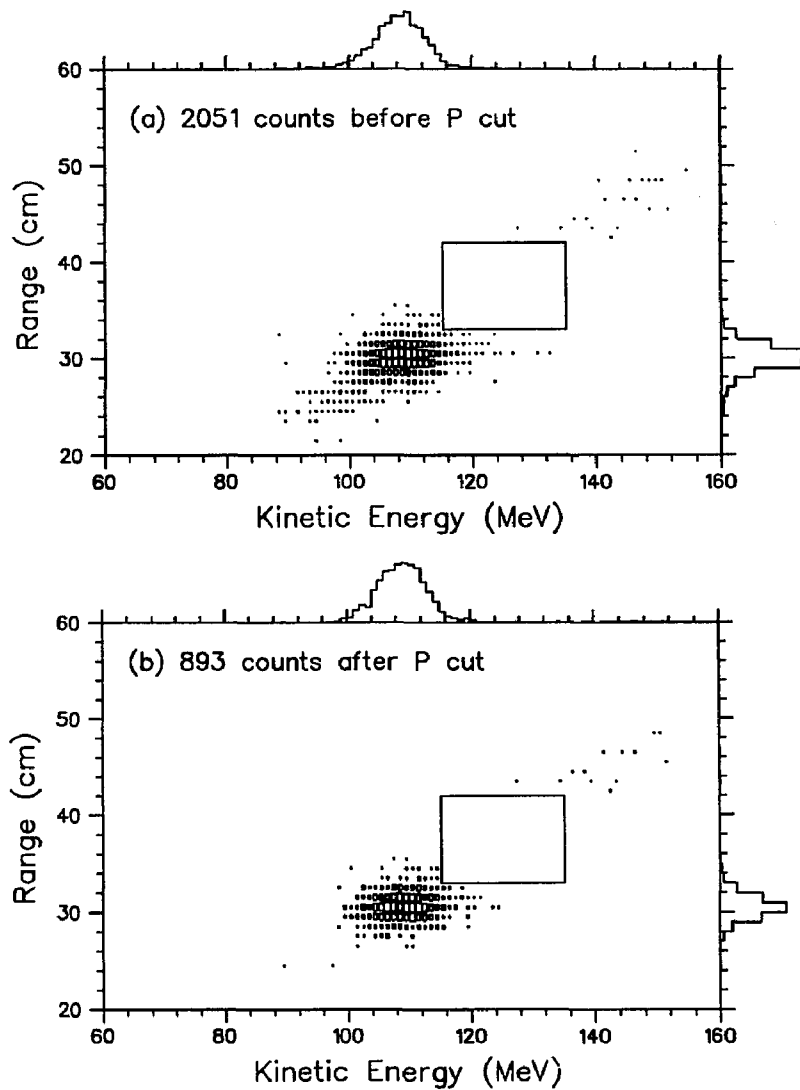


Figure 32. Range vs. energy for events surviving Pass 3, (a) before and (b) after a momentum cut of  $205 < P < 243$  MeV/c. The energy and range components of the kinematic "Box" cut are shown ( $115 < E < 135$  MeV;  $33 < R < 42$  cm). The cut positions are discussed in Section 4.3.6.2.

As the analysis unfolds it is imperative to carry out concurrent studies of the acceptance for the individual cuts. This is the only way to make sure that we are

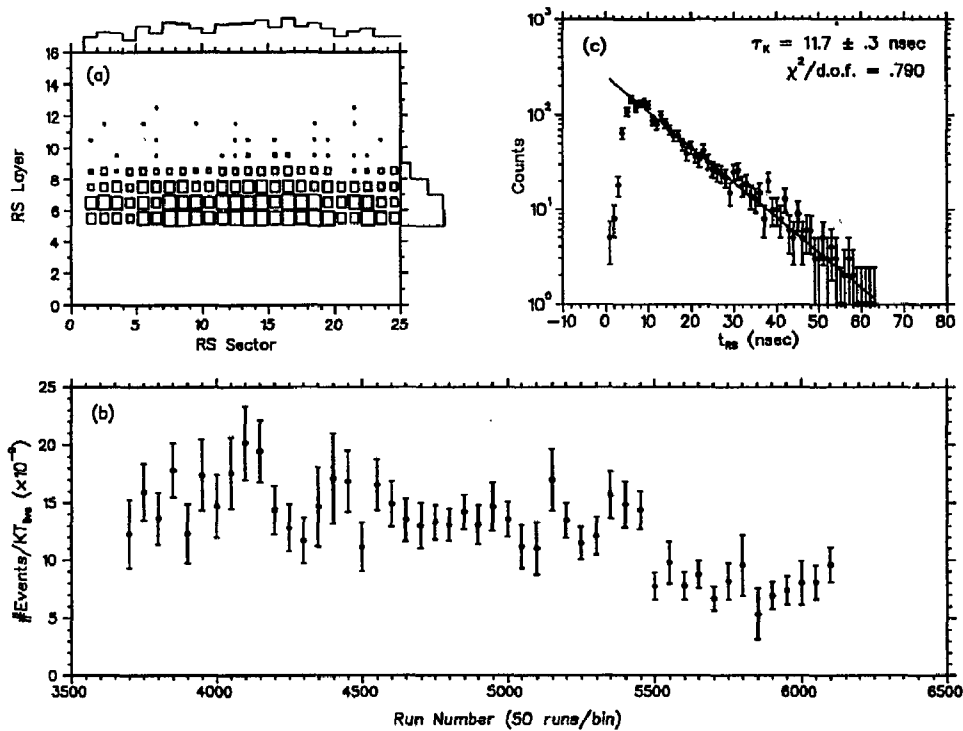


Figure 33. Events surviving Pass 3. (a) Occupation plot of the range stack stopping counter, in layer versus sector. (b) The number of events per unit kaon flux as a function of run number; the step near run 5500 is due to a loss of efficiency resulting from a broken wire in the central drift chamber (see Section 5.3.1). The data were taken in 1668 runs spanning the interval 3728–6148.  $KT_{\text{live}}$ , the unit of flux, is discussed in Section 5.7.1. (c) The kaon decay time as determined by the pion time in the range stack (true value:  $\tau_K = 12.4 \text{ nsec}$ ).

enhancing the signal to noise ratio.<sup>‡</sup> Of course, there is never perfect separation between signal and background, and it is often a judgement call to decide how hard to cut, how to balance rejection and acceptance. More straightforward is how to measure the acceptance of the cuts. This is done with various types of monitor triggers used to mimic different aspects of the signal. One example is the use of  $\pi$ -scat triggers to measure the acceptance of particle identification cuts, as was alluded to earlier. Another is the use of  $K_{\mu 2}$  triggers. These provide a source of

<sup>‡</sup> In the final analysis, we do not reject events via hand-scanning because the subjective nature of the technique makes it difficult to properly measure the acceptance.

clean single-track kaon decays with which to measure the accidental losses associated with photon vetoing.

A complete accounting of the acceptance is described in the next chapter. Now, we continue with the cuts themselves.

#### 4.3.1 Track Reconstruction

Reconstruction of the charged track is done in two steps. First, segments of the track are separately analyzed within the target, drift chamber and range stack; a loose set of cuts removes events that fail to reconstruct. Following this, properties of the track segments are tested alone and against each other, and further cuts are applied to reject events that are poorly reconstructed. All of the cuts have acceptance near unity for clean tracks; events that fail usually do so because they are obscured by an unrelated accidental track or a temporary detector problem. In what follows, I describe the analysis of the segments, the quantities that define them and last, the "quality" cuts.

##### 4.3.1.1 The Target Segment

The target analysis measures the properties of the decay particle from as close to the vertex as possible through to the I-counters. The time/energy pattern illustrated in Figure 13 is used to classify "triangles" as kaon or pion, thus defining the track in the target. The location of the pion triangle near the target periphery selects the I-counter associated with the track (the choice is later verified by the drift chamber). The triangle lists are used to extract quantities from the target as described below. Table 2 contains a summary.

The kaon and pion times are computed from the average time of the hits within their respective cluster. If the RMS deviation of the pion time is greater than 2 nsec then we use the I-counter instead to establish the time of the track in the target. Pion energy in the target and I-counter are summed from calibrated ADC values for the integrated pulse height in each element.

Range is computed using the coordinates of the triangle at the periphery of the target and the location of the kaon cluster, as illustrated in Figure 34. In order to best estimate how much of the true pion range is masked by the kaon, we start with the kaon and pion hit lists and further classify the triangles as being inside or outside a "road" defined by extrapolating the drift chamber track back into the target. The range is taken as the distance from the midpoint of the kaon cluster in the road to the periphery of the target, as shown. The event shown is an extreme

Target Information	
Variable	Description
$t_K^{tgt}$	Average time of kaon triangles
$t_\pi^{tgt}$	Average time of pion triangles, or IC
$E_\pi^{tgt}$	Summed energy of pion triangles
$E_\pi^{ic}$	Energy in I-counter
$P_{xy}^{tgt}$	$xy$ coordinate at target periphery
$R_\pi^{tgt}$	Pion range in target
$\Delta R_{tgt}$	Kaon-pion overlap
$R_\pi^{ic}$	Range in I-counter

Table 2. A summary of target information used in the analysis.

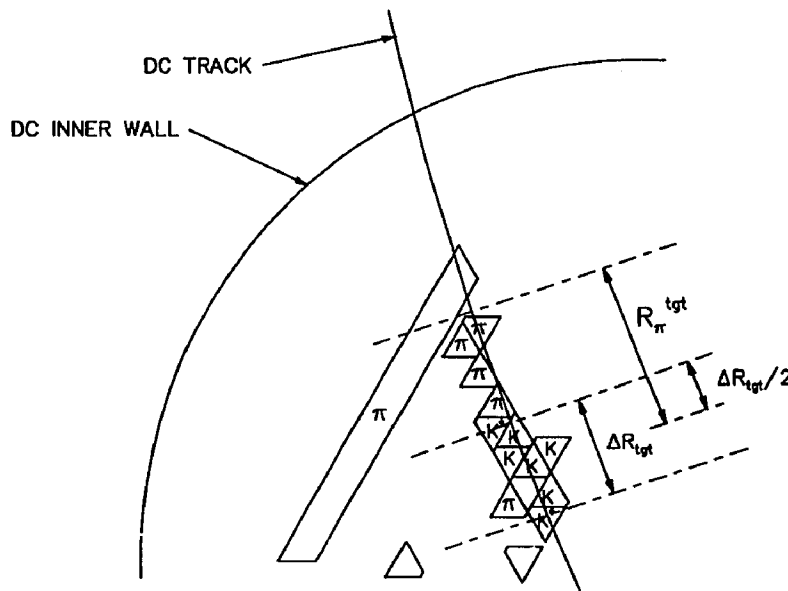


Figure 34. The target analysis.  $R_\pi^{tgt}$ , the target range, is the distance from the midpoint of the triangles at the extreme ends of the kaon cluster (marked K\*) to the periphery of the target.  $\Delta R_{tgt}$ , the separation of the starred (\*) K's, is a measure of the uncertainty introduced by kaon-pion overlap. The "road" (see text) consists of the area within about  $\pm 1.5$  triangles of the DC track.

case in that the kaon is very elongated in the  $x$ - $y$  plane. However, it serves to

illustrate the problem at hand—the uncertainty in range due to overlapping tracks. The uncertainty is minimized by using the road to define the biggest region of possible overlap.

The range in the I-counter is measured geometrically using the extrapolation of the drift chamber track. We approximate the hexagonal shell formed by the I-counters by a cylinder with similar dimensions. The direction cosines of the track at the radius of the cylinder (see next section) times the thickness of the counter determine the path length. Both target and I-counter ranges, which are measured in the  $x$ - $y$  plane, are corrected for the longitudinal component using the dip angle measurement of the drift chamber.

#### 4.3.1.2 The Drift Chamber Segment

The drift chamber analysis uses a circle fitting procedure to link together track segments in the axial super-layers 1, 3, and 5 to determine the transverse component of momentum. The longitudinal component comes from fitting a straight line to the stereo hits in super-layers 2 and 4. Corrections to the drift times are made to account for the Lorentz angle, timing variations in the stop signal, and signal propagation time along the wires. In addition to the momentum, other valuable information comes from the track fit in the form of position information, especially at the exit and entry points to the target and range stack: the center and radius of the fitted circle and the  $z$  information can be used to extract coordinate positions and direction cosines of the trajectory at specified detector radii. Table 3 summarizes the information derived from the tracking analysis.

DC Track Information	
Variable	Description
$P_{dc}$	Momentum in drift chamber
$Q_{\pi}$	Charge of the track
$\theta_{dip}$	Track angle relative to detector midplane ( $x = y = 0$ )
$x_r, y_r, z_r$	Track coordinates as a function of detector radius
$\cos \theta_i^{dc}(r)$	Direction cosines as a function of detector radius
$x_{cen}, y_{cen}$	Center of fit circle

Table 3. A summary of drift chamber information used in the analysis.

## 4.3.1.3 The Range Stack Segment

The range stack track is reconstructed to provide time, energy, and range measurements. It is defined by a list of contiguous counters starting with a  $T \cdot A$  combination that is selected by the azimuth of the drift chamber track. A track-finding algorithm loops over struck counters in the vicinity of the  $T \cdot A$  sector, working radially outward in the direction of curvature for positive particles. How we compute quantities of interest is described below; Table 4 contains a summary.

Linear interpolation of the rising edge of range stack TD pulses provides us with sub-nanosecond timing resolution. Because of the considerable length (2 m) of the counters the time it takes light to reach the two ends depends significantly on the  $z$  position of the production point. Therefore, the time in a given counter is best computed from the mean of the two ends, as this cancels the  $z$  dependence. Counter times are calibrated such that a charged particle emerging from the target and going into the range stack will register the same mean time in every counter it strikes. The overall time of the track is thus calculated by averaging the mean time in each counter.

Range Stack Information	
Variable	Description
$t_{\pi}^{rs}$	Average time of track counters
$E_{\pi}^{rs}$	Summed energy of track counters
$E_{last}^{rs}$	Track energy in stopping layer
$R_{\pi}^{rs}$	Path length of RS segment including S.L. correction
$z_i^{rs}$	RSPC $z$ position ( $i = 1, 2$ is the index over layers)
$L_{stop}^{rs}$	Layer index of stopping counter
$S_{stop}^{rs}$	Sector index of stopping counter

Table 4. A summary of range stack information used in the analysis.

Energy is handled in a similar fashion. However, here the  $z$  dependent effect is due to the *attenuation* of the light. Therefore, we take the *geometric* mean of the ends. The track's energy in the range stack is simply the sum of the counter energies.

The calculation of range is complicated by the presence of the magnetic field, which causes the tracks to curve and thus the entrance angle into each layer to vary. This is especially serious in the last layer if the particle is "turning over," as illustrated in Figure 26, and thus traveling along the length of the counter, rather

than through it. At the risk of inducing a correlation, we apply the energy-based correction described below.

The inputs to the range algorithm are the drift-chamber-derived entry vector complete with direction cosines, the range stack track list, position information from the range stack proportional chambers, and the energy in the last counter. The path length is computed geometrically using the available position/direction information from the chambers. Information from the counter list supplements the chamber positions, helps define the track boundaries, and allows for “gap corrections” to account for the path length in air and chamber material between the scintillators. Finally, we estimate the path length in the last layer using energy: a numerical integration of the *Bethe-Bloch* equation yields the path length corresponding to a stopping pion with initial energy  $E_{last}^{rs} - E_{\mu}$ , where  $E_{last}^{rs}$  is the energy in the last counter and  $E_{\mu}$  is the energy of the muon resulting from pion decay.

Additional quantities derived from the range stack analysis that enter elsewhere in the analysis are  $z$  positions from the RSPC’s used for fiducial cuts, and the address of the stopping counter used for TD cuts.

#### 4.3.1.4 Reconstruction Cuts

In the course of reconstruction we impose certain criteria that must be met in order to enable us to continue with the analysis of the event, that is, the event must be “setup” before complete analysis is possible. These requirements, which are implicit in the above three analyses, are summarized below. The losses are incurred at Passes 1 and 2.

- TG Setup  $\Rightarrow$  Clusters must be found for the kaon and pion. The pion cluster can be “constructed” from no triangles if the kaon is at the edge of the target. A pion time must be found, whether from the pion triangles or the I-counter. Preference is given to the triangles because of  $\sqrt{N}$  statistics.
- DC Setup  $\Rightarrow$  Must successfully find a track that satisfies  $P_{dc} < 270$  MeV/c and  $Q_{\pi} = +1$ . The above momentum cut is quite loose; it rejects only tracks that are well above the region of interest. (Recall that our final phase space cut places a momentum upper limit of 243 MeV/c.)
- RS Setup  $\Rightarrow$  Must successfully reconstruct one, and only one, track. Must find track time.

Additional cuts are applied to ensure the quality of the individual track segments, and of the overall track:

- $D_{tgt}, D'_{tgt} \Rightarrow$  Compare the  $xy$  position of the drift chamber track at the outer edge of the target with that determined by the target itself. Apply a loose cut at Pass 1, limiting the discrepancy to 6 cm (the perimeter of the target hexagon is 36 cm). Tighten the cut at Pass 3 to 3 cm.
- $\Delta t_{\pi} \Rightarrow$  Compare the pion time in the target and range stack. Require  $|t_{\pi}^{rs} - t_{\pi}^{tgt}| < 5$  nsec. In terms of timing resolution, this is a modest cut; mainly it serves to reject events where a gross error has occurred, such as an accidental hit disrupting a time-reference signal and completely throwing off the time of one of the segments.
- $TG_{gap} \Rightarrow$  Make sure that the pion track originates near the kaon by looping over all combinations to find the minimum pion-kaon separation in the  $x-y$  plane. Require it to be less than 1 cm.
- $\Delta R_{tgt} \Rightarrow$  Place an upper limit on the kaon-pion overlap by requiring  $\Delta R_{tgt} < 1.8$  cm. (This was defined in Figure 34.)
- $R_{IC} \Rightarrow$  Require  $R_{\pi}^{ic} < 5$  cm. Tracks that leave from the edge of the target at a very shallow angle can have a significant path length in the I-counters, which are only .64 cm thick. For such tracks, our measurement is very sensitive to small errors in the drift chamber direction-cosines (see Section 4.3.1.1, above). Therefore, we reject events with a long I-counter range.
- $z_{tgt} \Rightarrow$  This cut eliminates reconstruction mishaps due to tracks that emerge from the degrader and stop in the fiducial region. Such events can satisfy the trigger if they occur close in time to some other particle that has fulfilled the trigger's beam requirements. These events are characterized by a  $z$  value upstream of the front face of the target. To suppress these events we require  $z_{tgt} > -15$  cm, where  $z_{tgt}$  is the  $z$  position of the track as it leaves the target. (The target starts at  $z = -12$  cm.)

#### 4.3.2 Fiducial Volume Cuts

Fiducial cuts beyond those implied in the trigger and offline reconstruction more carefully define the region of the detector in which reliable kinematic measurements can be made—momentum, range, and energy are all affected. At large dip angles the momentum resolution worsens because the longitudinal correction becomes increasingly significant and begins to dominate the resolution. Range, which is similarly affected by a longitudinal correction, is also aggravated by a larger last-layer correction due to the “turn over” effect discussed earlier.

The energy of a track can be degraded since tracks can just as easily turn over in the non-scintillating materials that make up the range stack chambers. In tracks

that *appear* to stop in range stack layer 14 (just before the outer chamber), the effect is particularly noticeable because the particles are highly ionizing. It is likely that the tracks have actually stopped in or grazed the chamber wall, an hypothesis that is borne out by Monte Carlo simulation. The volume cuts, which are based on drift chamber and range stack position measurements, are summarized in Table 5.

Fiducial Cuts		
Pass	Symbol	Requirement
Pass 2	$\theta_D$	$-33^\circ < \theta_{\text{dip}} < 33^\circ$
Pass 3	$\theta_D^n$	$-30^\circ < \theta_{\text{dip}} < 30^\circ$
Pass 2	$z_{14}$	for $L_{\text{stop}}^{\text{rs}} = 8$ , $-36. < z_1^{\text{rs}} < 36.$ cm for $L_{\text{stop}}^{\text{rs}} = 8$ , no hits in outer chamber for $L_{\text{stop}}^{\text{rs}} \geq 8$ , $-40. < z_1^{\text{rs}} < 40.$ cm
Pass 3	$z'_{14}$	for $L_{\text{stop}}^{\text{rs}} = 8$ , $-36. < (z_1^{\text{rs}} - z_{\text{tgt}}) < 36.$ cm

Table 5. Summary of the fiducial cuts. The superscript in  $z^{\text{rs}}$  refers to the inner chamber.

#### 4.3.3 The Delayed Coincidence Cut

A comprehensive delayed coincidence cut is made with calibrated timing information in the target and range stack. The cut is applied in four parts, the first of which accounts for most of the rejection. The requirements are as follows:

- $t_\pi^{\text{tgt}} - t_K^{\text{tgt}} > 2.$  ns, if  $t_\pi^{\text{tgt}}$  is from target triangles.
- $t_\pi^{\text{tgt}} - t_K^{\text{tgt}} > 4.$  ns, if  $t_\pi^{\text{tgt}}$  is from the I-counter — we increase the delay because the I-counter time resolution is not as good.
- $t_K^{\text{tgt}} < 3.$  ns — late kaons indicate a faulty TDC stop signal or other spurious activity.
- $t_\pi^{\text{rs}} > t_K^{\text{tgt}}$  — provides a redundant measurement of the delay time.

#### 4.3.4 The Transient Digitizer Cuts

Particle identification cuts are made using transient digitizer (TD) data in and near the stopping counter to tag stopped pions by looking for the  $\pi^+ \rightarrow \mu^+ \rightarrow e^+$  decay signature. The two stages of the decay sequence are treated separately. The

$\pi^+ \rightarrow \mu^+$  tagging is done primarily with an algorithm called FITPI, which applies a fitting procedure to the pulse shape data in the stopping counter to determine the number of pulses and properties thereof. If two pulses are found, the event is subjected to cuts that test the integrity of the second pulse, as well as exploiting the characteristics of the decay muon. The  $\mu^+ \rightarrow e^+$  tagging uses the area and leading edge times of pulses in the vicinity of the stopping counter to look for energy clusters from the decay electron. The following two sections describe the analysis of the TD data and the associated cuts.

#### 4.3.4.1 The $\pi^+ \rightarrow \mu^+$ Tagging

Transient digitizer data for the two ends of the last counter in the range stack track are fitted to hypotheses for a stopping muon and a stopping pion. It turns out that individual phototube pulses can be characterized by just two quantities, their leading-edge time and their total area. In other words, the pulse *shape* is basically the same from pulse to pulse. Therefore, we can test the muon hypothesis with a two-parameter fit in which the pulse area and leading-edge time of a single "template" pulse are varied with respect to the data. Similarly, the pion hypothesis is tested with two template pulses in a four-parameter fit in which we vary the area of each pulse, the time of the first pulse, and the relative separation of the two pulses. Figure 35 illustrates the fitted results for both ends of the stopping counter of a  $K_{\pi 2}$  event. The event was selected by measuring the kinematics of the charged track and checking for two photons. Notice that the muon hypothesis is a poor fit to the data, while the pion hypothesis fits the data well.

Summary of FITPI Variables	
Variable	Description
$C_j^i$	Quality of fit for end $i = 1, 2$ ; species $j = \pi, \mu$
PROD	Combined fit quality: $\frac{C_\mu^1}{C_\pi^1} \cdot \frac{C_\mu^2}{C_\pi^2}$
$t_\mu^i$	Pulse separation at end $i$
$t_\mu^{\text{av}}$	Average muon time: $(t_\mu^1 + t_\mu^2)/2$
$E_\mu^i$	Area of second pulse at end $i$
$E_\mu^{\text{av}}$	Average muon energy: $\sqrt{E_\mu^1 E_\mu^2}$

Table 6. A summary of the quantities measured by fitting TD pulses. These form the basis of the cuts described in this section. The last four entries are only defined for the two-pulse fit.

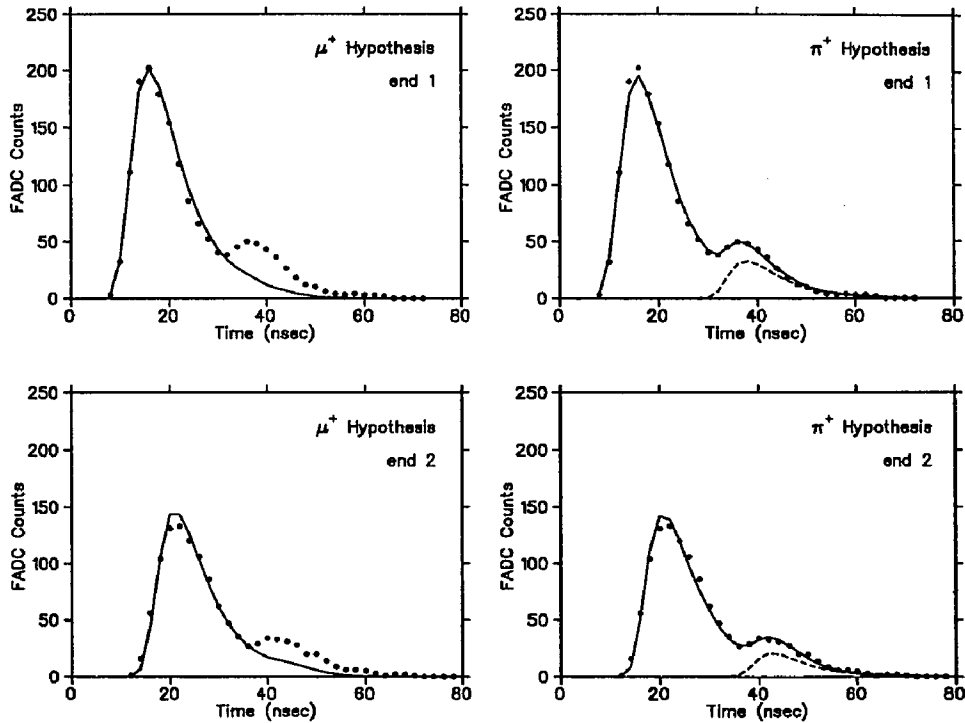


Figure 35. The results of fitting single- and double-pulse hypotheses to the pulse shape data in a  $K\pi_2$  event for the two ends of the stopping counter. The points indicate the actual data, the solid curve is the results of the fit, and for the double-pulse plots on the right, the dashed curve represents the second pulse, alone.

The quality of the fit is quantified by chi-squared-like variables,  $C_j^i$ , where  $i = 1, 2$  for the two ends and  $j = \pi, \mu$  for the two species. Since the deviations that contribute to the  $C_j^i$ 's are not really statistical, but are correlated with the pulse shapes, it would be misleading to name it  $\chi^2$ . Nonetheless, the trend of large values for poor fits still holds and is useful for making particle identification cuts in a consistent, quantitative fashion. Additional quantities, summarized in Table 6, derive from the fitted pulses. In particular, they well-characterize the second pulse as exemplified by a measurement of the pion lifetime shown in Figure 36.

Table 7 summarizes the TD cuts applied in the first two passes through the data. Several considerations go into their definition and tuning. The PREFIT cuts ensure that the muon hypothesis is a *poor* description of the data. Since only the one-pulse fit is performed and it takes considerably less CPU time to execute than the two-pulse fit, we realize a convenient savings in the overall processing time by

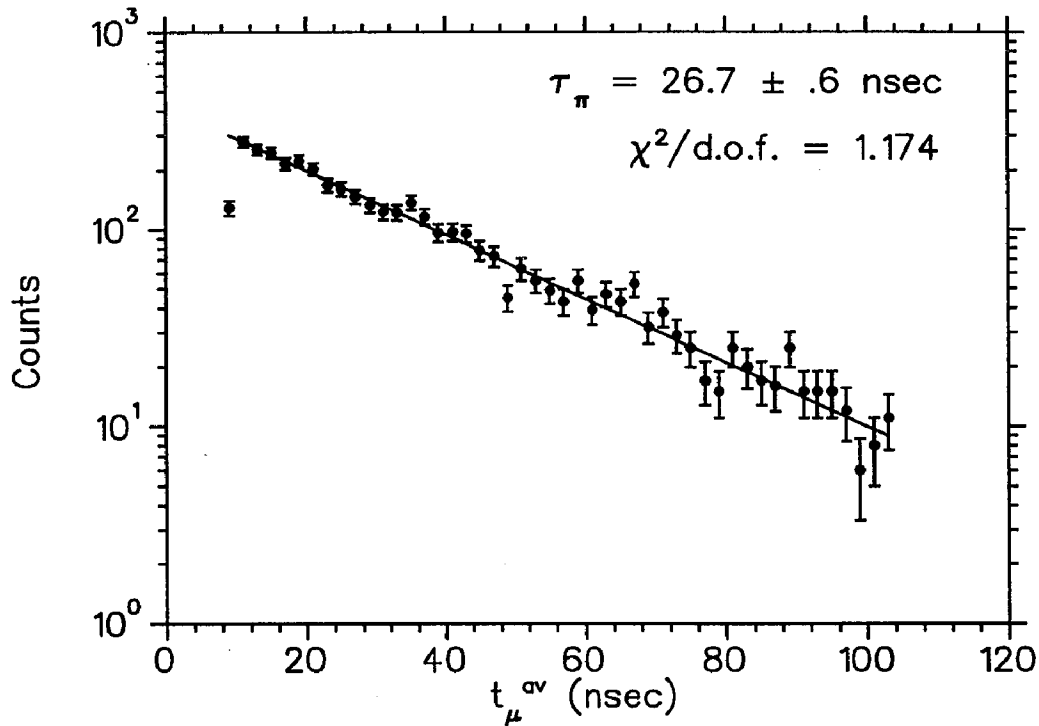


Figure 36. The time of the second pulse provides a measurement of the pion decay time. The events are  $\pi$ -scat triggers that have satisfied the “range-momentum” particle identification cut defined in Section 4.3.6, and the FITPI and FITPI2 cuts defined in this section. The fit value comes out slightly higher than the accepted value of 26.0 nsec.

applying the two-pulse analysis only to events that have passed the one-pulse cuts. Since the one-pulse analysis executes even faster than than the track reconstruction algorithms, it is the first offline analysis performed on the data. As a result, we do not yet know the values of  $L_{stop}^{rs}$  and  $S_{stop}^{rs}$ , so we use the hardware-determined stopping counter from the trigger, as with TDPION. After the application of some non-TD cuts we then go ahead with the more time-consuming two-pulse fit, which allows for cuts on both the pion and muon fit quality, as well as on the characteristics of the second pulse.

The FITPI cuts include limits on both the single-ended and average muon times to ensure that the two pulses are well separated—with its extra degrees of freedom, it is not unlikely that the fitting algorithm finds a high-quality two-pulse fit for what is truly a one-pulse event. An end-to-end timing cut requires that the same

Pass 1 and Pass 2 TD Cuts	
Quantity	Requirement
PREFIT Cuts	
Single-end single-pulse fit quality	$C_\mu^i > 0., i = 1, 2$
Double-end single-pulse fit quality	$\log_{10} \sqrt{C_\mu^1 C_\mu^2} > 1.8$
FITPI Cuts	
Single-end fit quality	$\frac{C_\mu^i}{C_\pi^i} > 1.5, i = 1, 2$
Combined fit quality	PROD > 3.
Single-end muon time	$2. < t_\mu^i < 120. \text{ ns}, i = 1, 2$
End-to-end muon timing	$-5 < (t_\mu^2 - t_\mu^1) < 5 \text{ ns}$
Average muon time	$2. < t_\mu^{\text{av}} < 120. \text{ ns}$
Single-end muon pulse height	$60. < E_\mu^i < 360. \text{ counts}, i = 1, 2$
Average muon pulse height	$70. < E_\mu^{\text{av}} < 270. \text{ counts}$
FITPI2 Cuts	
Average muon time	$t_\mu^{\text{av}} > 9. \text{ ns}$
Single-end muon pulse height	$E_\mu^i > 90. \text{ counts}, i = 1, 2$
Average muon pulse height	$100. < E_\mu^{\text{av}} < 240., \text{ for } t_\mu^{\text{av}} < 12. \text{ ns}$
End-to-end muon timing	$-3.25 < (t_\mu^2 - t_\mu^1) < 3.25 \text{ ns}$

Table 7. Summary of the cuts that are applied at Pass 1 (PREFIT and FITPI) and Pass 2 (FITPI2). The pulse-height calibration of the TD's is 56 counts/MeV.

pion decay time is measured at each end, or equivalently, that the  $z$  position of the muon agree with that of the pion.

Loose cuts at Pass 1 restrict the fitted muon energy as shown in the summary table. These reject single-pulse events that have large pulse height in the stopping counter and as a result are susceptible to fluctuations that lead to a pion signature with large apparent muon energy. Restricting the muon energy to a narrow band also makes sense because the muon from pion decay at rest is mono-energetic (4.2 MeV). The cut helps suppress a potential background induced by early  $\mu^+ \rightarrow e^+$  decays of stopped  $K_{\mu 2}$  muons that otherwise fake the  $\pi^+ \rightarrow \mu^+$  signature: since the electron is relatively energetic over most of its phase space, it tends to leaves a large signal in the stopping counter. Events with fake second pulses due to large accidental hits are rejected as well. We plot the relevant quantity,  $E_\mu^{\text{av}}$ , for a sample of selected  $\pi$ -scat triggers in Figure 37.

A final set of requirements called FITPI3 conclude the cuts based on the fitted

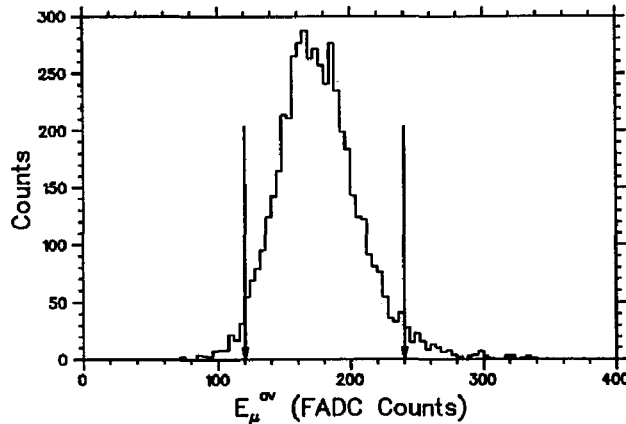


Figure 37. The average muon energy is plotted for kinematically selected  $\pi$ -scat triggers prior to any secondary TD cuts. The Pass 3 cut is indicated by the arrows.

quantities. Also included in this group are some cuts that do not rely on the fitted information but for organizational reasons fall naturally into this category, *i.e.*, cuts that deal with the activity in the stopping region. The cuts are summarized in Table 8; the less obvious ones are described below.

- TPIDIF  $\Rightarrow$  Suppress  $K_{\mu 2}$  events that have extra *early* activity in the stopping counter. An early pulse can conspire with the stopping pulse to fool the fitting algorithm. Such events are rejected by calibrating the time of the first fit pulse and requiring agreement with the measured time in the stopping counter.
- LOELAST  $\Rightarrow$  Require that the energy in the stopping counter be greater than 4 MeV.
- TDFLUC  $\Rightarrow$  Suppress tail fluctuations of stopping muon pulses, many of which are characterized by both high pulse height in the stopping counter and early (apparent) decay time. That these quantities are correlated for muons is shown in Figure 38. The numbers used in the cut describe the equation of the line shown in the figure.
- RSHEX  $\Rightarrow$  Reject events in which the second pulse occurs in the stopping hexant but not in the stopping counter (recall that the TD's record sums of four). Flag bits can potentially resolve the problem. However, similar information exists in the ADC's as well and that is where it turns out to be easiest to implement the necessary logic. Therefore, we reject events when there is ADC energy above .5 MeV in the stopping hexant that is not part of the range stack track. Figure 39 shows both the TD and ADC data for an event that fails the cut.

FITPI3 Cuts	
Name	Description/ Requirement
TPIDIF	First pulse of fit agrees with track time: $-15 < (t_{\pi}^{\text{fit}} - t_{\pi}^{\text{rs}}) < 15$
LOELAST	Minimum energy in stopping counter: $E_{\text{stop}}^{(\text{ADC})} > 4. \text{ MeV}$
EMUAV	Restrict fitted muon energy for all $t_{\mu}^{\text{av}}$ : $120. < E_{\mu}^{\text{av}} < 240. \text{ counts}$
TDFLUC	Tail fluctuations correlate with high $E_{\text{last}}^{\text{rs}}$ : $(1.364 \times t_{\mu}^{\text{av}} + 5.909) < E_{\text{last}}^{\text{rs}}$
PROD20	Minimum fit quality: $\text{PROD} > 20.$
TMUPROD	Poor fit quality correlates with early muon time: $\text{PROD} > 50., \text{ for } t_{\mu}^{\text{av}} < 26. \text{ nsec}$
RSHEX	Muon not in stopping counter (based on ADC's): <i>see text</i>

Table 8. Summary of the cuts that comprise the FITPI3 requirement.

As the above discussion of the last cut illustrates, activity at the apparent pion decay time that occurs outside the stopping counter can expose spurious events. Two more algorithms expand the search for such activity. The first, ELVETO, uses leading edge times of TD pulses throughout the range stack to search for hits that are in time coincidence with  $t_{\text{elv}} = t_{\pi}^{\text{rs}} + t_{\mu}^{\text{av}}$ . As the name suggests, one source of the extra hits are electrons from early decays of stopped  $K_{\mu 2}$  muons.

These electrons are in the energy regime where they can radiate soft photons that shower elsewhere in the detector. If they also happen to be responsible for the second pulse in the stopping counter then the extra hits will appear at  $t_{\text{elv}}$  and the event can be vetoed. The ELVETO cuts are broken up into two parts: ELVETO at Pass 2 vetoes on extra activity within  $\pm 1$  sector of the stopping counter, and ELVETO2 at Pass 3 expands the veto to the rest of the range stack.

The second algorithm, TDFOOLERY, is named for a similar class of events that also cause the FITPI analysis to be "fooled." Again, electrons are the cause: if they travel back along the path of the muon, then their leading edge times will be obscured. Consequently, ELVETO will fail to reject them. Since this is the now familiar problem of distinguishing two pulses close in time with one another we simply apply the FITPI analysis to these counters, the inner layers of the track. If

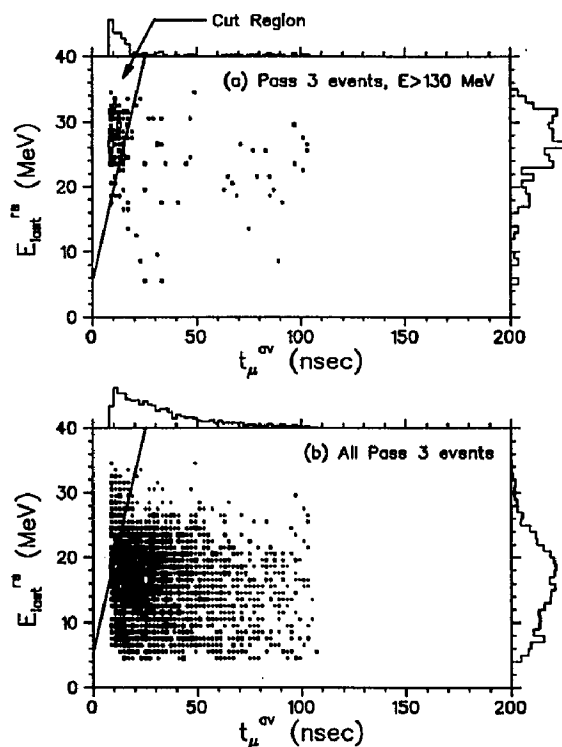


Figure 38.  $E_{last}^{rs}$  vs.  $t_{\mu}^{sv}$  is plotted for the Pass 3 sample just prior to application of the TDFLUC cut, which is indicated by the solid line. For the purpose of illustrating the correlation of these two quantities for muons we make two plots: (a) consists of events with total track energy above 130 MeV (the muons in the sample); (b) consists of the full sample, which is dominated by pions from  $K_{\pi 2}$  events, those with undetected photons.

second pulses are found with the same separation as in the stopping counter then TDFOOLERY rejects the event. It is important to note that the 4.2 MeV muon from  $\pi^+ \rightarrow \mu^+$  decays has a range of just 1.5 mm; only 4% of the time does it deposit a detectable amount of energy outside the 2 cm thick counter in which the pion stops (this is estimated in Section 5.4.2.1).

#### 4.3.4.2 The $\mu^+ \rightarrow e^+$ Tagger

As discussed earlier, we require the second part of the pion decay sequence to reduce the chances that it was a  $\mu^+ \rightarrow e^+$  decay that passed the  $\pi^+ \rightarrow \mu^+$  cuts. The strategy here is different from  $\pi^+ \rightarrow \mu^+$  tagging because (i) over most of the phase

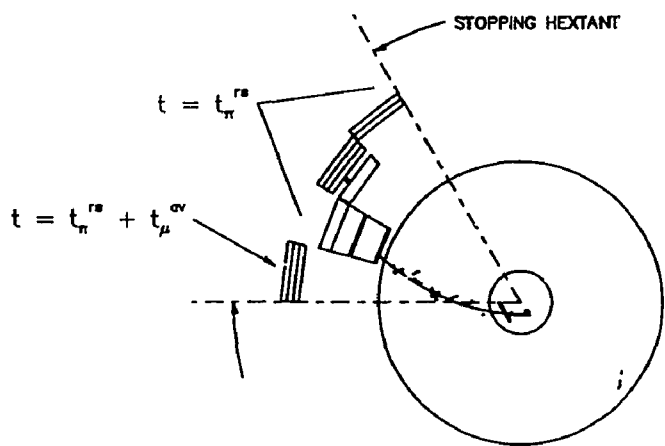
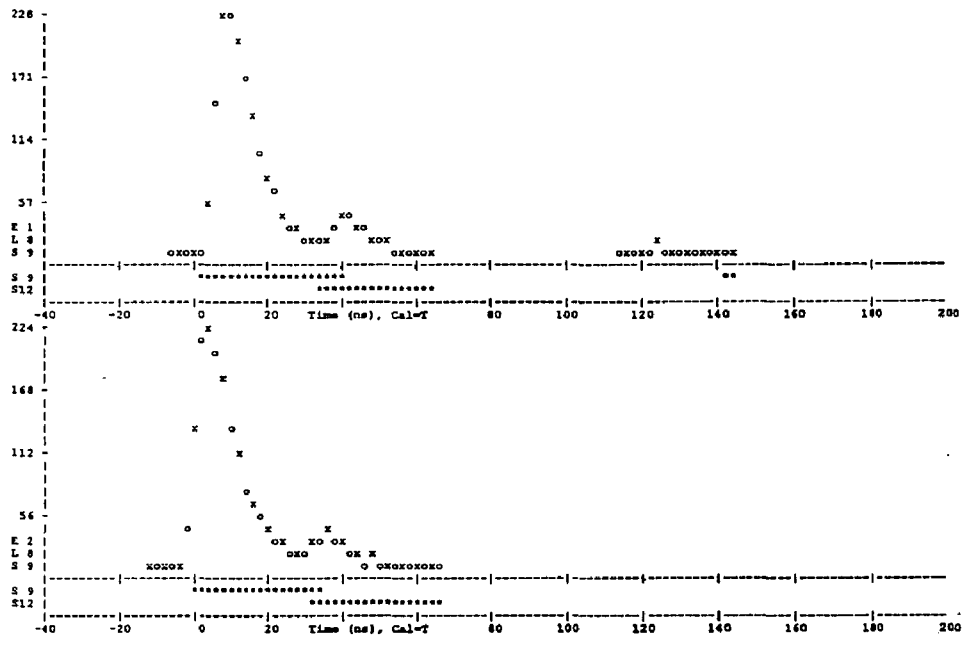


Figure 39. An event rejected by the RSHEX cut. The TD data for the (a) upstream and (b) downstream ends of the stopping counter show the pulse height as a function of time, along with the active flag bits in each sector. The ADC-based event display (c) corroborates the TD flag information—notice the detached cluster in the stopping layer that occurs at the time of the apparent  $\pi^+ \rightarrow \mu^+$  decay.

space the decay electron is more energetic than the decay muon, so we can demand that it strike more than one counter and (ii) the muon lifetime is long compared to TD pulse widths, so fitting techniques are not needed—individual pulses are well characterized by simply their leading edge time. Both of these points are illustrated in Figure 40 which shows the full decay sequence in four layers of range stack TD data for a  $K_{\pi 2}$  event. The event selected has a relatively late pion decay and a relatively early muon decay so that the pulse times and widths can be viewed on the same horizontal scale—the TD's actually record muon decays as late as  $6 \mu\text{sec}$ , or nearly  $2.7 \mu^+$  lifetimes.

The  $\mu^+ \rightarrow e^+$  algorithm starts with the location of the stopping counter and the time of the pion decay and uses them to define regions in space and time in which to search for electron hits. It uses end-to-end mean times in a three-by-five block of range stack counters (shown in Figure 41) to look for time coincidences among the counters. Cuts on the end-to-end time difference ensure that hits within a cluster come from the same  $z$ -position, and that the average  $z$  of the cluster agrees with that of the pion; the 3.5 nsec coincidence window corresponds to about 25 cm in  $z$ , or one-eighth the length of the counters.

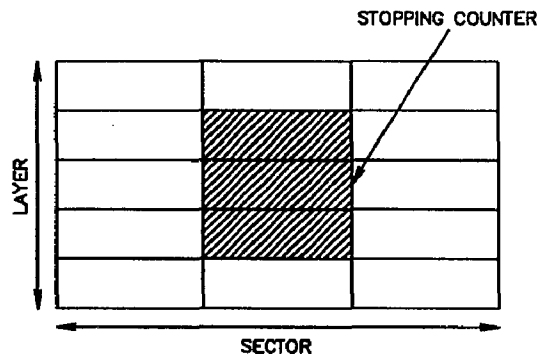


Figure 41. A schematic view the  $\mu^+ \rightarrow e^+$  search region in the range stack "local" to the stopping counter. A minimum of 2 hits is required in the  $3 \times 5$  block of counters, at least one of which must be in the shaded area.

Pulse height cuts serve two purposes. On the low side they filter out small noise hits in the vicinity of the stopping counter, while on the high side they reject electron candidates that have energy well above the endpoint energy. Accidental tracks that land in the stopping region are usually responsible for clusters above the endpoint. Parameters for the timing and pulse height cuts are summarized in Table 9.

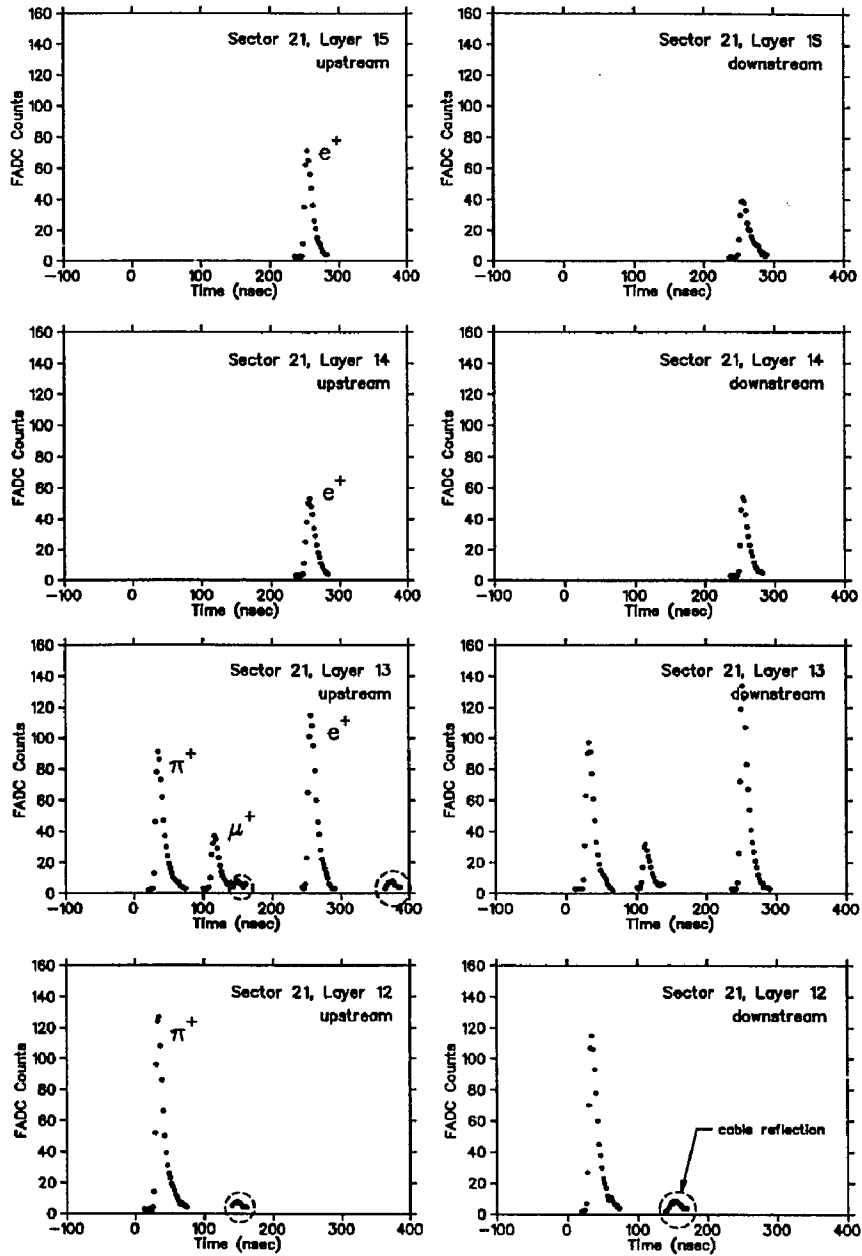


Figure 40. Actual TD data showing the full stop and decay sequence for a  $K_{\pi 2}$  event in the range stack. The  $\pi^+$  passes through layer 12, stops in layer 13, and decays to a muon. The muon, which is contained by the stopping counter, decays in turn to an electron. The small encircled pulses caused by cable reflections are not problematic since they are below the threshold for primary pulses.

$\mu^+ \rightarrow e^+$ Parameters	
Description	Value
Minimum delay time to accept hits after $t_\mu^{\text{av}}$	20 nsec
Coincidence window for end-to-end hits	20 nsec
Coincidence window for counter-to-counter hits	5 nsec
Coincidence window for end-to-end match ( $z_\pi$ vs. $z_e$ )	3.5 nsec
Pulse height threshold for hits (sum of two ends)	100 TD cts.
Lower limit on local integrated pulse height	750 TD cts.
Upper limit on total integrated pulse height (full RS)	7000 TD cts.

Table 9. Parameters used in  $\mu^+ \rightarrow e^+$  tagging. Hits for the total RS pulse height sum at the  $\mu^+ \rightarrow e^+$  decay time are subject to the same time coincidence windows as the local electron hits.

Figure 42 shows a fit to the muon lifetime based on the time of the electron. The measured value of  $2190 \pm 65$  nsec is in good agreement with the accepted value of 2197 nsec. A further test of the purity of the tagged electrons is made by a background study in which we search the *opposite* side of the detector for an electron. We find the rate of accidentals is less than 2%, compared with a tagging efficiency of 85% for real  $\mu^+ \rightarrow e^+$  decays (details of the efficiency measurement are given in Chapter 5).

#### 4.3.5 Photon Veto Cuts

The offline vetoes employ every scintillating element of the detector (beam counters excepted) in order to detect photons with very high efficiency. Photon energy comes in two broad categories: showers in regions that are spatially separate from the charged track, or showers that partially or fully overlap it. Photons in the latter category are more subtle to detect; fortunately, most are in the former.

The use of timing information is crucial in tagging photon energy because of the susceptibility of vetoing otherwise clean single-track events due to accidental hits. Rates in the detector (typically 10–100kHz) are such that during the 100 nsec integration time of the ADC's, it is almost certain that at least one of the 1000 or so channels, unrelated to the track, will have energy above threshold. Since this would result in utterly unacceptable losses, we examine the veto energy more carefully, so as to only include that which is "in time" with the charged track. The one place this is difficult to accomplish is when there is complete overlap of the photon by the charged track, but again, this is a relatively small region of "phase space."

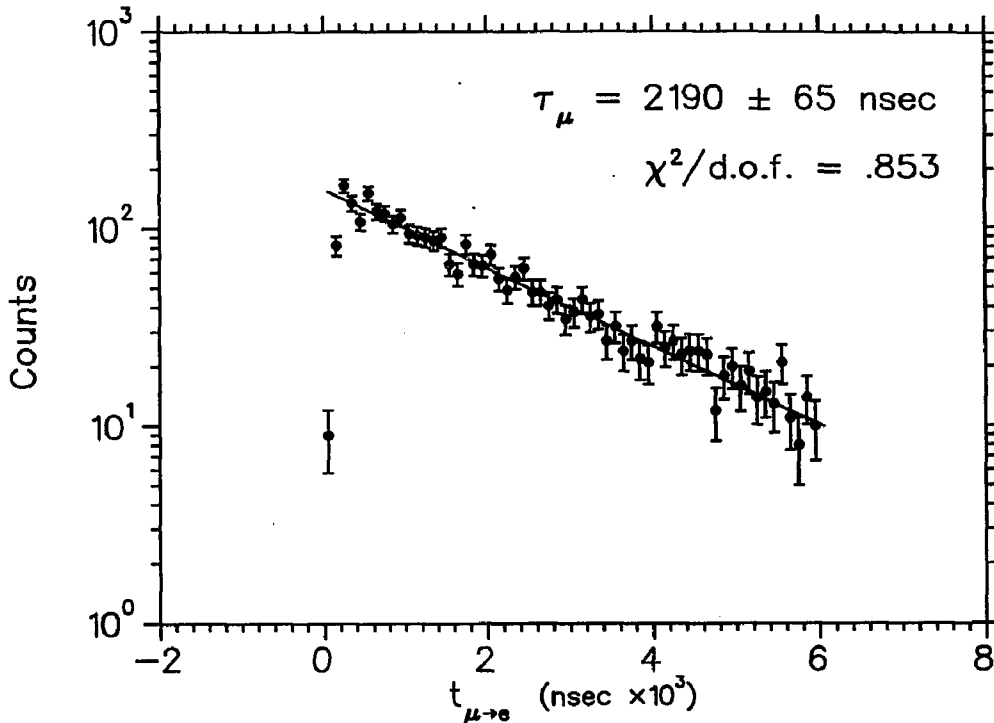


Figure 42. The time of the electron is plotted for a sample of  $\pi$ -scat triggers that have satisfied the range-momentum, FITPI and FITPI2 pion identification cuts. The solid line is an exponential fit from 300 to 6100 nsec.

Veto energy is accumulated in a number of ways, and used for the cuts summarized in Table 10. Energy that is separate from the track is treated by two algorithms—one for the target and one for the rest of the detector. In the target, we sum energy that is in time with the  $\pi^+$  but outside of the projected road of the drift chamber (the same road that was discussed in relation to Figure 34). Hits within 6 nsec of the pion are considered to be in time; to avoid accidentally vetoing on kaon energy they must also be later than  $t_K^{\text{tgt}}$ . The sum,  $E_{\text{veto}}^{\text{tgt}}$ , and the number of hits,  $N_{\text{veto}}^{\text{tgt}}$ , are used for the  $\bar{\gamma}_{\text{tgt}}$  cut, as shown in the table.

“Prompt” energy in each of the remaining sub-systems, which is defined by narrow time windows centered about  $t_{\pi}^{\text{rs}}$ , is accumulated by a routine called INTIME. Events are rejected if the sum of the prompt energy,  $E_{\text{veto}}^{\text{pr}}$ , is greater than 1 MeV. The features of INTIME, which are designed to minimize the amount of accidental vetoing, are as follows:

- Energy is summed throughout the barrel, endcap, and range stack, and in the I- and V-counters. Range stack counters from the track list and the track I-counter are excluded from the sum.
- Only ADC hits with associated time information are included. (The absence of TDC or TD information is accounted for by small differences in the thresholds of the various systems and a low-level of instrumentation failures.
- In the range stack and barrel, only counters that are struck at both ends are used. This affords the best time resolution, and hence the narrowest windows, because mean times are available.
- The time resolution in the range stack is sufficiently good that we are sensitive to the different velocity of photons and charged particles. Therefore, a correction is applied to the photon time based on the layer of the shower [28].
- To reduce accidental losses in the endcaps, only hits greater than 2 MeV are added to the sum. (The veto threshold on the sum is 1 MeV.)

Because of the differences in geometry and instrumentation, separate windows are determined for each sub-system. As usual, we begin with a narrower set of windows and then widen them at a later pass, as summarized in Table 10 (the  $\overline{\gamma_n}$  and  $\overline{\gamma_w}$  cuts).

Additional cuts are needed in the target and range stack to suppress events with photons on or near the track because these are missed by the above methods. The  $\gamma'_{tgt}$  cut consists of three cuts that look for abnormally large energy depositions by defining what is expected for a track with no photons. The first compares  $E'_{tgt}$  and  $R_{\pi}^{tgt}$  as shown in Table 10, where  $E'_{tgt}$  equals  $E_{\pi}^{tgt}$  plus any residual hits in the "road" that are not already accounted for. If a photon has showered on the track then the energy comes out high for the measured range. The second cut checks all pion fibers in the target list and requires that none be over 5 MeV. The third requires that  $E_{\pi}^{tc}$ , the I-counter energy, be less than 4 MeV.

Showers in the range stack that land near the track are rejected by a pattern cut called PRPAT that looks for prompt energy in counters contiguous to the track, such as those illustrated in Figure 43. The events with photons are characterized by tracks that appear to have crossed sector boundaries at more than one layer. Clean single-track events cannot lead to this topology.

The BETASQ cut rejects events in which a photon showers on the inner layers of the range stack track and thus causes an abnormally large energy, there. According to the *Bethe-Bloch* equation the energy loss is given approximately by

$$\frac{dE}{dx} \sim \frac{1}{\beta^2}.$$

Photon Veto Cuts		
Pass	Cut	Requirement
Pass 2	$\overline{\gamma}_n$	INTIME: $E_{veto}^{pr} < 1$ MeV $t_{rs} = 1.2, t_{bv} = 3.0, t_{ec} = 4.0, t_{ic} = 2.5$ nsec
Pass 3	$\overline{\gamma}_w$	INTIME: $E_{veto}^{pr} < 1$ MeV $t_{rs} = 2.4, t_{bv} = 6.0, t_{ec} = 6.0, t_{ic} = 5.0, t_{vc} = 5.0$ nsec
Pass 2	$\overline{\gamma}_{tgt}$	$E_{veto}^{tgt} < 2$ MeV, for $N_{veto}^{tgt} \geq 2$ $E_{veto}^{tgt} < 5$ MeV, for $N_{veto}^{tgt} = 1$
Pass 3	$\overline{\gamma}'_{tgt}$	$E'_{tgt} < 5 \times R_{\pi}^{tgt}$ , for $R_{\pi}^{tgt} < 5$ cm $E'_{tgt} < 2 \times R_{\pi}^{tgt} + 15$ , for $R_{\pi}^{tgt} \geq 5$ cm $E_{\pi}^{ic} < 4$ MeV $E_{\pi\Delta}^{tgt} < 5$ MeV for all $\Delta$ 's in pion list
Pass 3	PRPAT	<i>see text</i>
Pass 3	BETASQ	$E_{abc} \times \beta^2 < 37$ MeV, if $E_{\pi}^{rs} - E_{abc} > 10$ MeV

Table 10. Photon veto cuts. The time given for each sub-system in the INTIME cuts is the half-width of the window that defines "prompt." V-counter energy was not included in  $E_{veto}^{pr}$  until Pass 3.

If we assume a constant range in the first three layers of the track then the relevant quantity to compute is  $E_{abc} \times \beta^2$ , where  $E_{abc}$  is the summed energy in layers A-C, and  $\beta^2$  is taken from the average kinetic energy in those layers, assuming a pion mass. If this comes out too large then we take it as evidence of a photon.

The placement of the cut at 37 MeV is determined empirically by measuring this quantity for a sample of  $\pi$ -scat events that have been selected with kinematic and TD particle identification cuts and that have passed the other photon veto cuts. Figure 44 shows both the spectrum and the cut position. Since the determination of  $\beta^2$  turns out to be reliable only if the pion still has significant energy upon leaving the layer C we apply the cut only if  $E_{\pi}^{rs} - E_{abc} > 10$  MeV.

#### 4.3.6 Kinematics

Kinematic quantities resulting from track reconstruction are used in two independent ways: for a pion-muon particle identification cut, and for the spectrum (or "Box") cut, which selects the part of the  $K^+ \rightarrow \pi^+ \nu \bar{\nu}$  phase space that is between the  $K_{\pi 2}$  and  $K_{\mu 2}$  peaks. The first cut uses only the measurements of range in the range stack and momentum in the drift chamber to test particle-mass hypotheses; it

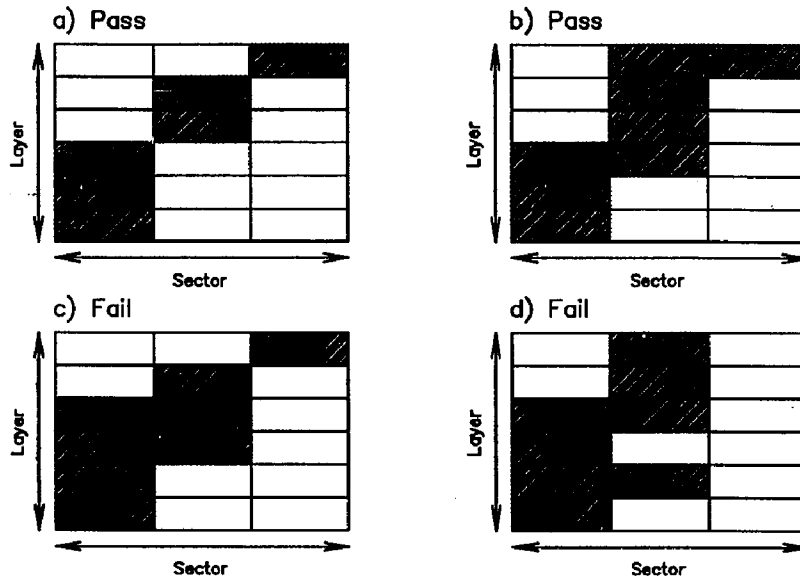


Figure 43. The PRPAT cut. RS tracks that would pass (a & b) and fail (c & d) the pattern cut. The latter two fail on the assumption that a clean single track event cannot exhibit sector crossings in more than one layer at any given sector boundary. (Shaded blocks indicate prompt hits.)

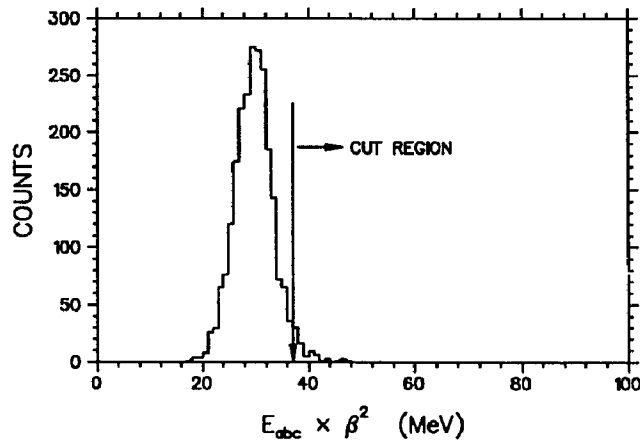


Figure 44. The BETASQ Cut. The quantity  $E_{abc} \times \beta^2$  is plotted for selected  $\pi$ -scat triggers that have already passed all of the other photon veto cuts. The arrow indicates the position of the cut.

thus avoids the target-based corrections to these quantities and takes advantage of the best possible resolution. Conversely, the second cut is based on the total kinematic quantities and can therefore exploit the monochromaticity of the primary background processes. In what follows, I describe how the track segments from the range stack and drift chamber are used for the former, and how the segments are linked together to form total kinematic quantities for the latter.

#### 4.3.6.1 Range-Momentum

The range-momentum cut is used to distinguish pions from muons by comparing the measured range in the range stack with that predicted by the particle's momentum. The predicted range is calculated by numerical integration of the *Bethe-Bloch* equation over the limits of the measured momentum. Both predicted and measured range differ for pions and muons. The measured range for a pion hypothesis,  $R_{\pi}^{rs}$ , was described in Section 4.3.1. A measurement for the muon hypothesis,  $R_{\mu}^{rs}$ , is similarly obtained but the energy-based correction for the path length in the last layer is suitably modified. Specifically, the energy of a decay muon is not subtracted from  $E_{last}^{rs}$ , and the *Bethe-Bloch* integration is made assuming a muon mass, rather than a pion mass.

The predicted ranges are defined by

$$R_i^0 = \int_{\sqrt{P_{dc}^2 + m_i^2}}^0 \frac{1}{\frac{dE}{dx}(m_i, E)} dE$$

where  $i$  specifies the  $\pi$  or  $\mu$  hypothesis,  $m_i$  is the mass of particle  $i$ ,  $P_{dc}$  is the momentum measured in the drift chamber, and  $dE/dx$  is the expression for energy loss in MeV/cm of scintillator. The lower limit of integration is the particle's energy as it enters the range stack.

A distribution of measured minus predicted range for a test sample of selected  $\pi$ -scat triggers\* is centered not at zero but at .7 cm. The offset originates in the momentum measurement, which comes out systematically low (see next section), and thus tends to underestimate the predicted range. Nevertheless, since we determine the cut's position and acceptance empirically from data, consistency is more the issue than precision. Therefore, in our definition of the likelihood of each mass

---

\* The  $\pi$ -scat trigger, which was alluded to in Section 2.1, is defined in Chapter 5, along with our method of sample selection.

hypothesis, we are free to center the distribution by subtracting an equivalent offset. We define the likelihood as

$$L_i \equiv \exp \left[ - \frac{(R_i^{\text{rs}} - R_i^0 - \delta_R)^2}{2\sigma_R^2} \right]$$

where  $i$  specifies  $\pi$  or  $\mu$ ,  $\sigma_R$  is the width of the “ $R - R^0$ ” distribution (2.7 cm), and  $\delta_R$  is the offset from zero (.7 cm). The logarithm of the relative likelihood is plotted in Figure 45 for pions and muons. The “spike” at  $-6$  is an artifact of our treatment of numerical underflows, which are defaulted to this value.

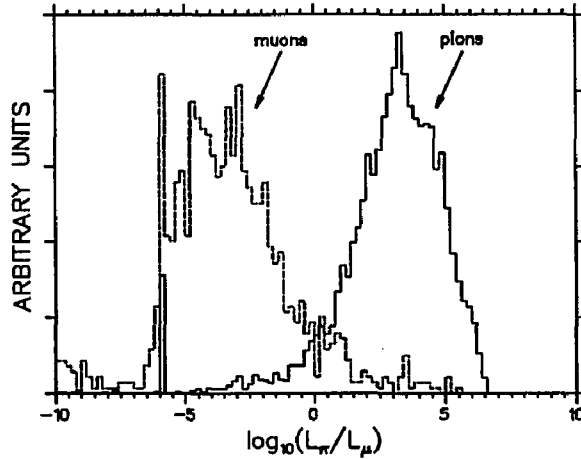


Figure 45. The log of the relative likelihood for kinematic particle identification. The muon test sample is derived from  $K_{\mu 2}$  events that stop in layers 19 or 20 of the range stack, well beyond the reach of pions from  $K_{\pi 2}$  decays. The pion test sample consists of  $\pi$ -scat events that have been tagged for the  $\pi^+ \rightarrow \mu^+ \rightarrow e^+$  decay sequence with the TD's.

Cuts based on the pion and relative likelihoods were made at Passes 1 and 3, as summarized in Table 11. We started at Pass 1 with what we thought was a loose cut called RNGMOM. However, we learned afterwards that there were two problems with it:

- Due to an oversight, the  $\delta_R$  offset was not applied. The cut had been tuned using the analysis of an older data set in which the range analysis differed slightly and caused the offset to cancel. More recent improvements to the range measurement led to a non-zero offset but it was not noticed until after Pass 1 was completed.

- A correction to the range using  $z$  information from the range stack chambers actually worsened the resolution. (Recall that the range reconstruction employs RSPC position to correct the track's trajectory.)

In the subsequent analysis, we reverted to a calculation of range that uses only a  $\varphi$  correction, and we corrected the offset. Future work includes a study of the RSPC corrections; meanwhile, we determined that the acceptance loss due to the errors was only 5%, so Pass 1 was not rerun. With the oversights corrected at Pass 3, we placed the cut RNGMOM2, as shown in the table. The cut position is determined empirically from Figure 45, which reflects these changes, as well.

Range-Momentum Cuts			
Pass	Name	RSPC Correction	Requirement
Pass 1	RNGMOM	$\varphi$ and $z$	$L_\pi > .01$ , or $\log_{10}(L_\pi/L_\mu) > -1$
Pass 3	RNGMOM2	$\varphi$ only	$\log_{10}(L_\pi/L_\mu) > 0$

Table 11. Summary of the range-momentum cuts.

#### 4.3.6.2 Energy, Momentum, Range and the "Box" Cut

The calculation of kinematic quantities used for the final spectrum, or "Box," cut is made in two steps. First, the three variables are calculated in "raw" form by linking together appropriate quantities from the track segments to form totals for energy, range and momentum. Measurements of the peak positions for selected  $K_{\pi 2}$  and  $K_{\mu 2}$  decays in data and Monte Carlo show systematic discrepancies with the true values.\* Therefore, a second step is made to correct the scales. In both data and Monte Carlo, this allows us to place the Box cut on the true scale instead of relative to the measured peaks; we apply the cut to simulated events to measure the acceptance.

The raw total energy is simply the sum of the individual segments and is given

\* A Monte Carlo simulation of the detector and trigger is used to generate events of standard decays for comparison with actual data, and of rare decays for acceptance measurements. Details are given in Chapter 5.

by

$$E_{total}^{raw} = E_{\pi}^{tgt} + E_{\pi}^{ic} + E_{\pi}^{rs}.$$

The total range is given by

$$R_{total}^{raw} = R_{\pi}^{tgt} + R_{\pi}^{ic} + R_{iw}^{dc} + R_{ow}^{dc} + R_{\pi}^{rs},$$

where  $R_{iw}^{dc}$  and  $R_{ow}^{dc}$  account for the path length of the particle in the inner and outer walls of the drift chamber, expressed in equivalent centimeters of scintillator. These are measured with drift chamber directional information in the same manner as  $R_{\pi}^{ic}$ . (Incidentally,  $R_{ow}^{dc}$  is included in the range component of the range-momentum cut.)

The calculation of total momentum is not as straightforward. We must account for the momentum loss of the particle in the target, which could be easily done using the measured energy in the target. However, owing to dead material (glue, which does not scintillate), this does not offer the best resolution. Instead, we use the target path length, including everything prior to the drift chamber:

$$R_{tgt}^l = R_{\pi}^{tgt} + R_{\pi}^{ic} + R_{iw}^{dc}.$$

Now we want to convert  $R_{tgt}^l$  into an equivalent momentum but we have to be careful to use the right part of the  $dE/dx$  curve. Therefore, we convert  $P_{dc}$  into an equivalent path length, add to it  $R_{tgt}^l$ , and convert the result back into momentum. Thus, we arrive at a value for total momentum where the only input measurements are  $P_{dc}$  and  $R_{tgt}^l$ . (A pion mass is assumed throughout.)

We use the well-defined two-body  $K_{\pi 2}$  and  $K_{\mu 2}$  peaks to test the accuracy and precision of the kinematic measurements. Raw totals are summarized in the top section of Table 12. Note the discrepancies with the true values, as well as between data and Monte Carlo. Although not all of these are accounted for (some are mentioned below), this turns out not to be a problem. Kinematic accuracy is an issue only in that the acceptance of kinematic cuts applied to the data must be measured consistently, *e.g.*, with properly simulated rare events. Therefore, it is sufficient to apply the small empirical corrections to remove systematic effects (to both data and Monte Carlo). To the extent that the  $K_{\pi 2}$  and  $K_{\mu 2}$  measurements come out as expected, use of a similar analysis for the rare modes is justified.

Corrected quantities are summarized in the second section of Table 12. In the analysis of the physics data the charged particle—whether pion or muon—must be treated with a pion hypothesis. Since the same analysis is applied to the test cases, we cannot expect to measure the true value for the  $K_{\mu 2}$  peak because we have knowingly treated a muon as a pion. Therefore, the goal of the correction procedure

is first to get the  $K_{\pi 2}$  Monte Carlo to agree with the true value, and then to get the analysis of the  $K_{\pi 2}$  and  $K_{\mu 2}$  data to agree with their Monte Carlo counterparts.

Corrections are applied for known effects such as energy deposited in the dead material of chamber walls, saturation in the scintillator and, in the Monte Carlo, the resolution effects of timing and photo-statistics. Ultimately, we resort to empirical transformations that rescale and shift the variables.

Raw	$P_{total}^{raw}$ (MeV/c)			$E_{total}^{raw}$ (MeV)			$R_{total}^{raw}$ (cm of scint.)		
	Peak	$\sigma$	%	Peak	$\sigma$	%	Peak	$\sigma$	%
$K_{\pi 2}$ DATA	203.0	5.6	2.7	98.4	3.9	4.0	30.29	1.26	4.2
$K_{\pi 2}$ UMC	205.1	4.2	2.0	103.4	1.4	1.3	30.96	1.12	3.6
$K_{\mu 2}$ DATA	234.4	7.2	3.1	142.1	4.4	3.1	52.23	2.99	5.7
$K_{\mu 2}$ UMC	237.3	5.4	2.3	143.7	1.3	0.9	52.19	2.81	5.4
Corrected	$P_{total}$ (MeV/c)			$E_{total}$ (MeV)			$R_{total}$ (cm of scint.)		
	Peak	$\sigma$	%	Peak	$\sigma$	%	Peak	$\sigma$	%
$K_{\pi 2}$ DATA	204.9	5.6	2.7	108.5	3.8	3.5	no correction		
$K_{\pi 2}$ UMC	204.1	5.1	2.5	108.4	4.1	3.8	30.31	1.15	3.8
$K_{\mu 2}$ DATA	236.3	7.2	3.1	151.5	4.4	2.9	no correction		
$K_{\mu 2}$ UMC	236.3	6.5	2.7	149.5	4.6	3.1	52.25	2.88	5.5
True Value	$P_{total}$ (MeV/c)			$E_{total}$ (MeV)			$R_{total}$ (cm of scint.)		
$K_{\pi 2}$	205.14			108.55			30.37		
$K_{\mu 2}$	235.53			152.48			54.34		

Table 12. Summary of kinematic measurements. The selection cuts applied to both the data and UMC samples are the same as those used for the branching ratio measurements described in Chapter 6. Peak and sigma values are from gaussian fits; the “%” columns are sigma divided by the value of the peak.

The Box cut places final limits on the total kinematic quantities. The choice of the cut positions are dictated by the kinematics of the two-body background modes and by the resolution with which the kinematic variables are measured. As noted in Section 2.1, the separation between the  $K_{\pi 2}$  and  $K_{\mu 2}$  peaks is the narrowest in momentum. This is especially so when it is expressed in terms of the resolution: using the mean value of sigma for corrected data in Table 12, we find that the approximate separation in momentum is  $5\sigma_p^{av}$ , whereas in range and energy it is

$10\sigma_{\text{R}}^{av}$  and  $10\sigma_{\text{E}}^{av}$ , respectively. Therefore, we place relatively tight cuts in energy and range, while the cut in momentum is applied mainly to bolster the rejection in anticipation of further running of the experiment. The lower limits on range and energy are placed approximately  $2\sigma$  above the  $K_{\pi 2}$  peak, and the upper limits,  $2\sigma$  above the  $K^+ \rightarrow \pi^+ \nu \bar{\nu}$  endpoint. The momentum cut is simply tuned for a factor of two in background reduction. Thus, we require:

$$115 < E_{total} < 135 \text{ MeV} \quad (127)$$

$$33 < R_{total} < 42 \text{ cm} \quad (38)$$

$$205 < P_{total} < 243 \text{ MeV}/c \quad (227)$$

where the numbers at right refer to the endpoint of the  $K^+ \rightarrow \pi^+ \nu \bar{\nu}$  spectrum. The cuts were illustrated in Figure 32; we note again that even prior to the application of the momentum cut, range and energy leave us with no candidate events.

#### 4.3.7 Beam Cuts

The philosophy of the beam cuts is based on a layered defense designed to reject two classes of events, as illustrated in Figure 46: single-beam-particle events triggered by a scattered pion and double-beam-particle events consisting of a kaon followed by a scattered pion. The primary cut for both event types is to veto on a  $\tilde{C}_\pi$  signal in time with the range stack. However, due to a small but non-negligible inefficiency in the Čerenkov counter two more cuts are needed. A  $dE/dx$  cut in B4 rejects prompt scattered pions that survive the delayed coincidence cuts and fail to register a  $\tilde{C}_\pi$  signal, while a complementary cut based on B4 transient recorder data rejects double-beam-particle events via their characteristic two-pulse signature. Note that the latter event type consists partially of a kaon and, therefore, tends to pass the  $dE/dx$  cut. The three cuts are described below.

- $\overline{\tilde{C}_\pi^n}, \overline{\tilde{C}_\pi^w} \Rightarrow$  Veto events that have a  $\tilde{C}_\pi$  signal in coincidence with  $t_\pi^{rs}$ . We start with a loose cut at Pass 2 using a narrow window of  $\pm 4$  nsec and widen it at Pass 3 to  $\pm 7$  nsec.
- $B4_{dE/dx} \Rightarrow$  For events with  $t_\pi^{rs} < 2$  nsec, the summed energy in the B4XY hodoscope is required to be greater than 4 MeV. The cut position is set empirically using the B4 energy spectrum for kaons tagged by  $K_{\mu 2}$  decays.
- $B4_{fit} \Rightarrow$  Veto event if two pulses are found in the B4 TD data with the same time separation as the apparent kaon decay time,  $t_\pi^{rs}$ . The pulse-shape data are analyzed by an algorithm similar to FITPI, which returns quality-of-fit values for single- and double-pulse fits, as well as the relative time and area

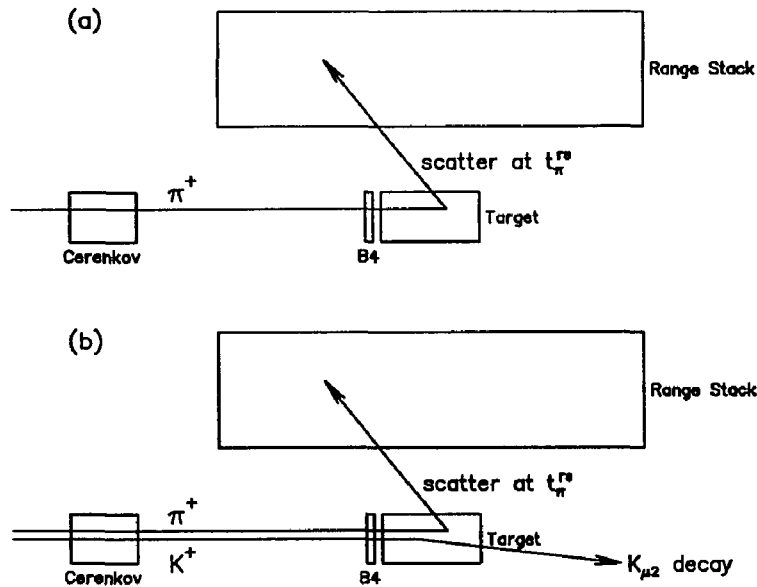


Figure 46.  $\pi$ -scat events. Both event types are rejected if they have a  $\bar{C}_{\pi}$  hit in time with the range stack track. Type (a) events are further suppressed by requiring high B4 pulse height, and type (b) by vetoing on a double-pulse in B4. (Not to scale.)

Requirements to veto event	Description
$\log_{10}(C_{B4}^{(1)}) > 1.8$	Poor single-pulse fit
$E_{B4}^{(2)} > 10$ counts	Minimum second-pulse area
$\Delta t_{B4}^{(2)} - t_{\pi}^{rs} + 2.5 < 6$ . nsec	B4 pulse separation agrees with K decay time

Table 13. Summary of the quantities used in the  $B4_{fit}$  analysis. Superscripts refer to the 1- or 2-pulse fits.

of the second pulse for the two-pulse fit. The cut quantities and parameters are summarized in Table 13. It turns out that the cut also rejects some  $K_{\pi 2}$  events in which a photon has showered in B4.

## 4.4 SUMMARY OF THE CUTS

The cuts and their rejection factors are summarized for each analysis pass. By rejection we mean the factor by which the sample is reduced when a cut is applied. Thus, an increase in sensitivity is achieved when the rejection of a cut is greater than the inverse of its acceptance, or more simply, when a cut rejects more events than it would due to its acceptance loss alone. For some of the cuts that we apply this would appear not to be the case, but that is because rejection is actually not a well-defined quantity. Rather, it depends strongly upon the composition of the sample on which it is measured, *i.e.*, on the type of background events that remain. For example, given the three main backgrounds—photons, muons, and  $\pi$ -scats—if the sample is largely dominated by  $K_{\pi 2}$  events and we subject it to a cut that is meant to suppress muons, then the rejection will tend to appear low. Yet, if we measure the rejection of the cut on only the events on the high end of the spectrum, which is where the muons are, then the rejection looks quite high.

Pass 1 Summary	
Cut	Rejection
PREFIT	2.14
Target Setup	1.03
RS/DC Setup	1.16
RNGMOM	1.95
$D_{tgt}$	1.23
FITPI	1.61
Net	9.86

Table 14. Summary of Pass 1 cuts and typical rejection factors. Due to availability, only a representative set of statistics is shown.

Pass 2 Summary			
Cut	Events In	Events Cut	Rejection
TG/RS Setup	859134	2720	1.003
$\overline{\gamma}_n$	856414	664012	4.451
Delayed Coincidence	192402	64717	1.507
$\tilde{C}_\pi^n$	127685	19509	1.180
$z_{14}$	108176	31478	1.410
$\theta_D$	76698	4167	1.057
RNGMOM	72531	74	1.001*
$D_{tgt}$	72457	224	1.003*
$\overline{\gamma}_{tgt}$	72233	20274	1.390
FITPI	51959	31	1.0006*
FITPI2	51928	17391	1.504
ELVETO	34537	20743	2.504
Duplicate Events <sup>†</sup>	13794	74	1.005
Net	—	—	62.6

Table 15. Summary of Pass 2 cuts shown in order of their application. Additional setup costs are incurred due to timing reconstruction in the target and range stack. \*As a monitor on the stability of the analysis, cuts from previous passes are re-applied—in these cases the choice of calibration files was finalized. Since tighter versions of each of these cuts are applied at Pass 3 the acceptance of the final cuts is unaffected by the calibration update. †Operator errors at Pass 0 caused some runs to be duplicated; extra events were eliminated.

Pass 3 Summary			
Cut	Events In	Events Cut	Rejection
$\overline{\gamma}_w$	13720	3774	1.379
PRPAT	9946	193	1.020
BETASQ	9753	510	1.055
$\Delta t_\pi$	9243	3411	1.585
$\tilde{C}_\pi^w$	5832	106	1.019
$B4_{\text{fit}}$	5726	453	1.086
$B4_{dE/dx}$	5273	59	1.011
$z'_{14}$	5214	44	1.009
$\theta_D^n$	5170	207	1.042
RNGMOM2	4963	510	1.115
$D'_{\text{tgt}}$	4453	47	1.011
$z_{\text{tgt}}$	4406	7	1.002
$\overline{\gamma}_{\text{tgt}}$	4399	11	1.003*
$\gamma'_{\text{tgt}}$	4388	483	1.127
TG <sub>gap</sub>	3905	60	1.016
$\Delta R_{\text{tgt}}$	3845	130	1.035
$R_{\text{IC}}$	3715	7	1.002
$\mu^+ \rightarrow e^+$	3708	1092	1.417
FITPI3	2616	422	1.192
ELVETO3	2194	133	1.065
TDFOOLERY	2061	10	1.005

Table 16. Summary of Pass 3 cuts in order of their application. \*A calibration update caused a few additional events to be rejected when re-applying this Pass 2 cut at Pass 3.

## 5. The Sensitivity

### 5.1 INTRODUCTION

Now that we have searched the data for a signal, it is time to describe how we determine the effective number of kaons observed, that is, the product of the total number of kaons (the flux) times the fraction of signal events that would survive the full online and offline selection chain (the acceptance). Having found no candidate events, we can then extract branching ratio upper limits for the rare processes. The calculation of the acceptance, which dominates the bulk of this chapter, is a very involved procedure as we must account for the inefficiency of each and every trigger criterion and analysis cut. At our present sensitivity we must suppress the background by some eleven orders of magnitude; in doing so we unavoidably reduce the acceptance for the desired signal, to 0.50% for  $K^+ \rightarrow \pi^+ \nu \bar{\nu}$  and 2.3% for  $K^+ \rightarrow \pi^+ f$ . The acceptance is higher in the second case because two-body kinematics put the  $\pi^+$  between the  $K_{\pi 2}$  and  $K_{\mu 2}$  peaks so losses due to spectrum cuts are minimal.

At first, the acceptances may seem low but note that they represent a signal-to-noise enhancement of about  $10^9$ . Also, most of the inefficiency is due to just a few effects, whose losses are at best difficult to reduce without major changes in the detector hardware; moreover, some losses are intrinsic limitations of the basic strategy of the experiment.\* The main effects are:

- Particle lifetimes. We survey the kaon lifetime (12.4 nsec) from 2–50 nsec, the pion (26.0) from 9–120 nsec, and the muon (2197) from 20–6100 nsec; the limits are determined by finite bandwidth, dynamic range, and timing

---

\* Planned improvements to the experiment focus on increasing the kaon intensity, along with requisite upgrades to handle the increase, e.g., faster triggering and data acquisition.

resolution. The fraction of events that survive the timing of the decay chain is 54%; however, under “battle conditions” the losses are somewhat higher because more than just timing cuts are needed to reject background events.

- Solid angle coverage. Charged particles are tracked over about half the total solid angle. Since we define the flux according to stopped kaons in the target, the geometric acceptance of the detector is included as an efficiency loss.
- Nuclear interactions and decays in flight. About half the signal pions are absorbed or decay before they stop. (This “robs” them of their characteristic three-pulse decay sequence, the observation of which is required for complete background suppression.)
- Accidental vetoes. In rejecting events with photons, we veto true single-track events about 20% of the time because of unrelated accidental hits occurring in coincidence with the kaon decay. Vetoing on activity outside the stopping counter at the time of the pion decay, as described in Section 4.3.4.1, costs another 7%.
- Track reconstruction. Chamber reconstruction in the trigger and offline analysis amounts to a 25% loss. (This sizeable loss breaks down to several smaller effects: 8% is due to a wire break in the central drift chamber during the latter part of the run, which caused a section of it to be shut down; 6% is due to sector gaps between the range stack chambers; the remainder is split among track-fitting and/or wire-related inefficiencies.)
- Kinematic spectrum. All but approximately 20% of the  $K^+ \rightarrow \pi^+ \nu \bar{\nu}$  spectrum lies outside the various kinematic cuts that begin with the trigger and culminate with the energy-range cut depicted in Figure 32b.

The product of the acceptance factors associated with the above effects is 1.5%. The rest of the losses are due to small inefficiencies distributed over the remaining cuts which are further necessary to reduce background.

\* \* \*

A standard approach for measuring the acceptance for a rare process is to normalize to the branching ratio measurement of a known process. Owing to the complex nature of our detector and systematic differences in the event selection procedure between  $\pi^+ \nu \bar{\nu}$  and the known final states ( $\mu^+ \nu$  and  $\pi^+ \pi^0$ ), it has been necessary to adopt a different approach. We determine the acceptance of individual

cuts, measuring a factor for each such that the product gives the overall acceptance.<sup>†</sup> In so doing, we come to understand the loss entailed by requiring each individual cut, which not only allows us to optimize the cut position, but assures us that some large systematic effect has not been overlooked.

For the most part, the factors themselves are measured with actual data that is triggered on known processes that mimic specific aspects of the rare decays; only a few factors need a Monte Carlo simulation to determine them. Detector data has an advantage over simulated events because it accounts for the true performance of the instrumentation. Also, since the data we use are “monitor triggers” accumulated over the full course of the run—concurrent with the physics data—we automatically account for the effects of bad channels, broken wires, intensity variations, and the like. Also, since acceptance factors are measured separately for each cut, we can choose the type of monitor trigger that is best suited for the cut in question. By working with different processes, we essentially have a composite of the basic characteristics of  $K^+ \rightarrow \pi^+ \nu \bar{\nu}$  and  $K^+ \rightarrow \pi^+ f$  decays:  $K_{\mu 2}$  events are topologically similar,  $K_{\pi 2}$  events produce  $\pi^+$ 's of unique momentum, and  $\pi$ -scat triggers are a source of long-range pions.<sup>‡</sup>

In all but a few cases, acceptance factors are measured with a simple “counting method” illustrated by the flow chart in Figure 47. First, a sample of raw monitor triggers is prepared with a set of selection criteria drawn from our library of cuts. Then it is subjected to the cut whose acceptance we wish to measure. The ratio of events surviving to events examined determines the efficiency, while the surviving events themselves can be passed on to another cut in the sequence. For example, if we want to measure the delayed coincidence efficiency, we need a sample of stopped kaons. To get such a sample we start with  $K_{\mu 2}$  triggers and demand that every charged track has the right energy, range and momentum for a decay at rest. In addition, we demand that its relative “range-momentum” likelihood is consistent with that of a muon mass. We then impose the delayed coincidence requirements on the selected events, first (say) the trigger bit and then the offline cut, and measure the fraction that survive each.<sup>§</sup>

Although the order of application of the cuts is unimportant, it is essential to measure the acceptance of related ones in sequence, i.e., those that tend to fail

<sup>†</sup> In the measurement of acceptance, trigger requirements and analysis cuts are on an equal footing; in the interest of brevity, the term “cut” refers to either.

<sup>‡</sup> The special triggers that select these events are defined later in this chapter.

<sup>§</sup> Recall that the status of all trigger bits is recorded for all events whether or not they are required in the definition of the particular trigger that activated data acquisition. Thus, it is natural to use monitor triggers to measure the acceptance of many of the trigger criteria, in the same manner as the offline cuts.

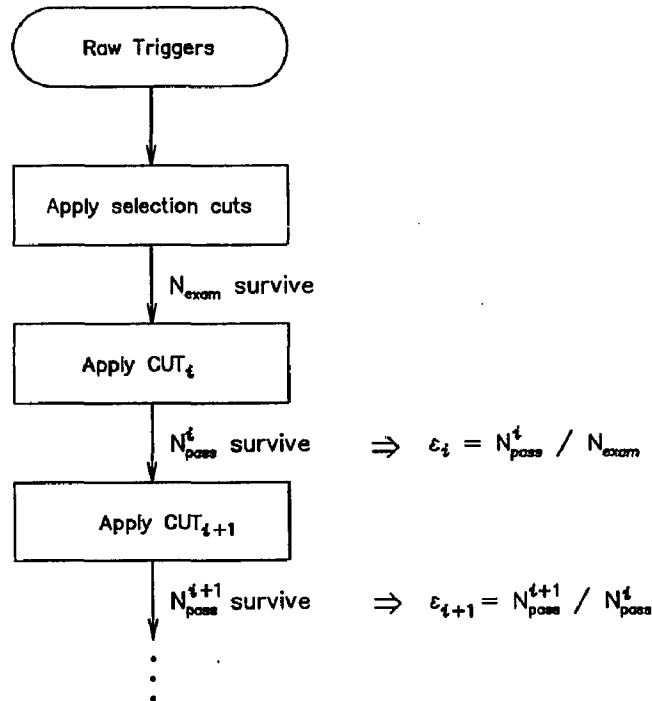


Figure 47. A flow chart for the “counting method” of determining acceptance factors.

events on similar detector information or similar physics, like the example above. Otherwise, we would clearly underestimate the acceptance by counting the same losses time and again. As we will see, considerations of correlated losses among the analysis cuts affect both why we group a particular set of cuts and measure their efficiencies from the same test sample and how we choose some other set of cuts to select that sample in the first place.

Still, a complication arises. Sample preparation may not be straightforward because of the difficulty of either selecting the appropriate test data or isolating specific effects that cause losses to an otherwise distinct groups of cuts. The former is illustrated by attempts to measure the reconstruction efficiency, where most of our would-be selection cuts themselves depend on the results of event reconstruction. On such occasions alternate methods are called for and introduced as needed.

The latter is illustrated by pion absorption, which affects the efficiency of our particle identification cuts by changing either the particle’s identity or its kinematics. Since our cuts are only capable of tagging pions that come to rest via electromagnetic energy loss alone, it is difficult to select a background-free sample

of test pions without discriminating against those that undergo nuclear interactions. This in turn makes it difficult to use real data to properly assess how nuclear interactions affect the efficiency. Therefore, we use the analysis cuts to prepare test samples free from interactions in order to measure particle identification efficiencies on "clean" pions. We then measure a separate acceptance factor for losses due to interactions alone using a Monte Carlo simulation, where we can assess their effect in a more controlled environment.

Since we thus make fair demands on the Monte Carlo regarding the simulation of nuclear interactions, we use it to make an independent check by measuring the  $K_{\pi 2}$  branching ratio, which also has a  $\pi^+$  in the final state and is thus similarly affected. This measurement is described at the end of the chapter and is preceded by a description of the Monte Carlo itself. Earlier in the chapter we give a summary table listing all of the acceptance factors. Measurements of the factors themselves are described according to four major groups according to the source of events used for the test samples. The first three are made with the monitor triggers mentioned earlier ( $K_{\mu 2}$ ,  $K_{\pi 2}$ , and  $\pi$ -scat), and the last with the Monte Carlo. Each section contains a description of the selection (or generation) of the test samples and the factors they are used to measure. We conclude with measurements of the flux and the  $K_{\mu 2}$  and  $K_{\pi 2}$  branching ratios that serve to check both it and the acceptance.

## 5.2 THE FACTORS

Table 17 is a complete list of the trigger criteria and analysis cuts, along with the values of their acceptance factors. As noted earlier, the acceptance is different for  $K^+ \rightarrow \pi^+ \nu \bar{\nu}$  and  $K^+ \rightarrow \pi^+ f$  because of the spectra of the  $\pi^+$ . This is reflected in the table by two entries for factors affected by kinematics, one measurement for each mode. Errors are, for the most part, statistical. In the few cases where the best method of sample preparation is not clear, we make alternative measurements in order to estimate a systematic error. In the end, however, the errors in our branching ratio limits are still dominated by the Poisson statistics of finding zero candidate events.

Item	Defined	Method		$K^+ \rightarrow \pi^+ f$	$K^+ \rightarrow \pi^+ \nu \bar{\nu}$
Level 0 trigger					
Delayed coincidence	3.3.1	$K_{\mu 2}$	5.3.2	$.864 \pm .004$	
$T \cdot A$ (Solid Angle)	3.3.2	UMC	5.6.2	$.459 \pm .004$	$.417 \pm .003$
$\mu$ veto - Accidentals	5.3.2	$K_{\mu 2}$	5.3.2	$.9991 \pm .0003$	
Range cut - $\mu$ -veto & B	3.3.2	UMC	5.6.2	$.9987 \pm .0005$	$.825 \pm .003$
$\bar{\gamma}$ - Accidentals	5.3.2	$K_{\mu 2}$	5.3.2	$.970 \pm .002$	
Level 1 trigger					
Hexant - Accidentals	3.4.1	$K_{\mu 2}$	5.3.2	$.990 \pm .001$	
11 <sub>CT</sub>	3.4.2	UMC	5.6.2	$.961 \pm .002$	$.507 \pm .005$
R.R.Reconstruction	3.4.2	$K_{\mu 2}$	5.3.2	$.883 \pm .004$	
MLU	3.4.2	UMC	5.6.2	$.927 \pm .004$	$.979 \pm .002$
Level 1.5 trigger					
One-and-only-one $T \cdot A$	3.6	$K_{\mu 2}$	5.3.2	$.9982 \pm .0005$	
Energy Cut	3.6	$K_{\pi 2}$	5.5.1	$.98 \pm .01$	$.9992 \pm .0008$
Transient Recorder					
$\pi^+ \rightarrow \mu^+$	4.3.4.1	$\pi$ -scat	5.4.2.1	$.54 \pm .05$	
$\mu^+ \rightarrow e^+$	4.3.4.2	$\pi$ -scat	5.4.2.2	$.845 \pm .006$	
ELVETO, ELVETO2	4.3.4.1	$\pi$ -scat	5.4.2.2	$.928 \pm .005$	
TDFOOLERY	4.3.4.1	$\pi$ -scat	5.4.2.2	$.9975 \pm .0009$	
$ST_{hex}$	5.5.2	$K_{\pi 2}$	5.5.2	$.958 \pm .002$	
FITPI3 Cuts					
TPIDIF	4.3.4.1	$\pi$ -scat	5.4.2.2	$.9977 \pm .0007$	
EMUAV	4.3.4.1	$\pi$ -scat	5.4.2.2	$.980 \pm .002$	
TDFLUC	4.3.4.1	$\pi$ -scat	5.4.2.2	$.959 \pm .003$	
PROD20	4.3.4.1	$\pi$ -scat	5.4.2.2	$.991 \pm .002$	
LOELAST	4.3.4.1	$\pi$ -scat	5.4.2.2	$.996 \pm .001$	
TMUPROD	4.3.4.1	$\pi$ -scat	5.4.2.2	$.995 \pm .001$	
RSHEX	4.3.4.1	$\pi$ -scat	5.4.2.2	$.9993 \pm .0005$	

Table 17. Acceptance table. Whenever two cuts are made on a given variable, a loose one followed by a tighter one in a subsequent pass, a single entry is given for the combined effect. The second column indicates in what section the cut was defined, the third where it was measured and with what event type. UMC refers to the E787 Monte Carlo program.

Item	Defined	Method		$K^+ \rightarrow \pi^+ f$	$K^+ \rightarrow \pi^+ \nu \bar{\nu}$
Analysis Cuts					
<b>Setup</b>					
Target	4.3.1	$K_{\mu 2}$	5.3.1	$.983 \pm .001$	
DC/RS	4.3.1	$K_{\mu 2}, K_{\pi 2}$	5.3.1	$.853 \pm .003$	
$\bar{\gamma}$ - Accidentals					
$\bar{\gamma}_n, \bar{\gamma}_w$	4.3.5	$K_{\mu 2}$	5.3.2	$.877 \pm .003$	
PRPAT	4.3.5	$K_{\mu 2}$	5.3.2	$.9982 \pm .0005$	
BETASQ	4.3.5	$\pi$ -scat	5.4.1	$.973 \pm .003$	
$\bar{\gamma}_{tgt}$	4.3.5	$K_{\mu 2}$	5.3.2	$.974 \pm .002$	
$\gamma'_{tgt}$	4.3.5	$K_{\mu 2}$	5.3.2	$.972 \pm .002$	
<b>Beam Cuts</b>					
$\bar{C}_\pi^n, \bar{C}_\pi^w$	4.3.7	$K_{\mu 2}$	5.3.2	$.986 \pm .001$	
$B4_{fit}$	4.3.7	$K_{\mu 2}$	5.3.2	$.978 \pm .002$	
$B4_{dE/dz}$	4.3.7	$K_{\mu 2}$	5.3.2	$.991 \pm .001$	
$z_{tgt}$	4.3.1.4	$K_{\mu 2}$	5.3.2	$.9998 \pm .0002$	
TARGF	4.3.1.4	$K_{\mu 2}$	5.3.2	$.982 \pm .002$	
$\Delta R_{tgt}$	4.3.1.4	$K_{\mu 2}$	5.3.2	$.973 \pm .002$	
$R_{IC}$	4.3.1.4	$K_{\mu 2}$	5.3.2	$1.0000 \pm .0002$	
Dly'd Coin.	4.3.3	$K_{\mu 2}$	5.3.2	$.943 \pm .003$	
$\Delta t_\pi$	4.3.1.4	$K_{\mu 2}$	5.3.2	$.997 \pm .002$	
$D'_{tgt}, D'_{tgt}$	4.3.1.4	$K_{\mu 2}$	5.3.2	$.9985 \pm .0005$	
$z_{14}, z'_{14}$	4.3.2	UMC	5.6.2	$.963 \pm .003$	$.985 \pm .002$
$\theta_D, \theta_D^n$	4.3.2	UMC	5.6.2	$.970 \pm .002$	
RNGMOM and RNGMOM2	4.3.6.1	$\pi$ -scat	5.4.1	$.881 \pm .005$	$.891 \pm .005$
BOX	4.3.6.2	UMC	5.6.2	$.962 \pm .003$	$.417 \pm .017$
Line Items					
No decay in flight or nuclear interactions	5.6.2	UMC	5.6.2	$.48 \pm .01$	$.53 \pm .02$
Pion stop in scint.	5.6.2	UMC	5.6.2	$.979 \pm .002$	$.985 \pm .002$
<b>The Acceptance</b>				$0.0235 \pm .0023$	$0.0050 \pm .0005$

Table 17. Acceptance table (continued). The overall acceptance is the product of the factors in each column. "Line items" are effects mentioned in the previous section that are difficult to properly isolate in the data, and are thus measured independent of any particular cut.

### 5.3 $K_{\mu 2}$ MEASUREMENTS

Losses due to reconstruction, photon veto and beam accidentals, and timing are measured using a sample of  $K_{\mu 2}$  monitor triggers spanning the full run. The  $K_{\mu 2}$  trigger is defined as

$$KT \cdot (T \cdot A) \cdot B_{CT} \cdot (19_{CT} + 20_{CT} + 21_{CT}),$$

where the terms are the Level 0 trigger bits described in Chapter 3. Since the intrinsic rate of this monitor trigger (and all of them, for that matter) is very high, we impose a "prescale" condition before writing events to tape. A scaler is incremented each time the trigger condition is valid and when it reaches the large integer value  $N_{ps}$ , data from the last event is acquired and the scaler is reset. By tuning the value of  $N_{ps}$  for each monitor trigger, we control the amount of calibration data recorded along with the physics data.

The  $K_{\mu 2}$  measurements are made in two parts. First, we measure the offline reconstruction efficiency using a set of minimum-bias cuts to select the  $K_{\mu 2}$  decays. Then, after reconstruction is complete, analysis cuts are applied to select a sample with which to measure the acceptance of the remaining items.

#### 5.3.1 Offline Reconstruction

As noted earlier, we encounter our first difficulty with sample selection when we try to measure the reconstruction efficiency of the target, drift chamber, and range stack because our would-be selection cuts depend on the results of reconstruction. Recall that the reconstruction requirements (see "setup" cuts in Section 4.3.1) are that we find a track segment in each system, and that in the target and range stack we also find its time. Therefore, we seek a pure sample of clean single-track events from the decays of stopped kaons, *e.g.*,  $K_{\mu 2}$  decays, and ask what fraction are successfully reconstructed.

The problem is that the only selection criteria available prior to reconstruction are the online results stored in the trigger bits. Although the bits are quite effective, they leave us with a sample that is contaminated with short or fragmented tracks that have "tricked" the  $K_{\mu 2}$  trigger with the help of a photon or accidental that hits one of the outer layers and appears to extend the track. A simple way of boosting the sample purity is thus to measure the energy of the track and require that it lie in the  $K_{\mu 2}$  peak. Equivalently, we make a plot of the track energy and use it for event counting by subtracting the flat background caused by the "junk" tracks. We proceed as follows:

- We require the delayed coincidence trigger bit in order to select stopped kaons. This is important to the target analysis, which attempts to resolve the decay vertex, and it also makes the track energy well-defined. Furthermore, the implicit I-counter requirement, along with  $T \cdot A$ , restricts the track to the angular acceptance of the drift chamber, as was discussed in relation to Figure 15.
- We veto on the outermost layer of the range stack using the  $X_{CT}$  bit for layer 21. This is needed to contain the tracks in the range stack so that the energy will be properly measured.
- We apply the target reconstruction program. Since the losses are primarily due to random hits and are thus not a strong function of sample selection, the above events are sufficient for measuring the target setup efficiency. We find:

$$\epsilon_{TG} = .983 \pm .001,$$

where the error is statistical.

The remaining steps are specifically for the drift chamber and range stack:

- We measure the track energy in the range stack using a simple 99.8%-efficient algorithm. The contribution from the target is added and the result is plotted (Figure 48a). We use a fit to a gaussian plus flat background to determine the number of counts in the peak above background, which gives the denominator for the efficiency measurement, that is, the number of events in the sample prior to drift chamber and range stack (DC/RS) reconstruction.
- We apply DC/RS reconstruction. For organizational reasons, a single factor is used for both of these sub-systems.
- The track energy is plotted again for all events that are successfully reconstructed (Figure 48b). Fitting in the same manner as above gives the number of reconstructed  $K_{\mu 2}$  tracks.

The relative number of events above the background gives the efficiency. We find:

$$\epsilon_{DC/RS} = .853 \pm .003,$$

where the error is statistical. We note that the monitor sample used for the above measurement was taken uniformly over the full course of the run. Thus, the loss of efficiency caused by a broken wire in (and partial shutdown of) the central drift chamber in the last two weeks of running is included in the above result. Measurements before and after the break indicate a relative loss of approximately 33% in a system that is otherwise 95% efficient.

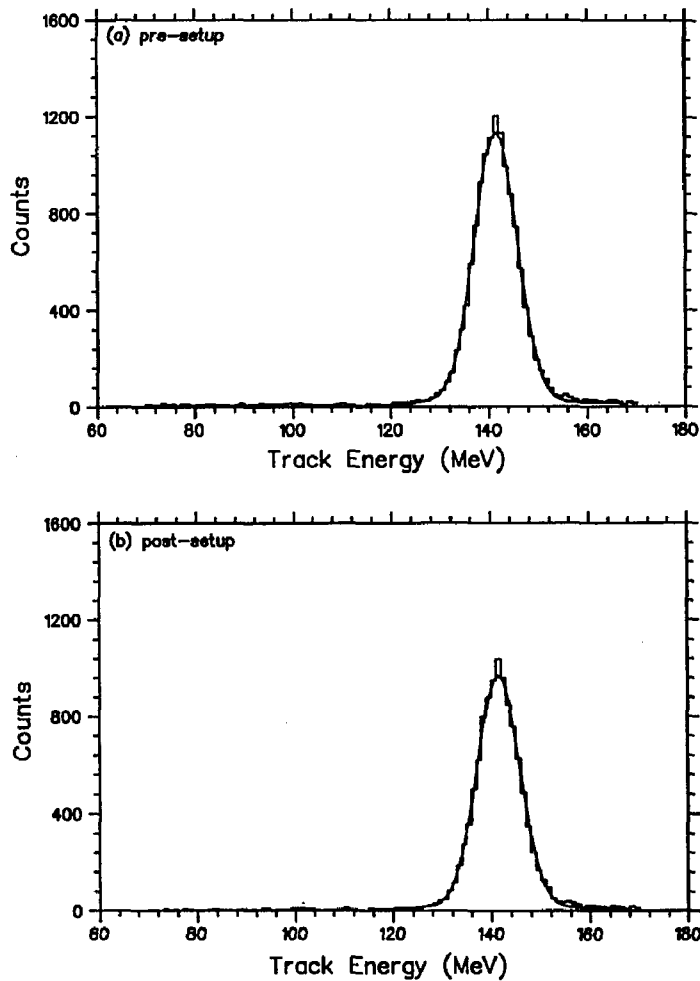


Figure 48. The track energy including the contribution from the target is plotted a) before and b) after track reconstruction in the drift chamber and range stack. A fit to a gaussian plus a flat background over the range  $120 < E < 165$  MeV reveals the number of events in the  $K_{\mu 2}$  peak.

### 5.3.2 Accidentals, Beam Cuts and Timing

The counting method is applied to  $K_{\mu 2}$  events to measure the acceptance of cuts that depend on having a kaon in the target and beam counters, a single track in the charged-particle region of the detector, and no photons, anywhere.  $K_{\mu 2}$  events that survive track reconstruction are further selected to meet the above requirements.

The range-momentum cut is inverted so as to select muons (rather than pions). Also, tight kinematic cuts of  $\pm 1.5\sigma$  in momentum, energy, and range, centered about the  $K_{\mu 2}$  peak, ensure that the muon is from a kaon decay at rest;  $\sigma$  is the width of the various distributions, as summarized in Table 12.

In addition, we apply the delayed coincidence as part of the overall selection process. At the end, once the other factors are measured, we relax it and use the other cuts to select the sample for its acceptance measurement. This allows the other cuts to benefit from delayed coincidence selection, but avoids over-counting losses in the delayed coincidence measurement itself. The cut statistics are summarized in Table 18; details of the less obvious items are given below.

- Level 0  $\gamma$  veto  $\Rightarrow$  Accidental losses for the online veto are measured by checking the status of the prerecorded trigger bits *BV*, *ECM*, and *ECP*. Although the online threshold is higher than the offline, there are additional losses because the effective coincidence window is wider in the trigger sums. Similar losses are incurred for the hexant cut and the one-and-only-one  $T \cdot A$  requirement of Level 1.5.
- Level 0  $\mu$  veto  $\Rightarrow$  The veto on RS layers 19–21 suffers from accidental losses because if an unrelated hit lands deep in the “feed-forward” region of the range stack established by  $T \cdot A$ , then the Level 0 range measurement is artificially extended (the range measurement was discussed in Section 3.3.2). We note that the acceptance loss for “real” tracks that reach that far is measured separately using the Monte Carlo.
- R.R. Reconstruction  $\Rightarrow$  This refers to the success of the Level 1 refined range measurement described in Section 3.4.2. Losses occur due to imperfect geometric coverage (gaps between sectors; 6%), chamber inefficiencies (5%), and accidentals (we require valid chamber information in not more than one sector; 1%).
- Dly’d Coin.  $\Rightarrow$  As mentioned above, we exploit the monochromaticity of  $K_{\mu 2}$  decays to select a test sample of stopped kaons by applying kinematic cuts to the charged track to ensure that it is a muon from a  $K^+$  decay at rest.

Cut	# Passing	Efficiency
Selection	8920	—
$\overline{\gamma_n}, \overline{\gamma_w}$	7819	.877 ± .003
PRPAT	7805	.9982 ± .0005
Level 0 $\gamma$ veto	7573	.970 ± .002
Level 0 $\mu$ veto	7566	.9991 ± .0003
Level 1 Hexant	7490	.990 ± .001
Level 1 R.R. Reconstruction	6610	.883 ± .004
Level 1.5 One-and-only-one $T \cdot A$	6598	.9982 ± .0005
$\Delta t_\pi$	6448	.997 ± .002
$\tilde{C}_\pi^n, \tilde{C}_\pi^w$	6355	.986 ± .001
B4 <sub>fit</sub>	6216	.978 ± .002
B4 <sub>dE/dx</sub>	6157	.991 ± .001
$D_{tgt}, D'_{tgt}$	6148	.9985 ± .0005
$z_{tgt}$	6147	.9998 ± .0002
$\overline{\gamma}_{tgt}$	5990	.974 ± .002
$\gamma'_{tgt}$	5820	.972 ± .002
TARGF	5718	.982 ± .002
$\Delta R_{tgt}$	5566	.973 ± .002
$R_{IC}$	5566	1.0000 ± .0002
Restore Dly'd Coin. events	6737	—
Level 0 Dly'd Coin.	5823	.864 ± .004
Offline Dly'd Coin.	5494	.943 ± .003

Table 18. The  $K_{\mu 2}$  monitor sample used to measure photon veto and beam accidentals, timing losses, and some miscellaneous items.

#### 5.4 $\pi$ -SCAT MEASUREMENTS

The efficiency of the particle identification cuts are measured using a sample of  $\pi$ -scat monitor triggers taken in "prescale" fashion over most of the run.\* The  $\pi$ -scat trigger, which selects the sort of event depicted in Figure 46a, is defined at Level 0 as the following condition:

$$\tilde{C}_\pi \cdot B4 \cdot E_{target} \cdot IC \cdot \overline{DC} \cdot B_{CT} \cdot (20_{CT} + 21_{CT} + BV + ECP + ECM).$$

\* The  $\pi$ -scat trigger was not operational for the first 10% of our 1989 run.

The first three terms form the beam-pion equivalent of  $KT$ , the kaon-in-target signal defined in Section 3.3. Of the pions that reach the target, we trigger on those that scatter by requiring that they be in coincidence with  $\tilde{C}_\pi$ . Operationally, this is most easily accomplished by *inverting* the delayed coincidence requirement and referencing it to  $\tilde{C}_\pi$ 's leading edge. The remaining trigger criteria, which are similar to that of  $K^+ \rightarrow \pi^+ \nu \bar{\nu}$ , define the allowed region for the charged track.

Offline, we analyze the sample two ways. TD cuts are used to select a clean sample of stopped pions to measure the performance of the kinematic cuts, and vice versa to measure the TD cuts. We thus obtain pion samples that are relatively free of nuclear interactions, the effects of which are determined independently with Monte Carlo, as discussed in Section 5.1.

#### 5.4.1 Kinematic Cuts

Here we measure the acceptance of the range-momentum cuts, which use kinematics to test the relative likelihood of a pion versus a muon mass hypothesis, and the BETASQ cut, which looks for overlaying photons. Although the latter is not a particle identification cut per se, it is tuned for a particular particle type in a particular energy band. Given the choice between  $\pi$ -scat and  $K_{\pi 2}$  events as our source of test pions, the former are better suited for this because they better approximate the part of the  $K^+ \rightarrow \pi^+ \nu \bar{\nu}$  spectrum that we accept.

The  $\pi$ -scat event selection proceeds as follows:

- The full set of TD  $\pi^+ \rightarrow \mu^+ \rightarrow e^+$  cuts are applied to ensure that the pion stopped cleanly, *i.e.*, due to electromagnetic energy loss only.
- The range stack part of the INTIME cut and the PRPAT cut are applied. This avoids over-counting any losses that might be inflicted by accidentals.
- The  $\theta_D$  cut is applied to keep the tracks in the fiducial region of the drift chamber.
- A cut is placed on energy to keep the  $\pi$ -scat tracks in the kinematic region of interest. We require  $80 < E_\pi^{\text{rs}} < 127$  MeV, which is the approximate span for the track energy of  $K^+ \rightarrow \pi^+ \nu \bar{\nu}$  events in the range stack.

The selected events are subjected in turn to the range-momentum and BETASQ cuts. The range-momentum efficiency has a slight kinematic dependence due to worse resolution at high momenta. Therefore, to remove any chance of bias, we weight the efficiency by the shape of the final spectrum as determined by Monte

Carlo simulations for each mode. We find

$$\epsilon_{\text{RNGMOM,RNGMOM2}} = \begin{cases} .881 \pm .005, & K^+ \rightarrow \pi^+ f; \\ .891 \pm .005, & K^+ \rightarrow \pi^+ \nu \bar{\nu}, \end{cases}$$

whereas the unweighted result is  $.897 \pm .005$ ; although the cuts (RNGMOM and RNGMOM2) were applied in two different analysis passes, we assign a single factor for their combined acceptance. Applying the BETASQ cut to the range-momentum survivors with the usual counting method gives

$$\epsilon_{\text{BETASQ}} = .973 \pm .003.$$

All errors are statistical.

#### 5.4.2 Transient Digitizer (TD) Cuts

Nuclear interactions make it difficult to select a totally pure sample of stopped pions using kinematic cuts alone. Since the purity of the test sample strongly influences the result in a counting-method determination of efficiency, we adopt an alternate approach that decouples the measured efficiency from the sample purity. The cuts are treated in two groups. The primary TD cuts consist of PREFIT, FITPI, FITPI2 and TDPION; we denote them by simply the " $\pi^+ \rightarrow \mu^+$ " cuts. Their efficiencies, which is where event selection is a problem, are measured with what we call the "area" method, a method of computing the acceptance that is based on the "area under the curve" in a fit to the pion lifetime. This is described more fully in the next section. As for the secondary cuts, which consist of all remaining TD cuts, sample selection is again straightforward because we have the primary cuts at our disposal. This dispenses with the purity issue and lets us revert to the otherwise more reliable counting method.

##### 5.4.2.1 The Area Method

The "area" method starts with the assumption that the only efficiency loss in tagging pions is due to early decays because the two-pulse signature will have merged into a single pulse. Under this assumption the pion lifetime for successful fits would look like the sketch in Figure 49; at later times the efficiency would be 100% and at early times it would start to fall off. (In fact, we impose a minimum allowed pion decay time because early fits are indistinguishable from stopping muons from say  $K_{\mu 2}$  decays.) The basis of the area method is to extrapolate the observed lifetime

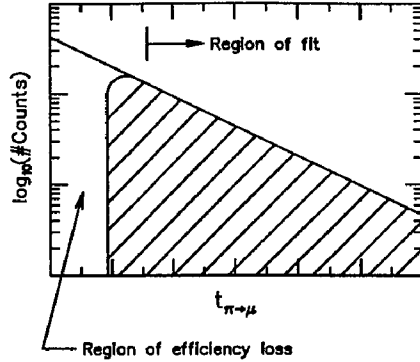


Figure 49. The area method. Assuming the only loss is due to early  $\pi^+ \rightarrow \mu^+$  decays, i.e., merged pulses, the efficiency is the ratio of the area of the hatched region to the area under the whole curve.

spectrum back to early times and thereby infer the loss of efficiency there, the *area* under the lifetime curve where no pions are tagged. In essence, we exploit the quantifiable and predictable pattern of  $\pi^+ \rightarrow \mu^+$  “survivors” — that they obey a  $\pi^+$  decay curve — to select their own test sample.

The actual method, which is outlined in the flowchart of Figure 50, is more complicated than suggested above because there are reasons other than early decays for legitimate pions to fail the analysis. An example is overflows in the digitizing of pulses, as discussed in Section 3.7. Therefore, we measure and apply a correction that amounts to about 20%. The first-order measurement is illustrated in the left branch of the figure, the corrections, on the right; both are described in detail below.

We start by selecting a sample of  $\pi$ -scat triggers with the analysis cuts listed below (the first two “bubbles” in the chart):

- The range stack part of the INTIME cut and the PRPAT cut are applied. This avoids over-counting any losses already incurred by the photon veto cuts.
- The Level 1 hextant cut is applied. (It is needed to establish a unique hardware stopping-counter address for PREFIT and TDPION, as discussed in Sections 3.6 and 4.3.4.)
- We require agreement between the hardware and software address for the stopping counter. (Disagreement is measured as a separate loss in Section 5.5.2.)
- A stringent range-momentum cut is used to select pions. We require  $L_\pi > .1$  and  $\log_{10}(L_\pi/L_\mu) > 1$  (see Figure 45).
- We apply the  $\theta_D$  cut to ensure the integrity of the kinematic measurements,

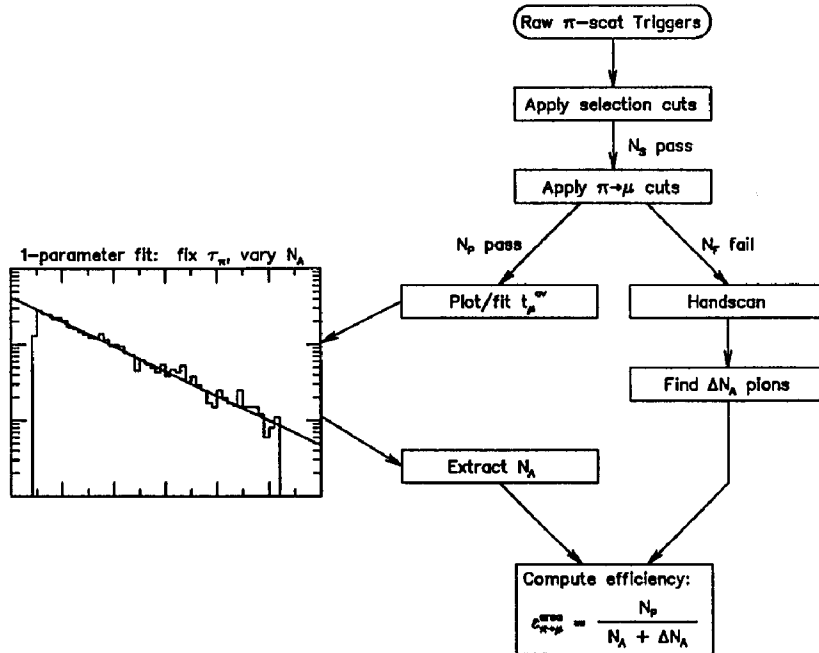


Figure 50. The “area” method of measuring the  $\pi^+ \rightarrow \mu^+$  tagging efficiency. The variables are discussed in the text.

The selected events are subjected to the  $\pi^+ \rightarrow \mu^+$  cuts, and  $t_\mu^{\text{av}}$  is plotted and fit to an exponential decay curve for the surviving events. It was this particular spectrum that was shown in Figure 36, when the cuts themselves were described. We note again that the 2-parameter fit yielded a pion lifetime of  $\tau_\pi = 26.7 \pm .6$  nsec with  $\chi^2/d.o.f. = 1.174$ , compared with an accepted value of 26.03 nsec. We take this as evidence for the purity of the test sample, and we use the number of events that pass the cuts for the numerator in the efficiency calculation.

To determine the denominator, we proceed with the two branches in the chart. Again, the first-order measurement is made in the left branch of the diagram by assuming that only early decays fail the cuts. We deduce the expected number of survivors for *perfect* efficiency by measuring the area under the fitted curve for *all* times. (To eliminate any bias introduced by the measured lifetime we have refit the data with the lifetime fixed at the true value and varied only the normalization.)

The right branch illustrates a handscan correction that accounts for other losses by looking at the *failed* events and seeing how many should have passed the cuts. Since this involves looking for double-pulses by eye (those that were missed by the trigger and offline fitter), we only take those that have  $t_\mu^{\text{av}} > \tau_\pi = 26$  nsec.

Therefore, since we do not survey what might be legitimate pions during the first lifetime, which are as likely as late decays to have failed because of overflows, etc., we scale the number of events that pass the handscan by Euler's number,  $e$ . Also, we only handscan approximately one event in twenty so the number of passing events must be scaled for this, as well.

The total number of potentially-detectable pions is the sum of the fitted normalization and the handscan correction, where the latter is given by

$$\Delta N_A = N_{PH} \times e \times \frac{N_F}{N_H},$$

as discussed in the previous paragraph. Again, the terms are summarized in Table 19, along with their measured values; note also that  $N_F/N_H$  corrects for the fraction of events that were *not* handscanned. The efficiency based on the area method is given by

$$\epsilon_{\pi^+ \rightarrow \mu^+}^{area} = \frac{N_P}{N_A + \Delta N_A}$$

where  $N_P$  is the number of events passing the cuts and  $N_A$  is the fitted normalization. Substituting the measured values from the table gives

$$\epsilon_{\pi^+ \rightarrow \mu^+}^{area} = .564.$$

An error is not yet supplied because one final correction remains.

Quantity	Description	Value
$N_S$	Number selected in original sample	8452
$N_P$	Total counts in spectrum	3933
$N_A$	Normalization, 1-parameter fit	$5664 \pm 96$
$N_F$	Number failing $\pi^+ \rightarrow \mu^+$ cuts	4519
$N_H$	Number of failed events handscanned	225
$N_{PH}$	Number passing handscan criteria	24

Table 19. Bookkeeping for the area method. The error shown in  $N_A$  is the statistical error in the fitted normalization.

A loss we have not yet accounted for is decay muons that leave the stopping counter before depositing enough energy for a detectable second pulse. We base a simple geometrical correction on the thickness of the range stack counters and the kinematics of the muon from  $\pi^+$  decay at rest. The TD cuts must see at least

approximately 2 MeV of the original 4.2 MeV of energy. Equivalently, we are able to detect muons that have a range in the stopping counter greater than approximately

$$d = R_{\mu}(4.2) - R_{\mu}(2) = 1.55 - .18 = 1.37 \text{ mm},$$

where  $R_{\mu}(E)$  is the range in scintillator of a muon with kinetic energy  $E$ . Since this loss is itself a small correction and is dominated by muons that escape through the large faces of the slab-like counters, we ignore the effects of muons leaving through the sides of the counters. Thus, we compute the observable fraction of muons as

$$\epsilon_{\pi^+ \rightarrow \mu^+}^{escape} = \frac{d}{2t} = \frac{1.37}{2 \times 19.5} = .965,$$

where  $t = 19.5$  is the thickness of the counter in millimeters. Therefore, the net  $\pi^+ \rightarrow \mu^+$  efficiency is the product of two terms:

$$\epsilon_{\pi^+ \rightarrow \mu^+} = \epsilon_{\pi^+ \rightarrow \mu^+}^{area} \times \epsilon_{\pi^+ \rightarrow \mu^+}^{escape} = .564 \times .965 = .54 \pm .05.$$

A statistical error derived from the fitted normalization and the handscan procedure amounts to .02. However, studies made with a variation on the counting method suggest a larger uncertainty, as we have indicated.

The  $K_{\pi 2}$  branching ratio measurement, which is described in Section 5.7.2, does not use either the PREFIT or TDPION cuts because these in turn depend on the hardware stopping assignment. Since this information is based on the photon veto hexant bits of Level 1, it is not generally valid for events with photons. Therefore, we repeat the area method to get an efficiency for the FITPI and FITPI2 cuts alone, as opposed to the full set of primary  $\pi^+ \rightarrow \mu^+$  cuts. We find:

$$\epsilon_{FITPI, FITPI2} = .60 \pm .05.$$

#### 5.4.2.2 TD Cuts: the Counting Method

The events that survive the  $\pi^+ \rightarrow \mu^+$  analysis above are a relatively pure sample of pions so we use them to measure the efficiency of the secondary cuts by reverting to the usual counting method. The cuts and their efficiencies are listed in Table 20; a discussion of the losses follows.

Cut	# Passing	Efficiency
Selection	3933	—
TPIDIF	3924	.9977 ± .0007
LOELAST	3908	.996 ± .001
EMUAV	3831	.980 ± .002
TDFLUC	3673	.959 ± .003
$\mu^+ \rightarrow e^+$	3102	.845 ± .006
PROD20	3073	.991 ± .002
TMUPROD	3057	.995 ± .001
ELVETO, ELVETO2	2837	.928 ± .005
RSHEX	2835	.9993 ± .0005
TDFOOLERY	2828	.9975 ± .0009

Table 20. Efficiency of the secondary TD cuts. Errors are statistical.

About half the inefficiency of the  $\mu^+ \rightarrow e^+$  cuts is attributable to the muon lifetime, since we only detect electrons in the range  $20 < t_{\mu^+ \rightarrow e^+} < 6100$  nsec. The remainder of the loss is due to low energy electrons, or those that fail to deposit at least some energy local to the stopping counter. Losses to TPIDIF, the ELVETO cuts, TDFOOLERY and RSHEX are due to accidentals, as can easily be seen from the descriptions of the cuts given in Chapter 4. Inefficiencies of the remaining cuts are due simply to tails in the various distributions, the imperfect separation between signal and background.

### 5.5 $K_{\pi 2}$ MEASUREMENTS

The acceptance of the Level 1.5 trigger, which rejected  $K_{\mu 2}$  events using an online determination of the track energy, is measured with a sample of  $K_{\pi 2}$  decays selected from monitor triggers accumulated over the full course of the run. Since  $K_{\pi 2}$  decays are a convenient source of monochromatic charged pions, we can use them to interpolate the effects of the trigger on pions of other momenta, those of the rare modes. Although we generally rely upon the Monte Carlo for measurements of our kinematic acceptance,  $K_{\pi 2}$  decays are of particular importance to the energy trigger because it is difficult to simulate all that affects the online measurement. Examples are variations in the online calibration and a higher susceptibility to accidentals that befall the less intelligent online algorithm of summing track energy. In the next section, we describe how  $K_{\pi 2}$  data are used to mimic the rare modes in regards to the application of the energy cut.

The trigger that selects  $K_{\pi 2}$  decays is defined at Level 0 as

$$KT \cdot (T \cdot A) \cdot B_{CT} \cdot \overline{(19_{CT} + 20_{CT} + 21_{CT})},$$

where the terms are the trigger bits described in Chapter 3. In addition to  $K_{\pi 2}$  decays, this (fairly loose) trigger also accepts a number of  $K_{\mu 2}$  decays, those at large dip angle that stop in a layer shallow compared to most  $K_{\mu 2}$  decays; indeed, these are similar to the unwanted  $K_{\mu 2}$  events that satisfy the  $K^+ \rightarrow \pi^+ \nu \bar{\nu}$  trigger at Level 0, as we saw in Figure 26. Therefore, the data, which consist of both modes and are collectively referred to as “ $K_{\pi 2}$  triggers,” must be carefully selected to get a test sample for the online energy measurement.

We also use data from the  $K_{\pi 2}$  trigger to measure the loss of efficiency caused by errors in the hardware stopping counter assignment used for the TDPION and PREFIT analyses. Since the trigger is loose and accepts both  $K_{\pi 2}$  and  $K_{\mu 2}$  decays, it provides us with a test sample of kaon decays with good coverage over the full span of stopping layers accessible to  $K^+ \rightarrow \pi^+ \nu \bar{\nu}$  decays. Since the accidental hits affect the hardware address and their rate is somewhat layer dependent, it is important for the sample to have proper layer coverage. This measurement is taken up following the discussion of the energy trigger.

### 5.5.1 The Level 1.5 Energy Trigger

The energy trigger used for online rejection of  $K_{\mu 2}$  decays has two requirements, as was illustrated in Figure 29. The acceptance of the first, that there be one-and-only-one  $T \cdot A$ , was accounted for as an accidental loss measured with  $K_{\mu 2}$  decays in Section 5.3.2. Here, we measure the acceptance of the second, the efficiency of the kinematic cut once a valid online energy determination has been made. To avoid over-counting losses that are possibly correlated with those of the energy part of the offline (Box) cut, we define the efficiency of the trigger as the fraction of events accepted by the online cut following the application of the offline. The remaining details of the measurement lie in where to place the cuts on a  $K_{\pi 2}$  sample to produce effects equivalent to those placed on the rare modes.

We start by selecting a clean sample of  $K_{\pi 2}$  monitor triggers with cuts from the standard analysis program: TD and range-momentum cuts select stopped pions; beam and timing cuts select properly reconstructed decays of stopped kaons; fiducial cuts prevent biases in the kinematic measurements; and photon cuts ensure that there are two clusters in the barrel with energy roughly equal to the  $\pi^0$  energy and that there is no extra activity elsewhere, especially in the range stack. Application of the last cut, the range stack part of “INTIME,” avoids over-counting losses that

are due to accidental contributions to the track energy, losses that have already been counted in the photon veto acceptance factors.

The scatterplot in Figure 51 shows the correlation between online versus offline energy measurements for the selected events. The online energy  $E_{1.5}$  is the actual value that is computed and recorded for all events, regardless of trigger type (the cut itself is imposed only  $K^+ \rightarrow \pi^+ \nu \bar{\nu}$  triggers). The offline energy  $E_{total}$  is computed in the usual way, as discussed in Section 4.3.6.

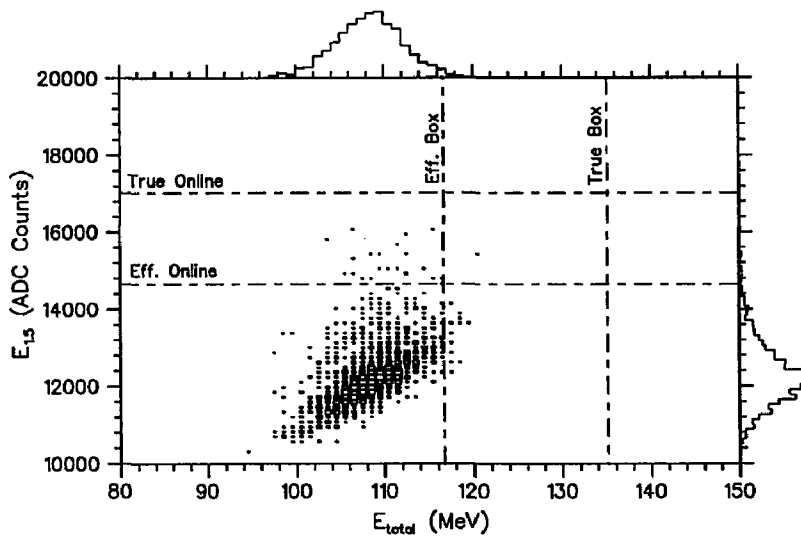


Figure 51. Level 1.5 track energy versus the offline result, for selected  $K_{\pi 2}$  decays. The vertical lines indicate the true and effective kinematic cuts for the energy component of the Box cut. Likewise, the horizontal lines indicate the online cut.

We compute the efficiency for  $K^+ \rightarrow \pi^+ f$  by shifting the Box and online cuts down by 18.5 MeV (the difference between the  $K_{\pi 2}$  and  $K^+ \rightarrow \pi^+ f$  peaks) and applying them to the  $K_{\pi 2}$  sample, as indicated by the dashed lines. To determine the magnitude of the shift in ADC counts, we use the nominal online calibration of 128 counts/MeV, a product of the following factors:

$$(\text{RS calib. of } 16 \text{ counts/MeV/end}) \times (2 \text{ ends}) \times 4.$$

The last term is an arbitrary scale change in the hardware that shifts the binary data by 2 bits. Since the actual online cut is placed at 17024 counts, or

133 MeV  $\times$  128 counts/MeV, the effective cut for  $K_{\pi 2}$  decays is

$$17024 - 18.5 \times 128 = 14656 \text{ ADC counts.}$$

The effective Box cut is simply

$$135 - 18.5 = 116.5 \text{ MeV.}$$

As discussed above, we define the online acceptance after the Box cut has been applied:

$$\begin{aligned} \epsilon &= \frac{(\# \text{in spectrum}) - (\# \text{failing Box}) - (\# \text{failing 1.5})}{(\# \text{in spectrum}) - (\# \text{failing Box})} \\ &= \frac{1368 - 24 - 24}{1368 - 24} \\ &= .982 \pm .004_{(stat.)}. \end{aligned}$$

We make two alternative measurements in order to gauge a systematic error because if the assumed calibration of 128 counts/MeV is incorrect then we have not moved the online cut by the right amount. First, we use the observed peak value of the online  $K_{\pi 2}$  energy to empirically determine the calibration. The expected value for the peak energy is 110.1 MeV.\* Comparing this with the measured value of 12224 counts suggests that the calibration is more like 111 counts/MeV, which in turn leads to an efficiency of  $.989 \pm .003_{(stat.)}$ .

Another estimate is made by using the energy resolution as a guide to placing the cuts, since the acceptance is mainly sensitive to the "tails." We take  $\sigma = .36/\sqrt{E}$ †, reposition the cuts to points that are equivalent  $\sigma$  above the  $K_{\pi 2}$  peak, and measure an efficiency of  $.982 \pm .004_{(stat.)}$ . Averaging the three results and inferring an error from the spread gives

$$\epsilon_{L1.5 E}(K^+ \rightarrow \pi^+ f) = .98 \pm .01.$$

For  $K^+ \rightarrow \pi^+ \nu \bar{\nu}$ , we use the first method to trace out the three-body spectrum by shifting the cuts in 1 MeV steps. This gives the efficiency for each energy bin, which we then weight with the shape of the final  $K^+ \rightarrow \pi^+ \nu \bar{\nu}$  spectrum derived

\* To get this we start with the true energy of 108.5 MeV, add 3 MeV for the decay muon and subtract 1.4 MeV for a typical I-counter energy; the latter is not included in the online sum.

† A reasonable fit to  $1/\sqrt{E}$  behavior is obtained with the kinematic measurements listed in Table 12; E and  $\sigma$  are in MeV.

from Monte Carlo and subsequent KOFIA analysis. Since much of the spectrum is below the endpoint of 127 MeV and most of the Level 1.5 losses occur above it, the effect is a higher efficiency for  $K^+ \rightarrow \pi^+ \nu \bar{\nu}$  than for  $K^+ \rightarrow \pi^+ f$ . We find

$$\varepsilon_{L1.5E}(K^+ \rightarrow \pi^+ \nu \bar{\nu}) = .9992 \pm .0008$$

where the error is due to the combined statistical error in the bin-wise efficiency and the shape of the simulated  $K^+ \rightarrow \pi^+ \nu \bar{\nu}$  spectrum; the systematic error in the  $K^+ \rightarrow \pi^+ f$  acceptance is dominated by effects at the endpoint and turns out to be negligible once the weighting factor is applied.

### 5.5.2 The Hardware Stopping Counter

A disagreement between the hardware and software stopping counter assignments results in a loss of efficiency because this means that the  $\pi^+ \rightarrow \mu^+$  cuts were applied over two different counters. Since a stopped pion could not possibly satisfy the  $\pi^+ \rightarrow \mu^+$  cuts in more than a single counter, an inefficiency results.  $ST_{hex}$  refers to the fraction of the time the two assignments *agree*.

To measure the efficiency we start with a prescaled sample of  $K_{\pi 2}$  triggers that span the full run. We then select a subset of clean single-track events that satisfy basic fiducial cuts, stop in layers 11–18, and have no photons in the range stack. The last requirement includes both the range stack part of the offline veto and the Level 1 Hextant cut. As noted earlier, the selected sample contains both  $K_{\mu 2}$  and  $K_{\pi 2}$  events and is thus well distributed over the layers of the stopping region. The efficiency is the fraction of the selected events that show agreement between hardware and software in both layer and hextant. We find:

$$\varepsilon_{ST_{hex}} = .958 \pm .002,$$

where the error is statistical.

Losses occur when a track crosses a hextant boundary just before the particle comes to rest, such that the energy deposited in the last hextant is below the threshold required to assert the corresponding (and correct) hextant bit. Recall that the primary function of the hextant bits is to veto photons in the range stack at Level 1. Therefore, although reducing the threshold from its  $\sim 10$  MeV setting would solve the stopping-address problem, it would also increase the susceptibility to accidental losses in the veto. Aside from the hextant bit threshold, inefficiencies are caused by accidental hits that land near the stopping counter.

Now we investigate a related inefficiency: the fraction of the time that the stopping counter comes out altogether *wrong*, both in hardware and software. A separate study shows that this occurs when the decay muon leaves the stopping counter in the outward radial direction and deposits enough energy in the next layer to artificially extend the track. This represents a loss of efficiency because although a  $\pi^+ \rightarrow \mu^+$  decay has taken place, it escapes detection because we search the wrong counter. It turns out that this loss is almost completely correlated with the rate at which muons leave too small a second pulse in the true stopping counter to be detected by the TD  $\pi^+ \rightarrow \mu^+$  cuts, a loss that we already accounted for by the geometrical correction described in Section 5.4.2.1. Finally, we note that the wrong-track rate caused by accidentals was found to be negligible.

## 5.6 MONTE CARLO MEASUREMENTS

Certain acceptance factors do not lend themselves to measurement with monitor triggers so we turn to Monte Carlo simulation. The E787 Monte Carlo program, UMC, was originally written to establish the design of the detector and to estimate the capabilities of the trigger. Since then, we have added improvements derived from actual detector performance to further enhance its realism.

UMC is used as a stand-alone program to simulate kaon decays in the E787 detector in which the user can extract, tally or plot quantities of interest. It also generates "fake" events in a format that is suitable for analysis by KOFIA, our standard analysis program. Use of the two programs in concert allows us to follow every detail of an event starting from a simulation of the trigger and on through nearly the entire analysis chain.

In the next section I describe the basic features of UMC, the event flow for generating kaon decays, and the simulation of the trigger. The section that follows describes efficiency measurements of the trigger, the fiducial and kinematic Box cuts, and finally the effects alluded to in Section 5.1, those that are difficult to properly isolate in data. We refer to the last effects as "line items" since they cause losses to several cuts: in order to avoid over-counting they are accounted for independent of the affected cuts and are therefore given a separate "line" in the table of acceptance factors. The example given earlier was nuclear interactions, which can alter the pion's kinematics and its identity. The other line items are pions that decay in flight and pions that stop in a detector medium other than scintillator (for example, a range stack chamber), both of which cause the range and energy to be mismeasured. In addition, the latter tends to "hide" the  $\pi^+ \rightarrow \mu^+$  pulse (recall the muon is short range), while the former precludes the double-pulse signature altogether.

## 5.6.1 The Workings of UMC

UMC starts each event with a kaon and a predetermined decay mode. Particles are propagated through the various media of the E787 detector and they lose energy via a number of different physical processes. Unstable particles decay according to their characteristic lifetime, and decay and nuclear reaction products are entered onto the “stack” of particles that began with the original kaon. The event is completed when all particles have either stopped or decayed, and the stack is thus empty.

The main energy loss process is the electromagnetic interaction, with an emphasis on the transport of low-energy charged particles. In particular, the effects of multiple-scattering are treated in detail, as this bears directly on measurements of both momentum and range, especially regarding the tails of the distributions. Electromagnetic showers of photons and electrons are simulated with the standard program EGS [29]. Nuclear interactions of the  $\pi^+$  are also simulated, using cross-sections based on experimental data [30] and allowing for elastic, inelastic and pseudo-elastic collisions with nuclei.

As an event develops, energy deposited in the detector is recorded in arrays according to region, medium and time. Also, the “fate” of each particle is noted: that it decayed in flight, underwent a nuclear interaction, or simply came to rest. Simulated trigger criteria are imposed in order to measure their own losses and to decide which events are to be written out for further analysis. Energy in the arrays is converted into ADC- and TDC-like data, but TD pulse information is not generated since it is better studied from actual data.

Summary of UMC Runs		
Mode	$\pi^+$ N.I./D.I.F.	To Measure
$K_{\pi 2}$	enabled	Kinematic scale; acceptance for BR
$K_{\mu 2}$	—	Kinematic scale; acceptance for BR
$K^+ \rightarrow \pi^+ \nu \bar{\nu}$	disabled	Acceptance of “perfect” pions
$K^+ \rightarrow \pi^+ f$	disabled	Acceptance of “perfect” pions
$K^+ \rightarrow \pi^+ \nu \bar{\nu}$	enabled	Relative acceptance of “real” pions
$K^+ \rightarrow \pi^+ f$	enabled	Relative acceptance of “real” pions

Table 21. The Monte Carlo is run in six configurations. Events passing the trigger are written out for further analysis.

For  $K_{\pi 2}$  and  $K_{\mu 2}$  decays we simulate the Level 0 trigger, and for the rare modes Level 1, as well.  $K_{\pi 2}$  and  $K_{\mu 2}$  events are generated to determine the trigger and

analysis acceptance for their branching ratio measurements in Section 5.7, and to study the kinematic scales that were summarized in Table 12. The rare modes are each run twice: first, to determine the geometrical and kinematic acceptance free from the effects of pion nuclear interactions and decays in flight, and then, to measure the loss due to these effects alone. The runs are summarized in Table 21, which shows the predetermined characteristics of the  $\pi^+$ .

We now describe the event flow and trigger using a  $K^+ \rightarrow \pi^+ \nu \bar{\nu}$  decay as an example:

- A kaon starts in the target with a stopping position selected from a three-dimensional distribution derived from data. Realism is sought here because the angular acceptance of the detector is influenced by the point of origin of the kaon decay products.
- Rather than start the kaon at rest, it is displaced upstream and given just enough kinetic energy to reach the position selected above. This allows the kaon itself to leave a signal in the target, yet preserves the true stopping distribution.
- The kaon is required to come to rest before decaying. (The UMC events are compared only to stopped-kaon data selected with the delayed coincidence cut.)
- The decay pion is tracked with nuclear interactions disabled and it is forced to decay at rest (or as noted in Table 21).
- The decay muon is tracked but does not itself decay. (Since the TD data are not simulated, our  $\mu^+ \rightarrow e^+$  analysis is not executed on UMC data; like the  $\pi^+ \rightarrow \mu^+$  analysis it is studied directly from data. Therefore, we eliminate the electron altogether by disabling the muon decay.)
- After tracking is complete and all particles have stopped and/or decayed, the Level 0 trigger criteria are applied to the data stored in the energy arrays. In analogy to the hardware described in Chapter 3, pulse height sums are made in the barrel and endcaps to establish veto signals and individual counters throughout the detector are discriminated by applying thresholds to their energies. Discriminated range stack signals are used to establish the  $T \cdot A$  and  $X_{CT}$  bits.
- If the event passes Level 0, we apply the refined range trigger of Level 1. The trigger logic is applied in much the same way as in the hardware illustrated in Figure 28. The digitization of the range stack  $z$ -position and target range are simulated with distributions from actual data.

- The range stack hextant veto is not applied. A separate Monte Carlo study shows that it has no intrinsic loss of acceptance, only that due to accidentals.
- We do not simulate the Level 1 hextant veto or the triggers used at Level 1.5 or 2: their acceptance factors are all measured from data.
- Events passing the simulated Level 1 trigger are recorded for further analysis.

The recorded events are subjected to the analysis program applied to data and acceptance factors are extracted from the cut statistics in counting-method fashion. Like the higher level triggers, we safely omit the beam and TD cuts because their acceptance factors are measured directly from data. Also, since we are dealing with preselected (hence, ideal) Monte Carlo events, these cuts are not need for further sample preparation as when working with real data.

### 5.6.2 UMC Acceptance Factors

The efficiencies of the trigger criteria are determined by statistics recorded within UMC for the samples with the  $\pi^+$  disabled. Factors are computed separately for  $K^+ \rightarrow \pi^+ f$  and  $K^+ \rightarrow \pi^+ \nu \bar{\nu}$  runs, as shown in Table 22. The loss of  $K^+ \rightarrow \pi^+ f$  events is primarily due to the solid angle acceptance of the  $T \cdot A$  requirement.  $T \cdot A$  losses are slightly higher in  $K^+ \rightarrow \pi^+ \nu \bar{\nu}$  because, in addition to geometry, low momentum tracks emerging from the target “curl up” in the drift chamber and fail to reach the range stack. The  $B_{CT}$  and  $11_{CT}$  requirements cut further into the lower part of the three-body spectrum. Since all of these events would fail the Box cut anyway, it is of no consequence that they are rejected by the trigger. The Level 1 MLU criterion has a lower acceptance for  $K^+ \rightarrow \pi^+ f$  because, like the energy trigger, it rejects events at the high end of the spectrum.

Factor	$K^+ \rightarrow \pi^+ f$	$K^+ \rightarrow \pi^+ \nu \bar{\nu}$
Level 0 $T \cdot A$	$.459 \pm .004$	$.417 \pm .003$
Level 0 $\mu$ -veto and $B_{CT}$	$.9987 \pm .0005$	$.825 \pm .003$
Level 1 $11_{CT}$	$.961 \pm .002$	$.507 \pm .005$
Level 1 MLU	$.927 \pm .004$	$.979 \pm .002$

Table 22. Trigger efficiencies from UMC.

The efficiencies of the fiducial and box cuts are determined by applying the analysis cuts to the events surviving the above trigger criteria. The factors for the two decay modes are listed in Table 23. Corrections to the kinematic quantities,

which were discussed in Section 4.3.6, are made prior to the Box cut. The  $z_{14}$  cuts, which suppress  $K_{\mu 2}$  decays that are kinematically degraded by range stack chamber material, have slightly higher losses for  $K^+ \rightarrow \pi^+ f$  because a larger fraction of their pions reach the outer chamber just beyond layer 14.

Factor	$K^+ \rightarrow \pi^+ f$	$K^+ \rightarrow \pi^+ \nu \bar{\nu}$
$z_{14}, z'_{14}$	$.963 \pm .003$	$.985 \pm .002$
$\theta_D, \theta_D^n$	$.970 \pm .002$	$.970 \pm .002$
BOX	$.962 \pm .003$	$.417 \pm .017$

Table 23. Efficiency of offline fiducial and kinematic cuts based on UMC.

Of the three "line items," we treat pion nuclear interactions and decays in flight together because they are loosely correlated: the probability that a pion interacts depends in part on how much material it has traversed—those that decay in flight traverse less. A separate acceptance factor is measured for the fraction of pions that stop in scintillator; those that stop in non-scintillating media represent an inefficiency, again, because of kinematic mismeasurement and the loss of the  $\pi^+ \rightarrow \mu^+$  signature.

To measure the combined acceptance of the first two items we compare the UMC samples that have the effects "on" and "off." Since these effects are coupled to the particle's kinematics, we apply the complete trigger and analysis chain including the Box cut, so that our measurement properly characterizes the final spectrum. The comparison of the two cases, which is made by taking the double ratio below, yields the efficiency for requiring that the pion did *not* undergo a nuclear interaction or decay in flight:

$$\varepsilon_{\text{n.i.,d.i.f.}} = \frac{(N_{\text{surviving}}/N_{\text{generated}})_{\text{on}}}{(N_{\text{surviving}}/N_{\text{generated}})_{\text{off}}},$$

where  $N_{\text{surviving}}$  is the number of events surviving the analysis cuts and  $N_{\text{generated}}$  is the number of stopped kaons in the UMC sample. For the case of the numerator, the requirement of a well-behaved pion is imposed by checking the "fate" information recorded for each event. We find that

$$\varepsilon_{\text{n.i.,d.i.f.}} = \begin{cases} .48 \pm .01, & K^+ \rightarrow \pi^+ f; \\ .53 \pm .02, & K^+ \rightarrow \pi^+ \nu \bar{\nu}. \end{cases}$$

The losses for the first process are higher because the decay pion must traverse more material before it comes to rest, and because the nuclear cross-sections increase with

increasing momentum in this kinematic band (the rising edge of a  $\Delta$ -resonance). We note again that our simulation includes cross-sections for elastic, inelastic, and pseudo-elastic processes. Experimental uncertainties in these quantities are as large 5–10%, and are not included in the above errors, which reflect only statistics.

We determine the fraction of pions that stop in scintillator by checking the stopping medium which was recorded by UMC for each event. As our test sample, we use the UMC events that have nuclear interactions and decays in flight disabled, and have satisfied all subsequent analysis cuts. We find:

$$\epsilon_{\text{scint.}} = \begin{cases} .979 \pm .002, & K^+ \rightarrow \pi^+ f; \\ .985 \pm .002, & K^+ \rightarrow \pi^+ \nu \bar{\nu}. \end{cases}$$

As with the  $z_{14}$  cuts, we observe slightly larger losses for  $K^+ \rightarrow \pi^+ f$ , again because their decay pions are more likely to reach the outer range stack chamber, the source of the non-scintillating material.

## 5.7 NORMALIZATION

Now that we have all of the acceptance factors, we complete our measurement of the effective number of observed kaons by determining the flux. As a cross check, we also measure the  $K_{\mu 2}$  and  $K_{\pi 2}$  branching ratios using analysis methods similar to those applied to the rare decay data. In particular, the  $K_{\mu 2}$  branching ratio depends mainly on measurements of the flux and solid angle acceptance, while the  $K_{\pi 2}$  depends also on “pion issues,” namely, particle identification, nuclear interactions and decays in flight. We start with a brief description of the flux measurement.

### 5.7.1 The Flux

We define the flux, which is denoted by  $K_{\text{stop}}$ , as the total number of kaons that stopped in the target during the time that the detector was “live,” or ready to accept a trigger. The actual signal that is counted when data are being taken is  $KT^*$ , however, it does not bear a one-to-one correspondence to  $K_{\text{stop}}$  because of a number of systematic differences in their definitions. For example, kaons that satisfy the K-Čerenkov requirement of  $KT$  might then interact in the degrader, with their subsequent reaction products striking  $B4$  and the target. Alternatively, a beam

---

\* Recall that  $KT \equiv \check{C}_K \cdot B4 \cdot E_{\text{target}}$  is the kaon-in-target signal defined in Chapter 3.

pion that reaches the target after accidentally firing  $\tilde{C}_K$  can also give a spurious  $KT$  signal. As these scenarios suggest, a true  $K_{\text{stop}}$  signal is difficult to define online so we rely on  $KT$ -counting and offline corrections thereof. The correction factor  $f_S$ , which consists of six independently measured parts [31], converts  $KT$  to  $K_{\text{stop}}$  with the result:

$$\begin{aligned} K_{\text{stop}} &\equiv f_S \times KT_{\text{live}} \\ &= (.642 \pm .008) \times 1.75 \times 10^{11} = (1.124 \pm .014) \times 10^{11} \text{ counts,} \end{aligned}$$

where  $KT_{\text{live}}$  is the logical "AND" of  $KT$  and the detector live time gate. In the second line, we have substituted the measured value of  $f_S$  including a combined statistical and systematic uncertainty, and the total  $KT_{\text{live}}$  counts for the data sample analyzed in Chapter 4. The result is our total kaon flux for the 1989 run.

### 5.7.2 The $K_{\mu 2}$ Branching Ratio

We measure the  $K_{\mu 2}$  branching ratio using the prescaled monitor sample taken along with the physics data over the course of the run. Selected cuts from the  $K^+ \rightarrow \pi^+ \nu \bar{\nu}$  analysis, which are summarized in Table 24, are applied to the monitors to produce a clean muon spectrum. We use a plot of the muon range to extract the number of candidate events, as shown in figure 52.

The flux is deduced from the  $KT_{\text{live}}$  total for the runs analyzed. To express it in terms of  $K_{\text{stop}}$ , we divide by the appropriate prescale factor and multiply by  $f_S$ . To measure the acceptance, we begin with Monte Carlo. A known number of UMC events are generated and the analysis cuts listed in the table are applied (beam and delayed coincidence cuts excepted). The fraction of original kaon decays that survive the trigger and analysis is the acceptance. Separate corrections are applied for photon and beam accidentals, and the delayed coincidence cuts, since they are applied to the data but not the Monte Carlo events. Also, we factor out the setup efficiencies and replace them with values measured from data because known effects are not simulated in the Monte Carlo. These are the broken drift chamber wire mentioned in Section 5.3.1 and reconstruction failures due to accidental hits.

$K_{\mu 2}$ Analysis Summary			
Cut	Events In	Events Cut	Rejection
Level 0 Dly'd Coin.	93108	26496	1.398
TG Setup	66612	1176	1.018
DC/RS Setup	65436	11280	1.208
Offline Dly'd Coin.	54156	4594	1.093
$\bar{\gamma}_w$	49562	8923	1.220
Level 1 Hexant	40639	736	1.018
$\bar{C}_\pi^w$	39903	739	1.019
$B4_{fit}$	39164	1064	1.028
$B4_{dE/dx}$	38100	393	1.010
$z_{14}, z'_{14}$	37707	262	1.007
$\theta_D$	37445	327	1.009
$D_{tgt}, D'_{tgt}$	37118	624	1.017
$\bar{\gamma}_{tgt}, \gamma'_{tgt}$	36494	1645	1.047
$10 < R_{total} < 70$ cm	34849	258	1.007
Total	34591	—	—

Table 24. Summary of applied  $K_{\mu 2}$  cuts and rejection factors.

We calculate the branching ratio for  $K^+ \rightarrow \mu^+ \nu$  using the expression:

$$\begin{aligned}
 BR(K^+ \rightarrow \mu^+ \nu) &= \frac{\#K_{\mu 2} \text{ events}}{\#K_{\text{stop}}} \times \frac{1}{A_{MC}} \times \frac{A_{DC/RS}^{MC}}{A_{DC/RS}^{data}} \times \frac{A_{TG}^{MC}}{A_{TG}^{data}} \\
 &\quad \times \frac{1}{A_{\bar{\gamma}}} \times \frac{1}{A_{DC}} \times \frac{1}{A_{BEAM}} \\
 &= \frac{34591}{(285721 \pm 3560)} \times \frac{1}{(.361 \pm .004)} \times \frac{(.982 \pm .002)}{(.853 \pm .003)} \\
 &\quad \times \frac{(.9962 \pm .0008)}{(.982 \pm .001)} \times \frac{1}{(.842 \pm .004)} \\
 &\quad \times \frac{1}{(.815 \pm .005)} \times \frac{1}{(.956 \pm .002)} \\
 &= .597 \pm .003_{(stat.)} \pm .009_{(acc.)}, \quad (\text{true value} = .6351).
 \end{aligned}$$

where  $A_{MC}$  is the Monte Carlo acceptance,  $A_{DC/RS}^{MC}$  and  $A_{TG}^{MC}$  are reconstruction efficiencies measured for the Monte Carlo sample using the same method as for

data,  $A_{DC/RS}^{data}$  and  $A_{TG}^{data}$  are reconstruction efficiencies measured for data,  $A_{DC}$  is the combined efficiency of the online and offline delayed coincidence cuts, and  $A_{\bar{\gamma}}$  and  $A_{BEAM}$  are corrections for losses due to accidental vetoes. The first error in the bottom line is the statistical error in the number of events in the data sample. The second is the error in the acceptance derived from the combined errors in the expression above it, which are themselves mostly statistical; exceptions are systematic errors in the setup losses and the flux, the latter carried over from  $f_S$ .

Our measured value is 6% below the accepted value. Before drawing a conclusion on the nature of the discrepancy and what to do about it, we proceed with the related measurement of the  $K_{\pi 2}$  branching.

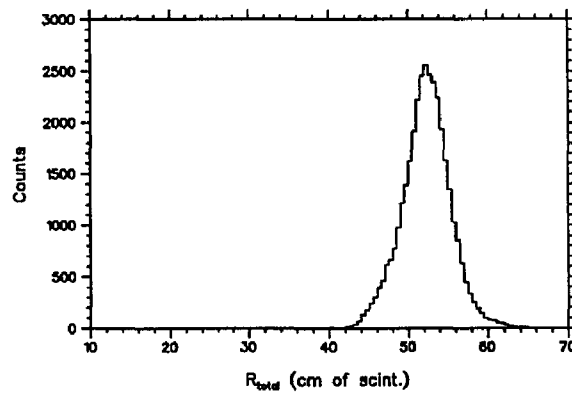


Figure 52.  $K_{\mu 2}$  Range. Events from monitor data that survive the analysis cuts. The applied range cut corresponds to the horizontal limits of the histogram.

### 5.7.3 The $K_{\pi 2}$ Branching Ratio

We measure the  $K_{\pi 2}$  branching ratio with the cuts listed in Table 25 and a monitor sample spanning the full run. After the analysis cuts, we extract the number of  $K_{\pi 2}$  candidates with a range cut centered about the peak value, as shown in Figure 53; a similar cut is applied to the UMC sample.

As in the previous section, the acceptance is calculated by starting with the Monte Carlo and applying a suitable set of corrections. In addition to beam and timing, we correct for the efficiency of the TD and range-momentum cuts using measurements from actual data. The flux is accumulated from the analyzed runs, along with the usual corrections.

We calculate the branching ratio for  $K^+ \rightarrow \pi^+ \pi^0$  using the expression:

$$\begin{aligned}
 \text{BR}(K^+ \rightarrow \pi^+ \pi^0) &= \frac{\#K_{\pi 2}}{K_{\text{stop}}} \times \frac{1}{A_{MC}} \times \frac{A_{DC/RS}^{MC}}{A_{DC/RS}^{data}} \times \frac{A_{TG}^{MC}}{A_{TG}^{data}} \\
 &\quad \times \frac{1}{A_{DC}} \times \frac{1}{A_{BEAM}} \times \frac{1}{A_{TD}^{data}} \times \frac{1}{A_{RM}^{data}} \\
 &= \frac{4620}{(366140 \pm 4562)} \times \frac{1}{(.164 \pm .003)} \times \frac{(.947 \pm .004)}{(.836 \pm .005)} \\
 &\quad \times \frac{(.987 \pm .002)}{(.9779 \pm .0006)} \times \frac{1}{(.815 \pm .005)} \times \frac{1}{(.956 \pm .002)} \\
 &\quad \times \frac{1}{(.60 \pm .05)} \times \frac{1}{(.897 \pm .005)} \\
 &= .210 \pm .003_{(stat.)} \pm .018_{(acc.)}, \quad (\text{true value} = .2117).
 \end{aligned}$$

where  $A_{TD}^{data}$  is the acceptance of the TD cuts,  $A_{RM}^{data}$  is the acceptance of RNGMOM and RNGMOM2, and the other factors are as described in the previous section. Note that the all four reconstruction efficiencies are remeasured using  $K_{\pi 2}$  events (data and UMC, as applicable) because of systematic effects arising from photons, which are not present in the  $K_{\mu 2}$  measurements. The first error in the last line is the statistical error in the number of events and the second is the error in the acceptance. Note that the uncertainty in  $A_{TD}^{data}$  includes an estimate of systematic uncertainty, but that we have not estimated the (possibly substantial) uncertainty in  $A_{MC}$  due to the simulation of nuclear interactions. The measured value for the  $K_{\pi 2}$  branching ratio appears to be in good agreement with the accepted value; see further comments below.

\* \* \*

In summary, our measured  $K_{\mu 2}$  branching ratio is low by 6%, or more than four times the combined uncertainty in the acceptance and flux. By comparison, the  $K_{\pi 2}$  branching ratio comes out correct even though it is subject to additional systematic effects pertaining to the  $\pi^+$ , as noted earlier. Indeed, since that which affects the  $K_{\mu 2}$  branching ratio also affects the  $K_{\pi 2}$ , particularly geometry and flux, it is likely that pion systematics have caused a fortuitous cancellation in the latter measurement. Although it is difficult to verify that this is actually the case, its plausibility can be seen as follows. First, suppose that the raw scaler measurement of  $KT_{\text{live}}$ , which lacks redundancy, overestimates the true flux. This would of course

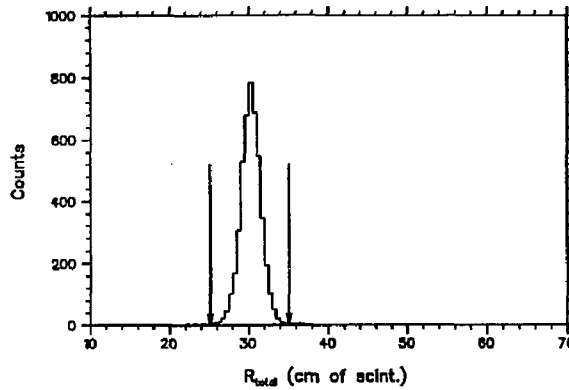


Figure 53.  $K_{\pi 2}$  Range. Events from monitor data that survive the analysis cuts. The applied range cut is indicated by the vertical arrows.

lower both branching ratio measurements. In addition, if the pion systematics are off in the other direction, this could cancel with the flux error in the  $K_{\pi 2}$  measurement while (obviously) leaving the  $K_{\mu 2}$  measurement unchanged. Given the possibly substantial uncertainty in the effects of nuclear interactions, this is not altogether unlikely. As for the scalars, aside from the systematic effects discussed in Section 5.7.1, their reliability is confirmed to better than 1% by comparison of various combinations of scaler data that should give identical results. On the positive side, we note that although the test measurements go beyond our ability to explain the particular source of discrepancy, they do nonetheless serve to limit our net systematic uncertainty to about 5%.

$K_{\pi 2}$ Analysis Summary			
Cut	Events In	Events Cut	Rejection
Level 0 Dly'd Coin.	86212	33563	1.637
TG Setup	52649	1161	1.023
DC/RS Setup	51488	12430	1.318
Offline Dly'd Coin.	39058	3348	1.094
$11 \leq L_{stop}^{rs} \leq 18$	35710	9618	1.369
$\tilde{C}_{\pi}^w$	26092	924	1.037
$B_{fit}^4$	25168	888	1.037
$B_{dE/dz}^4$	24280	202	1.008
$\theta_D$	24078	803	1.035
$D_{tgt}, D'_{tgt}$	23275	949	1.043
$E_{\pi}^{ic} < 4$	22326	946	1.044
FITPI	21380	15175	3.446
FITPI2	6205	1169	1.232
RNGMOM	5036	293	1.062
RNGMOM2	4743	90	1.019
$25 < R_{total} < 35$ cm	4653	33	1.007
Total	4620	—	—

Table 25. Summary of applied  $K_{\pi 2}$  cuts and rejection factors. A stopping layer cut restricts the events to the  $K^+ \rightarrow \pi^+ \nu \bar{\nu}$  region where the performance of the TD cuts has been measured.

## 6. Conclusion

### 6.1 LIMITS ON $K^+ \rightarrow \pi^+ \nu \bar{\nu}$ AND $K^+ \rightarrow \pi^+ f$

In summary, we find no candidate events for the processes  $K^+ \rightarrow \pi^+ \nu \bar{\nu}$  and  $K^+ \rightarrow \pi^+ f$  in a large sample of kaon decays, with a sensitivity determined by the acceptance of the selection criteria and the total kaon flux; these are measured to be:

$$\text{Flux} = (1.124 \pm .014) \times 10^{11} \text{ stopped kaons,}$$

and

$$\text{Acceptance} = \begin{cases} .0050 \pm .0005 & \text{for } K^+ \rightarrow \pi^+ \nu \bar{\nu}; \\ .0235 \pm .0023 & \text{for } K^+ \rightarrow \pi^+ f. \end{cases}$$

We now use Poisson statistics to set limits on the branching ratios for these decays. According to the Poisson distribution, there is a 10% probability that an experiment expected to count 2.3 events will instead fluctuate to zero. Hence, the definition of the 90% confidence level (c.l.) branching ratio upper limit for a counting experiment with zero measured events:

$$\text{BR} \leq \frac{2.3 \text{ Events}}{\text{Flux} \times \text{Acceptance}}.$$

But before applying this definition to our particular case we must reconcile our sensitivity for the rare modes with the small inconsistencies in the branching ratio measurements of the known processes  $K_{\pi 2}$  and  $K_{\mu 2}$  presented earlier. Therefore, we introduce a final correction—normalization to the  $K_{\mu 2}$  branching ratio—and

compute our limits as follows:

$$\begin{aligned} \text{BR} &\leq \frac{2.3 \text{ Events}}{\text{Flux} \times \text{Acceptance}} \times \frac{\text{BR}_{K_{\mu 2}}^{\text{true}}}{\text{BR}_{K_{\mu 2}}^{\text{meas.}}} \\ &= \frac{2.3 \text{ Events}}{\text{Flux} \times \text{Acceptance}} \times \frac{.6351}{.597}, \end{aligned}$$

where  $\text{BR}_{K_{\mu 2}}^{\text{true}} = .6351$  and  $\text{BR}_{K_{\mu 2}}^{\text{meas.}} = .597$  are the accepted and measured values for the  $K_{\mu 2}$  branching ratio, the latter from Section 5.7.2.

Although  $K_{\pi 2}$  decays embody more systematic effects common to the two rare processes than do  $K_{\mu 2}$  decays, in that all three have a  $\pi^+$  in the final state, it is difficult to clearly demonstrate that pion systematics alone are responsible for the apparent accuracy of the  $K_{\pi 2}$  measurement in view of the discrepancy in the  $K_{\mu 2}$  measurement, especially considering that the systematics of the latter are almost certainly common to all. In other words, if we could show decisively that our pion efficiency is systematically underestimated and that our flux is systematically overestimated, normalizing the rare mode measurements to the  $K_{\pi 2}$  would be justified (and virtually the same as no correction at all). However, since this is not the case and to be conservative, we use the  $K_{\mu 2}$  measurement to compute the correction since it has the largest percentage error in the direction that suggests we would otherwise underestimate our rare mode upper limits. Therefore, we substitute the various factors into the above inequality to get the final results:

$$\text{BR}(K^+ \rightarrow \pi^+ \nu \bar{\nu}) \leq 4.4 \times 10^{-9} \quad (90\% \text{ c.l.}),$$

and

$$\text{BR}(K^+ \rightarrow \pi^+ f) \leq 9.3 \times 10^{-10} \quad (90\% \text{ c.l.}).$$

We have neglected the fractional error of 10% in the acceptance: given that the variance ( $\sigma^2$ ) of a Poisson distribution is equal to the mean number of events, here assumed to be 2.3, we note that a fractional error of 10%, or .23, has a negligible

effect when added in quadrature to 2.3:

$$2.3 + .23^2 = 2.35,$$

which is to say that the statistical error in the number of events completely dominates the uncertainty in the acceptance. Besides, by normalizing to the  $K_{\mu 2}$  branching ratio we have in effect already accounted for the latter.

The above upper limit for the branching ratio of  $K^+ \rightarrow \pi^+ \nu \bar{\nu}$  represents a factor of 32 improvement over the previous search [11] and a factor of 8 compared to our own 1988 result [10]; similar factors for  $K^+ \rightarrow \pi^+ f$  are 41 and 7. This new limit for  $K^+ \rightarrow \pi^+ \nu \bar{\nu}$  is consistent with the Standard Model prediction of  $(.6-6) \times 10^{-10}$ ; furthermore, we have not yet reached the sensitivity to further constrain any of the input parameters such as  $m_t$  or  $V_{td}$  (see next section). Also, the absence of an enhanced rate for a three-body signal effectively rules out the possibility of observing “new” physics in this channel; should such physics exist, its signal will in the future be difficult to distinguish from that anticipated by the Standard Model. Finally, our upper limit for the process  $K^+ \rightarrow \pi^+ f$  suggests that if the familon exists then the mass scale for the breaking of family symmetry is greater than approximately  $2 \times 10^{11}$  GeV/ $c^2$  [3]. We note that according to that same reference the mass scale (admittedly borrowed from a related particle—the “axion”) is expected to be less than about  $10^{12}$  GeV/ $c^2$ .

## 6.2 FUTURE PROSPECTS

At the time of this writing, the Collaboration has already accumulated another sample of kaons that slightly more than doubles our present flux; analysis of the data is currently underway. In addition, a number of improvements are planned over the course of the next two to three years, improvements that will ultimately yield a sensitivity capable of measuring the Standard Model rate for  $K^+ \rightarrow \pi^+ \nu \bar{\nu}$ , thus providing direct knowledge of weak mixing angles, particularly those that couple to third generation quarks. The main improvements are:

- **High-intensity/high-purity beam.** Upgrades to the secondary beam line, which include larger geometric acceptance and two stages of  $K$ - $\pi$  electrostatic separation rather than one, will raise the kaon intensity but hold the overall number of beam particles roughly constant. Upgrades to the AGS itself (the “Booster”) will increase the rate of primary protons by a factor of three.

- Trigger and data acquisition. Upgrades are planned to meet the needs of the anticipated higher kaon flux. Experience gained with the data already analyzed will allow us to make online processing more effective by applying some of our offline algorithms in real time. Also, new processor modules and circuitry are under development that will impose some of the same trigger criteria now in use but with enhanced speed, thereby keeping the online rejection at its present level but reducing the per event deadtime.
- A new central drift chamber. Multiple-scattering of particles in the material (wires and gas) of the chamber itself is believed to limit the momentum resolution as well as contribute to the "tails." Improved designs are under development that utilize "straw tubes" or a "foil chamber," thereby reducing the amount of material and with it the likelihood of scattering. Straw tubes have the added advantage that in the inter-layer gas volume we could replace the argon-ethane mixture with helium, a further reduction of matter. Also, the possible addition of a dedicated  $z$ -measuring chamber between the target and the present drift chamber (or modifications thereof) could help the resolution through a better correction of the momentum's longitudinal component. All of this would have a significant effect on kinematic background rejection of both  $K_{\tau 2}$  and  $K_{\mu 2}$  decays.
- Search larger fraction of  $\pi^+$  energy spectrum. Data were taken in 1989 and 1990 to search for  $K^+ \rightarrow \pi^+ \nu \bar{\nu}$  decays in the kinematic region *below* the  $K_{\tau 2}$  peak where it may be possible to survey as much as 30% of the kinematic phase space. Although analysis of the data are as yet incomplete, they could offer a significant contribution to our limit. However, there are many potential backgrounds. For example, if the  $\pi^+$  from a  $K_{\tau 2}$  decay scatters in the target and is kinematically degraded it can appear in the signal region. A new stopping target with finer segmentation and transient digitizer readout is being considered as a countermeasure.

In summary, these modifications along with a two or three good "seasons" of data-taking would lead to a per event sensitivity of a few times  $10^{-11}$ , sufficient to observe several  $K^+ \rightarrow \pi^+ \nu \bar{\nu}$  events at the rate predicted by the Standard Model.

## References

1. S.L. Glashow, J. Iliopoulos, and L. Maiani, *Phys. Rev. D* **2**, 1285 (1970).
2. T. Inami, and C.S. Lim, *Prog. Theor. Phys.* **65**, 297 (1981).
3. F. Wilczek, *Phys. Rev. Lett.* **49**, 1549 (1982).
4. C.O. Dib, I. Duneitz, F.J. Gilman, SLAC preprint SLAC-PUB-4840 (1989).
5. U. Türke, *Phys. Lett.* **168B**, 296 (1986).
6. J. Ellis and J.S. Hagelin, *Nucl. Phys.* **B217**, 189 (1983).
7. M.K. Gaillard, Y.C. Kao, I-H. Lee, and M. Suzuki, *Phys. Lett.* **123B**, 241 (1983).
8. S. Bertolini and A. Masiero, *Phys. Lett.* **49**, 1549 (1986).
9. S. Bertolino and A. Santamaria, *Nucl. Phys.* **B315**, 558 (1989).
10. M.S. Atiya, *et al.* (The E787 Collaboration), *Phys. Rev. Lett.* **64**, 21 (1990).
11. Y. Asano, *et al.*, *Phys. Lett.* **107B**, 159 (1981).
12. T.D. Lee and C.N. Yang, *Phys. Rev.* **104**, 254 (1956).
13. R.P. Feynman, and M. Gell-Mann, *Phys. Rev.* **109**, 193 (1958).
14. N. Cabibbo, *Phys. Rev. Lett.* **10**, 531 (1963).
15. S. Weinberg, *Phys. Rev. Lett.* **19**, 1264 (1967); **27**, 1688 (1971).
16. M. Kobayashi, and T. Maskawa, *Prog. Theor. Phys.* **49**, 282 (1972).
17. D.H. Perkins, "Introduction to High Energy Physics," 2nd Ed., p. 250, Benjamin/Cummings, (1982).
18. J. Ellis, J.S. Hagelin, and S. Rudaz, *Phys. Lett.* **B192**, 201 (1987).
19. M.K. Gaillard and B.W. Lee, *Phys. Rev.* **D10**, 897 (1974).
20. L.S. Littenberg, E787 Technical Note 179; P.D. Meyers, *private communication*.

21. J.S. Frank and R.C. Strand, *Proceedings of the Workshop on Scintillating Fiber Detector development for the SSC*, Fermi National Accelerator Laboratory, 1988.
22. J.V. Cresswell *et al.*, *IEEE Transactions on Nuclear Science* **35** 460 (1988).
23. M.S. Atiya *et al.*, *Nucl. Instr. Meth.* **A279**, 180 (1989).
24. M.A. Selen, Ph.D. Dissertation (unpublished), Princeton University, (1988).
25. M.S. Atiya, *et al.* (The E787 Collaboration), *Phys. Rev. Lett.* **63**, 2177 (1989).
26. M.S. Atiya, *et al.* (The E787 Collaboration), *Phys. Rev. Lett.* **65**, 1188 (1990).
27. M.S. Atiya, *et al.* (The E787 Collaboration), *in preparation*.
28. P.D. Meyers, E787 Technical Note 185.
29. R. Ford and W. Nelson, SLAC-210 (1978).
30. A.J. Stevens, E787 Technical Note 112.
31. D.S. Akerib, D.R. Marlow, P.D. Meyers, E787 Technical Notes TN-168 and TN-186.